EFFICIENT DESIGN TOWARDS HIGHLY SELECTIVE LOW/SELF-POWERED GAS SENSOR

By

MAMABOLO MASHAOLE STUART

A DISSERTATION SUBMITTED IN PARTIAL FULFILMENT OF THE REQUIREMENTS FOR THE DEGREE OF MASTER OF SCIENCE IN PHYSICS IN THE DEPARTMENT OF PHYSICS, SCHOOL OF PHYSICAL AND MINERALS SCIENCES, FACULTY OF SCIENCE AND AGRICULTURE, UNIVERSITY OF LIMPOPO, SOUTH AFRICA.

SUPERVISOR: PROF D.E MOTAUNG

CO-SUPERVISOR: PROF T.E MOSUANG

JANUARY 2023

Declaration

I declare that the work reported under the title " Efficient design towards highly selective low/self-powered gas sensor" submitted to the University of Limpopo for the fulfilment of a Master of Science degree in Physics is my own work that all the sources that I have used or refer to have been indicated and acknowledged by means of complete references and that this work has not been submitted before for any other degree at any other institution.

24/01/2023

Mamabolo M.S

Date

Acknowledgments

I would like to thank:

- God almighty for the strength, love, and courage.
- My supervisor, Prof D.E Motaung for the exclusive guidance and support for the success of this research.
- I would like to thank all my colleagues and friends at the University of Limpopo for their sufficient input.
- I am also thankful to my co-supervisor Prof T.E Mosuang for his support and for making sure that the submission of the Dissertation is successful.
- Dr. Z.P Tshabalala, Dr. R Motsoeneng, and Mr. L.M Maebana for their help in the discussion and the analysis of the results.
- The Council for Scientific and Industrial Research *(*CSIR*)* HCD-INERBURSARY for their financial support throughout my MSc.
- University of Free State (UFS), Physics Department for equipment access.
- My family for their full support.

Publications and conference presentations

Publications:

- M.S.Mamabolo, Z.P.Tshabalala, H.C.Swart, G.E.Mphaphuli, T.K.Hillie, D.E.Motaung. Low Temperature Tunability on CO Selectivity, Low Detection Limit Based on SnO_2-Hollowspheres Induced by Various Bases. Surfaces and Interfaces. **31 (**2022) 101954. (https://doi.org/10.1016/j.surfin.2022.101954

Conference Presentations:

- Mamabolo M.S, Z.P Tshabalala and Motaung D.E. Low concentration selectivity of H_2S by SnO_2 Hierarchical Nanoplatelets Induced by Various Bases. Faculty of Science and Agriculture Research Day at Bolivia Lodge, Polokwane, 6 to 8 October 2021. Oral presentation.
- Mamabolo M.S, Z.P Tshabalala and Motaung D.E. Low concentration selectivity of H_2S by SnO_2 Hierarchical Nanoplatelets Induced by Various Bases. The 7th CSIR Emerging Researchers Symposium, 12 and 13 July 2022 at the CSIR International Convention Centre in Pretoria. Poster presentation.

Dedications

This work is dedicated to:

My mother

Shelly Malegola Mamabolo

My brother

Kalakala Phillimon

ABSTRACT

The daily population activities linked to the emission of various hazardous gases that can be toxic, explosive, and flammable such as CO, H_2S, SO_2, NO_x, CO_2, and volatile organic compounds have a negative impact on human lives and the environment. The development of NO_2 and CO gas sensors is vital for prompt detection due to their poisonous behaviour, which may lead to immediate deaths.

Consequently, tin dioxide (SnO_2) and vanadium pentoxide (V_2O_5) nanostructures were prepared following a facile hydrothermal method using different bases for the detection of various gases. The SnO_2-NaOH displayed hollow sphere-like structures with etched surfaces, while the SnO_2-NH_4OH and SnO_2-Urea illustrated nanoflakes and hierarchically arranged nanoflakes forming spheres, respectively. The V_2O_5 nanostructures showed nanorod like structures that varied in thickness and length with base. Structural findings exhibited improved crystalline structure of the SnO_2 in the following behaviour: SnO_2-NaOH<SnO_2-Urea<SnO_2-NH_4OH. In-situ electron paramagnetic resonance and photoluminescence studies disclosed that the SnO_2-NaOH possessed a significantly high concentration of oxygen vacancies (V_O). Consequently, the SnO_2-NaOH based sensor disclosed an exceptional selectivity to CO gas amid other target gases while operating at low temperature (75 °C). The sensor displayed a higher resistance ratio (≈32) at 60 ppm, a sensitivity of 0.49 ppm^{-1}, and a low theoretical detection limit of 70 ppb. Such unprecedented performance towards CO was owing to a higher number of surface defects induced by the strategy of utilizing NaOH as a base to tailor the surface properties of the SnO_2.

SnO_2/CuO-(1.0:1.0 M), SnO_2/CuO-(0.5:1.0 M) and SnO_2/CuO-(1.0:0.5 M) heterostructures-based sensors were also fabricated for detection of NO_2 gas at room temperature. The fabricated materials were characterized using various techniques, to investigate the structure, morphology, internal structure, and optical properties. The elemental mapping was also carried out to investigate the distribution of both Cu and Sn. To test their suitability in gas sensing applications, the nanomaterials were tested towards various gases at different temperatures. Among the tested sensors, the SnO_2/CuO-(1.0:1.0 M)-based sensor showed a higher response towards NO_2, in the presence of other four gases at room temperature. At 100 °C, the sensors showed a poor response, justifying that their optimal temperature is 25 °C. These results indicate that these sensors could be considered as low-power consumption sensors for the detection of NO_2.

TABLE OF CONTENTS

LIST OF FIGURES

LIST OF TABLES

CHAPTER 1

1.1. Overview

For decades, gas sensors such as semiconductor contact combustion, and electrochemical gas sensors have been investigated for the purpose of detecting and monitoring different gases in the environment and protecting human life [1.1]. Among these, semiconductor metal oxide (SMO) gas sensors have received extensive research and attention in the gas sensors field due to their advantages such as ease to use, production flexibility, low maintenance, low cost [1.2, 1.3], high sensitivity, rapid response and recovery time, reversibility, stability, simple electronic interface, and capacity to detect huge amounts of gases. [1.3, 1.4]. In overall SMO such as TiO_2, SnO_2, WO_3, ZnO, Fe_2O_3, etc. have been investigated, among all the SMO SnO_2 has been broadly investigated and used in the gas sensing field for the detection of various gases such as NO_2, NO, CH_4, H_2S, SO_2, CO_2, CO, etc. [1.5, 1.6], since it has great advantages over other materials in gas sensing, such as firm response, high sensibility, long-term stability, etc. Khalifa et al. [1.7]. SnO_2 nanoparticles are useful in the field of gas sensing because of their high surface-to-volume ratio, which results in improved sensitivity and adsorption capacity [1.8, 1.9].

SnO_2 gas sensors have been used to detect high humidity and inflammable gases, and the change in the electrical impendence of SnO_2 surface due to molecules adsorbed is used in measuring the electrical impendence of SnO_2 [1.10]. Toxic and combustible gases in low or high concentrations may be monitored using SnO_2 electric conductivity, which is employed as the most active layer in gas detecting devices

[1.11]. Tin oxide has a large theoretical capacity, is non-toxic, and is inexpensive, and so on, making it an excellent material for gas sensing [1.12].

The global gas sensor markets were valued at USD 1123.3 million in 2019 and is predicted to increase at an 8.66 percent compound yearly growth rate (CAGR) during the forecast period, reaching USD 1795.9 million by 2025 [1.13]. According to Grand View Research, the global market for gas sensors is predicted to reach USD 4.0 billion by 2027, with a CAGR of 8.3 percent from 2020 to 2027 [1.14]. The role of gas sensors in global economic growth is critical.

The elevated rate/level of air pollution in the environment is governed by the population activities related to the emission of toxic, flammable, explosive, and hazardous gases, which have a huge impact on the health and environment [1.15]. The outdoor sources that lead to air pollution globally include the burning of fossil fuel and biomass (generate power), transport, food production, industries, etc. which lead to the emission of various gases [1.16], whereas the indoor sources of air pollution include the use of gas and coal stoves, smoking, combustion of solid fuel, firewood, etc. [1.17, 1.18]. The emitted gases such as Methane (CH_4), Carbon monoxide (CO), carbon dioxide (CO_2), Sulphur dioxide (SO_2), Nitrogen dioxide (NO_2), nitrogen monoxide (NO), hydrogen sulfide (H_2S), Ammonia (NH_3), and volatile organic compounds. Some of these gases are invisible and when inhaled causes diseases such as respiratory diseases, lung diseases, cardiovascular diseases, etc. which causes mortality and morbidity [1.19-1.22].

Nitrogen dioxide (NO_2) is a major air polluter that is emitted from the ground by the burning of fossil fuels in manufacturing, processing, and petroleum operations such as automobile exhaust, power plants, businesses, and households [1.23, 1.24]. NO_x is produced when oxygen and nitrogen air combine. [1.25]. NO_2 gas is most toxic and reactive, removed speedily from the atmosphere in the form of dry and wet deposition than NO [1.26]. Nitrogen dioxide is released into the atmosphere, and the population inhales around 80-90 percent of it, which is absorbed by the lungs (NO_2 forms nitrous and nitric acids when it reacts with the fluids in the respiratory fluids). According to the Department of Environmental Affairs and Tourism, those who have chronic respiratory problems are particularly vulnerable to nitrogen dioxide gas exposure. [1.27]. NO_2 is a toxic gas to human health at a concentration larger than 200 g/m^3 and in the environment results in acid rain [1.28, 1.29]. NO_2 with a concentration between 15-25 ppm causes eyes and nasal irritation when exposed, also damages the cell membranes of the lungs when inhaled [1.30].

Hydrogen sulfide (H_2S) is regarded as colorless, flammable, toxic, and smelling like rotten eggs, when it reacts with air or oxygen in the atmosphere it forms an explosive mixture and reacts with iron it produces iron sulfide that will burn in air. Non-specific and anaerobic bacterial drop of sulphates and sulphur-containing organic molecules are natural sources. Natural bases include non-specific and anaerobic bacterial decline of sulphates and sulphur-containing organic compounds. [1.31, 31.2]. H_2S is a toxic substance polluter for both the environment and industrial affecting both humans, animals, and ecosystems. It is a colorless gas and heavy gas than air [1.33]. H_2S causes human nervous system damage when exposed to it, this gas is found in petroleum exploration, diverse industrial processes, and coal mines [1.34].

Ammonia (NH_3) is a toxic, irritant, corrosive, invisible, and odorless combustion applied in the manufacturing of fertilizer, refrigerant, and household cleaning products.

The emission of this gas causes atmospheric pollution, and it has effects on the eye and respiratory system and by being exposed to it results in death [1.34, 1.35].

The burning of coal, high-sulfur coal, and cars using diesel fuel results in the emission of invisible, non-flammable, and non-explosive sulfur dioxide (SO_2) gas as an environmental polluter [1.30]. SO_2 affects the respiratory system (asthma, cough, effects on children's lungs) when exposure at the high level of SO_2, also it reacts in the atmospheric level to form sulphuric acids with results in acid rain [1.36, 1.37]. The SO_2 gas reacts with moisture in the nose, throat, and nasal cavity to destroy the respiratory system nerves, also results in eye irritation, coughing, asthma, mucus secretions, coughing, and chronic bronchitis also lead to everyday hospital admission because of cardiac issues and death rates due to the highest concentration of SO_2 [1.30].

Carbon dioxide (CO_2) is an invisible, tasteless, non-flammable gas heavier than air that creates the greenhouse effect. It is created and released via the combustion of fossil fuels, human respiration, forest fires, and autotrophs plant, and it also causes oxygen deficit [1.38, 1.39]. CO_2 is a by-product of human metabolism [1.40]. The exposure limit for CO_2 is 8 hours, if inhaled at a high concentration it may result in health problems such as cancer, neurological diseases, sleep disorders, inflammation, and calcification of body tissue [1.41]. CO is invisible, odors, and tasteless with low water solubility and low reactivity, when incomplete combustion takes place, CO is emitted in the atmosphere and results in high death rates when exposed to its high level. Breathing CO results in health effects like headache, vomiting, weakness, dizziness, etc. [1.42]. Both nature and human activities contribute a lot to the formation of CO_2 levels in the atmosphere mainly by the burning of fossil fuel, extraction, and deforestation [1.43]. CO results in death by forming hypoxia with damaged cells in the blood [1.44]. Both CO and CO_2 come from the combustion of fossil fuels and tobacco smoke mainly formed by human activities, the level of CO and CO_2 can reduce the oxygen level in the air leading to death and related diseases such as nausea, drowsiness, headaches, and unconsciousness [1.45].

Volatile organic compounds (VOC) are considered as other forms of air pollution and boils between 100-250 ºC and measured at 101.3kPa, which is standard atmospheric pressure and has an impact on the formation of the tropospheric ozone layer [1.46]. VOC is classified as main sources such as traffic of road (24% of non-methane was reported in France 2002), industrial or domestic uses, such as paints, varnish or glue, and hydrocarbon evaporation [1.25]. VOC such as benzene, toluene, ethylbenzene, and xylenes (BTEX) is a threat to population health since it is categorized as a form of pollutants of the atmosphere, VOC travel a long distance from the emission spot through the air and can enter the body through the skin which will results in health effect like pathology, including asthma, atopic, dermatitis and neurologic [1.46].

Pollution Management and Environmental Health Program reported that in 2016 that the global economy has spent US$5.7 trillion which is 4.8% of global GDP only for ambient air pollution [1.47], while the World Health Organization (WHO) probable that roughly seven million people lost their life worldwide annually due to air pollution, both humans and natural activities. WHO also indicated that about 94% of death is occurring in low-middle income countries [1.48, 1.49]. In South Africa, the death rate owing to home air pollution (indoor activities) was 34 per 100 000 in 2016, due to acute and respiratory, as well as cardiovascular illnesses [1.50]. In Africa, it was claimed in 2013 that the cost of air pollution is enormous, around USD450 billion, with people losing their lives and the need for healthcare facilities increasing as a result of the impact of air pollution [1.51]. The WHO calculated specific limits of air pollution where people are permitted to dwell, but 90% of the world's population lives in areas that exceed the limit; in the United States, air pollution costs more than $200 billion each year [1.52].

Recent research has shown that in low- and middle-income countries indoor air pollution is experienced from the use of solid fuels, gas stoves, tobacco smoking, heaters particularly in southern Africa [1.53], which releases various toxic and colorless gases [1.54] such as sulfur dioxide (SO_2), particulate matter (PM), oxides of nitrogen, volatile organic compounds, and carbon monoxide (CO) [1.55]. Because the majority (roughly 90%) of South Africans use kitchens, furniture, wall insulation, personal care products, cleaning products, and so on. The covid-19 regulation, which was announced nationally by the president of the RSA, required people to spend the entire day indoors, increasing the health effects caused by indoor air pollution [1.56, 1.57]. 20% of South African households experience the health effect or diseases such as cancer, low birth weight, cardiovascular disease, asthma, tuberculosis, cataracts, acute lower respiratory infections (ALRI) in children etc and 1,400 children die annually in South Africa due to indoor air pollution [1.58].

1.2. Problem statement

The rapid population growth and the daily humans' activities are linked to the emission of toxic and hazardous gases that threatens the environment and health of the population [1.59]. The necessity to create and, the evolutions of the intensified gas sensor devices for the monitoring and detection of nitrogen dioxide (NO2) and carbon monoxide (CO) gases in the environment is of great demand for protecting human lives from harmful gases [1.60]. In South Africa, the populations are endangered from the sources that release NO_2 and CO during operation, such as car exhaust, household and mining industries [1.61, 1.62]. Gas sensors are useful in coal industries to monitor the leakage of NO_2 and CO from the containers and machines during manufacturing, which may lead to harm or explosion. Whereas in some houses where they used gas, wood, oil, kerosene, cigarettes and coal burning appliance, such as stoves, heaters, furnaces, boilers and fireplaces and gas engines, in cars and home generators, which contribute to the elevation of NO_2 levels makes gas sensor devices more preferable [1.63-1.65]. According to the World Health Organization reports in 2012, roughly three million population die yearly around the world because of the ambient air pollution. The low- and middle income countries suffer the most horrible effects. For instance, emerging countries, which have a substantial dependence on fossil fuels, such as South Africa (SA), India, etc. deal with the greater part of the health effects, production losses and mortality linked significant to air pollution. A topical study has denoted that 7.4% of all deaths in SA is related to chronic exposure to toxic gases, which cost the SA economy roughly 6% of its Gross Domestic Product (GDP) [1.66]. For instance, the accelerated rates of Tuberculosis and HIV/AIDS infection justifies that the country should consider linking the mortality rate with the air pollution. Furthermore, recent study has shown that long-term exposure to air pollution could contribute to higher numbers of COVID-19 fatalities, thus confirming a clear correlation between COVID-19 deaths with the air pollution, especially to extremely polluted countries, such as India, Italy, etc. [1.67]. Thus, the current work focuses on the production of low-powered portable gas sensors for detection of NO_2 and CO, which will provide the air quality regulator with sufficient and reliable data related to air quality.

1.3. Aim.

- The aim of the study is to develop a low-powered gas sensor device that could enhance the environmental sustainability.

1.4. Objectives.

The objectives of the study are to:

I. Synthesise inorganic p-type CuO and n-type SnO_2 and V_2O_5 nanostructures
II. incorporate inorganic on the organic polymer matrix as an acceptor material and donor materials that can harvest solar light to produce an open-circuit voltage (V_{OC}), which is associated to the potential at heterojunction.
III. Attempt to synthesis both low or self-powering and selective detection methods in a singular integrated sensor device.
IV. Synthesise noble metals as to improve the sensitivity and light scattering in the sensor and solar cell device.
V. Investigate the long-term stability of solar cell and sensing layer when exposed to different environments.

1.4. DISSERTATION OUTLINE

- **Chapter One:** deals with an overview and the problem statement associated with the detection of NO_2 and CO. The chapter further illustrates the thesis outline.

- **Chapter Two:** focuses on the literature review around the semiconductor metals oxides gas sensing. It also discusses the properties of the CuO, V_2O_5 and SnO_2.

- **Chapter Three:** Deals with the characterization techniques, as well as the synthesis methods used in the current work.

- **Chapter Four:** Focuses on the results obtained from the preparation of individual materials, such as V_2O_5 and SnO_2 and their detection towards CO.

- **Chapter Five:** Focuses on the preparation of p-n SnO_2/CuO heterostructures by varying the molarity of both SnO_2 and CuO. The realization of room temperature NO_2 gas sensing derived from n-p SnO_2/CuO heterostructure is also discussed.

- **Chapter Six:** Deals with the summary and future work.

1.5. References

1.1 Wei Guan. Na Tang. Kuang He. Xiaoying Hu. Mingshan Li. Kaiming Li. Gas-Sensing Performances of Metal Oxide Nanostructures for Detecting Dissolved Gases: A Mini Review. Frontiers in chemistry 8 (2020) 1-5.

1.2 Chengxiang Wang. Longwei Yin. Luyuan Zhang. Dong Xiang. Rui Gao. Metal Oxide Gas Sensors: Sensitivity and Influencing Factors. Sensors. (2010). 10. p2088-2106.

1.3 Young Kook Moon. Seong-Yong Joeng. Yun Chank Ang. Jong-Heun Lee. Metal Oxide Gas Sensor with Au Nanocluster Catalytic Overlayer: Toward Tuning Gas Selectivity and Response Using a Novel Bilayer Sensor Design. ACS applied materials and interface. 11 (2019).. p32169-32177.

1.4 Brian Yuliarto. Gilang Gumilar. Ni Luh Wulan Septiani. SnO_2 Nanostructure as Pollutant Gas Sensors: Synthesis, Sensing Performances, and Mechanism. Advances in Materials Science and Engineering. (2015). 2015. p1- 15.

1.5 David E Motaung. Gugu. H. Mhlongo. Peter R. makgwane. Baban P. Dhonge. Franscious R. Cummings. Hendric C. Swart. Suprakas Sinha Ray. Ultra-high sensitive and selective H_2 gas sensors manifested by interface of n-n Heterostructure of CeO_2-SnO_2 nanoparticles. Sensors and Actuators B: Chemical. 254 (2017) 984-995.

1.6 Ioannis Kortidis. Hendrik C. Swart. Suprakas Sinha Ray. David E Motaung. Characteristics of point defects on the room temperature ferromagnetic and high NO_2 selectivity gas sensing of p-type Mn_3O_4 nanorods. Sensors and Actuators B: Chemical. (2019). 285. p92-107.

1.7 Khalifa Aguir, Sandrine Bernardini, Bruno Lawson, Tomas Fiorido. Trends in metal oxide thin films: Synthesis and applications of tin oxide. Tin oxide materials. (2020). 8. p219-246.

1.8 Simin Tazikeh. Amir Akbari. Amin Talebi. Emad Talebi. Synthesis and characterization of tin oxide nanoparticles via the Co-precipitation method. 2014. 99.

1.9 Svitlana V. Nagirnyak. Victoriya A. Lutz. Tatiana A. Dontsova. Igor M. Astrelin. Synthesis and Characterization of Tin(IV) Oxide Obtained by Chemical Vapor Deposition Method. Nanoscale research letters. (2016). 11. p1-7.

1.10 Zhiwen Chen. Dengyu Pan. Zhen Li. Zheng Jiao. Minghong Wu. Chan-Hung Shek. C. M. Lawrence Wu. Joseph K. L. Lai. Recent Advances in Tin Dioxide Materials: Some Developments in Thin Films, Nanowires, and Nanorods. Chemical reviews. (2014). 114. p7442 -7486.

1.11 Sophie de Monredon. Antoine Cellot. Franc¸ois Ribot. Cle´ment Sanchez. Lidia Armelao. Lethicia Gueneau. Laurent Delattre. Synthesis and characterization of crystalline tin oxide nanoparticles.journal of Materials Chemistry. (2002). 12. p2396-2400.

1.12 M. Alaf. D. Gultekin. H. Akbulut. Tin/Tin oxide (Sn/SnO2) Nanocomposites Thin Films as Negative-Electrode Materials for Li-Ion Batteries. Acta Physica Polonica. (2013). 123. p323-325.

1.13 https://www.marketresearchfuture.com/reports/gas-sensors-market-5459.

1.14 https://www.grandviewresearch.com/press-release/global-gas-sensors-market.

1.15 Ioannis Manisalidis. Elisavet Stavropoulou. Agathangelos Stavropoulos. Eugenia Bezirtzoglou. Environmental and Health Impacts of Air Pollution: A Review. Frontiers in public health. (2020). 14. p1-13.

1.16 Danielle Millar. Caradee Y. Wright. Statement on Air Pollution and Health. South African Journal of Sciences. (2019). 115. p1996-7489.

1.17 Busisiwe Shezi. Caradee Y Wright. Household air pollution exposure and respiratory health outcomes: a narrative review update of the South African epidemiological evidence. Clean Air Journal. (2018). 28. p43-56.

1.18 Marie A. Coggins. Sean Semple. Fintan Hurley. Amy Shafrir. Karen S. Galea. Hilary Cowie. Araceli Sanchez-Jimenez. Carole Garden. Paul Whelan. Jon G. Ayres. Indoor Air Pollution and Health (IAPAH). Environmental Protection Agency Johnstown Castle, Co Wexford, Ireland, STRIVE Report. (2013). 2007 1-3.

1.19 Xin Yan. Yanan Wu. Rui Li. Chengqian Shi. Ramiro Moro. Yanqing Ma. Lei Ma. High-Performance UV-Assisted NO_2 Sensor Based on Chemical Vapor Deposition Graphene at Room Temperature. ACS omega. (2019). 4. p14179-141187.

1.20 M. Matooane.J. John R. Oosthuizen. M. Binedell. VULNERABILITY OF SOUTH AFRICAN COMMUNITIES TO AIR POLLUTION. 18th World Congress on Environmental Health Durban, South Africa. (2004). p1-8.

1.21 Janine Wichmann. Air pollution epidemiologic studies in South Africa - Need for freshening up. Reviews on environmental health. (2005). 20. p265-302.

1.22 Kayode S. John. Kamson Feyisayo. Air Pollution by Carbon Monoxide (CO) Poisonous Gas in Lagos Area Southwestern Nigeria. Atmospheric and Climate Sciences. (2013). 3. p511.

1.23 Jun Wang. Wei Zhang. Rui Cao. Xiangyu You. Hong Lai. Analysis of Nitrogen Dioxide in Environment. Advances in Bioscience and Biotechnology. (2016). 7. p278-288.

1.24 Francisco-Javier Mesas-Carrascosa. Fernando Pérez Porras. Paula Triviño-Tarradas. Alfonso García-Ferrer. Jose Emilio Meroño-Larriva. Effect of Lockdown Measures on Atmospheric Nitrogen Dioxide during SARS-CoV-2 in Spain. Remote Sensing. 2020. 12. p1-15.

1.25 C. Pénard-Morand. I. Annesi-Maesano. Air pollution from source of emission to health effect. (2004). 1. p108-119.

1.26 O V Bednova. V A Kuznetsov. Effect of atmospheric air pollution on local nitrogen cycles in the urban forest ecosystem. Breath. IOP Conference Series: Earth and Environmental Science. (2019). 316. p1-8.

1.27 https://www.ncbi.nlm.nih.gov/books/NBK230446/

1.28 Chao Zhanga. Yifan Luoa. Jiaqiang Xu. Marc Debliquy. Room temperature conductive type metal oxide semiconductor gas sensors for NO_2 detection. Sensors and Actuators A: Physical. (2019). 289. p118-133.

1.29 Atham Raghunandan. Mamopeli Matooan. Rietha Oosthuizen. DEPARTMENT OF ENVIRONMENTAL AFFAIRS AND TOURISM. PUBLICATION SERIES B: BOOK 5, nd.

1.30 Rahila Rahman Khan. M.J.A. Siddiqui. Review on effects of Particulates; Sulfur Dioxide and Nitrogen Dioxide on Human Health. International Journal of Research in Environmental Science. (2014). 3. p70 - 73

1.31 Parimal Chandra Bhomick. Kaza Somasekhara Rao. Sources And Effects of Hydrogen Sulfide. Journal of Applicable Chemistry. (2014). 3. p914-918.

1.32 Dr C.-H. Selene J. Chou. Hydrogen Sulfide: Human Health Aspects. World Health Organization. (2003). 662. p1-41.

1.33 RJ Reiffenstien. William C. Sheldon H Roth. Toxicological and Environmental Impacts of Hydrogen Sulfide. Annual Review of Pharmocology and Toxicology. (1992). 32. p109-134.

1.34 João B. A. Gomes. Joel J. P. C. Rodrigues. Ricardo A. L. Rabêlo. Neeraj Kumar. Sergey Kozlov. IoT-Enabled Gas Sensors: Technologies, Applications, and Opportunities. Sensors and Actuator Networks (2019).8. p1-29.

1.35 Fatma Sarf. Metal Oxide Gas Sensors by Nanostructures. Gas Sensors. (2019).1. p1-17.

1.36 Sahar Geravandi. Gholamreza Goudarzi. Ali Akbar Babaei. Afshin Takdastan. Mohammad Javad Mohammadi. Mehdi Vosoughi Niri. Shokrollah Salmanzadeh. Esmat Shirbeigi. Health Endpoint Attributed to Sulfur Dioxide Air Pollutants. Jundishapur Journal of Health Sciences. (2015). 7. 15. p1-5.

1.37 C. Pénard-Morand. I. Annesi-Maesano. Air pollution from source of emission to health effect. Breathe. (2004).1. p108 - 119.

1.38 Brian Yuliarto. Gilang Gumilar. Ni Luh Wulan Septiani. SnO_2 Nanostructure as Pollutant Gas Sensors: Synthesis, Sensing Performances, and Mechanism. Advances in Materials Science and Engineering. (2015). 2015. p1-15.

1.39 Kenichi Azuma. Naoki Kagi. U. Yanagic. Haruki Osawa. Effects of low-level inhalation exposure to carbon dioxide in indoor environments: A short review on human health and psychomotor performance. Environment International. (2018). 121. 51- 56.

1.40 László Kajtár. Levente Herczeg. Influence of carbon-dioxide concentration on human well-being and intensity of mental work. QJ Hung. Meteorol.Serv. (2012). 116. p145-169.

1.41 P.N. Bierwirth. Carbon dioxide toxicity and climate change: a major unapprehended risk for human health. Web published: ResearchGate. (2019). 10. p1-23.

1.42 Richard J. Levy. MD. FAAP. Carbon Monoxide Pollution and Neurodevelopment: A Public Health Concern. 2015.

1.43 Reda El Arafy. Air Pollution Control Technology for CO_2 Reductions. Neurotoxicologyand teratology. (2014). 49. p31-40.

1.44 Fatma Sarf. Metal Oxide Gas Sensors by Nanostructures. Gas Sensors. (2019).1. p1-17.

1.45 Frank Schulze. ID Xinghua Gao. Darius Virzonis. Samar Damiati. Marlon R. Schneider. Rimantas Kodzius. Air Quality Effects on Human Health and Approaches for Its Assessment through Microfluidic Chips. Genes. (2017). 244. p1-26.

1.46 Regina Montero-Montoya. Rocío López-Vargas. Omar Arellano-Aguilar. Volatile Organic Compounds in Air: Sources, Distribution, Exposure and Associated Illnesses in Children. Annals of global health. (2018). 84. p1-14.

1.47 https://www.worldbank.org/en/programs/pollution-management-and-environmental-health-program.

1.48 https://www.who.int/health-topics/air-pollution#tab=tab_1

1.49 https://www.who.int/news-room/air-pollution.

1.50 Danielle Millar. Caradee Y. Wright. Statement on Air Pollution and Health. South African Journal of Science .(2019). 115. p1.

1.51 Busisiwe Shezi. Caradee Y Wright. Household air pollution exposure and respiratory health outcomes: a narrative review update of the South African epidemiological evidence. Clean Air Journal. (2018). 28. p43-56.

1.52 Guillaume Chansin. David Pugh. Environmental Gas Sensors 2017 .https://www.idtechex.com/en/research-report/environmental-gas-sensors-2017-2027/500.

1.53 Nkosana Jafta. Lars Barregard. Prakash M. Jeenac. Rajen N. Naidoo. Indoor air quality of low- and middle-income urban households in Durban, South Africa. Environmental research. (2017). 156. p47-56.

1.54 Nkosana Jafta. Prakash M. Jeena. Lars Barregard. Rajen N. Naidoo. Association of childhood pulmonary tuberculosis with exposure to indoor air pollution: a case control study. BMC public health. (2019). 19. p1-11.

1.55 Brendon Barnes. Angela Mathee. Elizabeth Thomas. Nigel Bruce. Household energy, indoor air pollution and child respiratory health in South Africa. Journal of Energy in Southern Africa. (2009). 20. p1-10.

1.56 Jamaji C. Nwanaji-Enwerem. Joseph G. Allen. Paloma I. Beamer. Another invisible enemy indoors: COVID-19, human health, the home, and United States indoor air policy. 2020. https://www.ncbi.nlm.nih.gov/pmc/articles/PMC7341994/

1.57 Jay Saha. Pradip Chouhan. Indoor air pollution (IAP) and pre-existing morbidities among under-5 children in India: are risk factors of coronavirus disease (COVID-19)? Journal of Exposure Scienceand Environment Epidemiology (2020). 30. p773-775. https://www.ncbi.nlm.nih.gov/pmc/articles/PMC7362832/.

1.58 Ivo Vegter. Air quality: missing the wood for the trees. Indoor pollution is SA's most serious air quality problem. Clean Air Journal. (2016). 27. p1-5.

1.59 R.G. I. Kortidis. S. Sinha Ray. D.E. Motaung. Designing $SnO2$ Nanostructure-Based sensors with tailored selectivity towards Propanol and Ethanol Vapors. ACS omega. (2019). 4. p13696-13709.

1.60 C. Melios, V. Panchal, K. Edmonds, A. Lartsev. R. Yakimova. O. Kazakova. Detection of ultra-low concentration $NO2$ in complex environment using epitaxial graphene sensors. ACS sensors. (2018). 3. p1666-1674.

1.61 E.M. Pate. Practical Considerations in the Implementation of Emissions Reduction Solutions at Eskom's Coal Fired Power Plan. 4th EU-SA Clean coal Technologies Working Group Meeting. (2012). p1-33.

1.62 R. Gorham. Air Pollution from Ground Transportation. Tournesol Conseils. (2002). p1-194.

1.63 C.H. Drake. Understanding the low temperature electrical properties of nanocrystalline SnO_2 for gas sensor applications. University of Central Florida. (2007). p1-124.

1.64 D.J. Jarvis, G. Adamkiewicz, M.-E. Heroux, Regula Rapp, and Frank J. Kelly. WHO Guidelines for Indoor Air Quality: Selected Pollutants. Nitrogen oxide. World Health Organization, Geneva. (2010). 5.

1.65 B. Ostro. Outdoor pollution. World Health Organization. (2004). p1-62.

1.66 Adverse Health Effects of Elevated Nitrogen Dioxide (NO_2) Levels in Homes – Case study. www.E-Inst.com.

Chapter 2.

This chapter discusses semiconductor metal oxide, including their properties and applications with particular focus on gas sensing. It continues with a full review of tin dioxide from bulk properties up to the structure, before concluding with bulk properties of vanadium pentoxide and copper oxide.

2. 1. Semiconductor Metal Oxide

Semiconductor metal oxides (SMOs) with sensing properties were discovered in Japan in 1962 by Seiyama; since then, SMOs have gotten a lot of interest in research [2.1]. The first demonstration of some semiconductor was conducted in the Bell laboratories in the 1950s by two scientists Brattain and Bardeen where the modified Ge as a SMOs is dependent on the atmosphere in contact with them. Heiland later briefed that metal oxides which include ZnO alters their properties of semiconductor with respect to change in the atmosphere partial pressure of oxygen or other surrounding gases, SMO reaction with various gases and conductometric changes were introduced [2.2, 2.3]. In 1960, Seyama conducted experiments with a chemoresistive device based on ZnO thin film working at 485 °C, demonstrating the possibility of gas sensing with basic electrical circuits [2.2].Taguchi introduced a SMOs gas sensor to the market, which consists of an alumina ceramic tube mounted with metal oxide, an electrode, and a heating coil that passes through it. He created the business Figaro Engineering Inc in 1969, which is still the biggest semiconductor producer in the world today, whereas Demarne was the first to patent and demonstrate the thin film metal oxide gas sensor based on micromachined silicon substrate in 1998 [2.8].

SMOs gas sensors are the ultimate researched of all gas sensors, and SMOs with sizes ranging from 1 - 100nm are commonly employed in gas sensors owing to their size dependant characteristics and high surface area per unit mass [2.9]. Semiconductor metal oxide has been widely active in the field of gas sensors due to its physical and chemical qualities such as low cost, high sensitivity, simplicity [2.4, 2.5], flexibility in manufacture, and ability to detect a wide range of gases. Due to qualities such as excellent selectivity and consistency with contemporary equipment, SMO-based gas sensors serve an essential role in human health and environmental safety, as well as the monitoring of numerous poisonous and hazardous gases [2.7].

Since the 1980s, research on SMO-based gas sensors has increased dramatically and drawn significant interest in the sensor field. SMOs such as Nb_2O_5, ZnO, NiO, CuO, and SnO_2 have established significant attention in the field of gas sensors. They have been utilized for gas sensors and are thought to be an effective material for detecting both reducing gases (such as hydrocarbons, alcohols, hydrogen, and carbon monoxide) and oxidising gases (oxygen and NO_x) [2.2, 2.6].

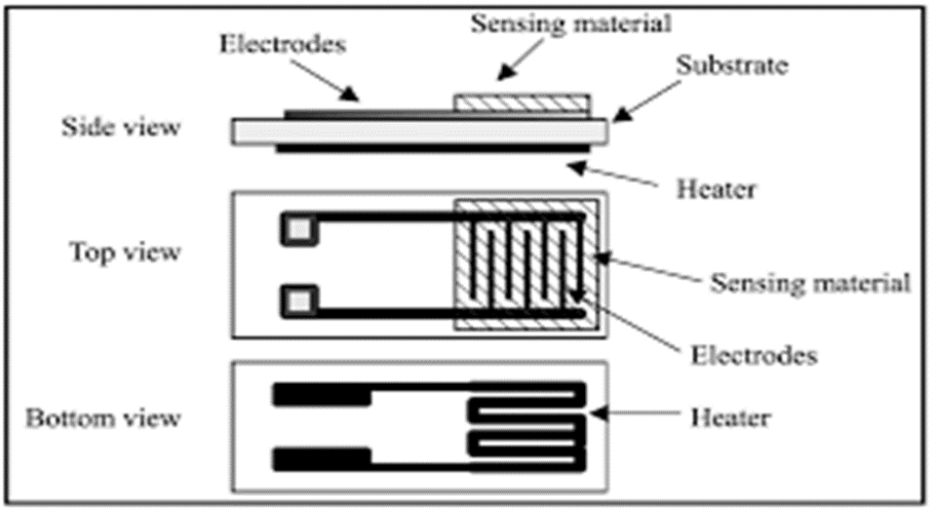

Fig. 2.1. Basic chemiresistive SMO gas sensor diagram showing side, top and bottom view.

Chemiresistive SMO gas sensor is made up of electrodes shown in fig.2.1. the resistance of the sensors and a heater on the bottom that raises the temperature sufficiently high to allow for its speed and reproducibility [2.39].

The most considered n-type semiconductors, such as SnO_2, WO_3, ZnO, In_2O_3, TiO_2, Fe_2O_3, and V_2O_5, and the p-type semiconductors, which includes CuO, NiO, Cr_2O_3, and Co_3O_4, are depicted in Fig. 2.2. In the n-type semiconductors, efforts have been focused on SnO_2, whereas in the p-type semiconductors on CuO [2.28- 2.31].

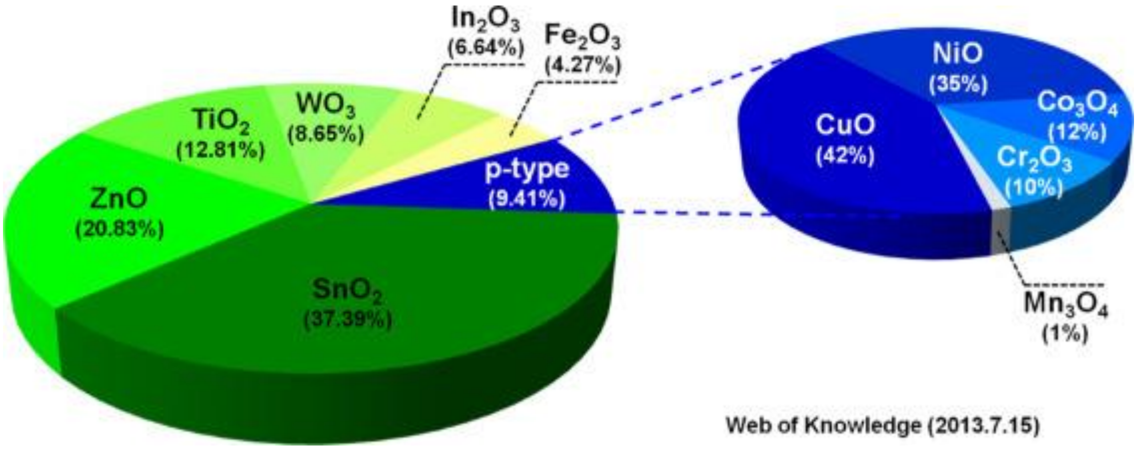

Fig. 2.2. The well most investigated n- and p-type semiconductor metal oxide gas sensors (internet search of Web of Knowledge on July 15, 2013) [2.1].

2.2. Working principle of SMO gas sensors

Semiconductor metal oxide sensors mechanism has two fundamental processes that comprise receptor and transducer as its major roles; the receptor function translates chemical data into an energy form, whilst the transducer function converts energy into signals [2.9, 2.10]. Regardless of how simple SMO measurements are in gas sensors, the detecting method remains difficult to grasp, with complications arising from several aspects that impact the functionalities of solid state gas sensors [2.3]. Wolkenstein was the first to disclose the mechanism of chemoresistive sensors based on metal oxides, where he documented the catalysis and application of electron theory of chemisorption on semiconductor [2.2]. Later, two scientists, Yamazoe and Gopel, investigated the circumstances of electric charge transmission through the SMO layer in the presence of oxygen and other reactive gases [2.3].

Based on the conductive type, semiconductor metal oxide is categorized into two types: n-type and p-type. When exposed to either reducing or oxidising gases, the indication of a drop or rise in electrical resistance is observed. The n-type resistance of the sensing layer declines when exposed to electron-donating gases (CO, H, hydrocarbons, alcohols, etc.), whereas the p-type resistances increase in the presence of electron-withdrawing gases (oxygen, NOx, etc.) [2.2, 2.6]. Formalized paraphrase. The surface redox reaction in n-type SMO gas sensors increased conductance, but the surface redox reaction in p-type SMO gas sensors decreased conductance [2.11].

Fig. 2.3 depicts the sensors connected by a neck, the grains forming large aggregates joined by grain borders, and the oxygen molecules on the surface of the grains. Adsorbed oxygen molecules absorb electrons from the conduction band on the surface of the grains and trap them as ions, resulting in a bending band and a decreased area of the electrons (space-charge layer). The sensitivity of the sensors will improve when the particle size of the sensing film is equal to or less than twice the thickness of the space-charge layer, as illustrated by Xu et al. and summarized by a semi quantitative model [2.9, 2.12]. Xu hypothesized that the neck size (X) is 0.8 times the size of the crystallite (D) and postulated that grain-boundary interactions have higher resistance when D is more than 2L. When D is smaller than 2L, the resistance grain controls the whole chain resistance and the gas sensitivity in the region [2.13].

As D becomes narrower and more comparable to 2L necks, they become more resistant and so continue to influence the sensitivity of the gas. It has been shown that on the surface of the grains, O^- or O^{2-} can be ionized by raising the resistance of the sensors coating by extracting electrons from the grains surface (Saxena Kanchan, 2010). This is due to absorbed oxygen species, which modify the energy band at the grain boundary. Because adsorbed oxygen species are very metastable, they oxidize the reducing gas when exposed to it, releasing the stored electron and lowering resistance [2.9].When D>>2L for large grains, the surface interfaces with the gas phase have no effect on crystallite volume (as illustrated in Fig. 2.3. a.), the major effect of the ambient gas on sensor conductivity is seen via the grain boundary barrier for inter-crystallite charge transport from one grain to another. Fig. 2.3.c depicts the entirely depleted region as a result of the significant drop in conductivity caused by the dead conduction routes between the grains. As D<2L and the crystallites of mobile charge carriers are nearly completely depleted, the depletion region expands throughout the entire grain, resulting in a rapid fall in conductivity as the conduction channels between the grains vanish. Because there are no substantial impediments to the transmission of inter-crystallite charge, the energy bands are essentially smooth over the whole configuration of the entangled grains, and the conductivity is basically regulated by the inter-crystallite action. In this situation, it was empirically discovered that the highest gas sensitivity is reached when D<2L. However, the gas sensing mechanism of such ultrafine particles is not evident, and additional explanation is needed to explain why there is such a sharp rise in sensitivity with decreasing grain size even when D is already less than 2L [2.16-2.18].

The working temperature governs the kinds of chemisorbed oxygen species determination, as shown in the equations below. The production of oxygen species in the surface layer of the conduction band is caused by the release of electrons, which causes the conductivity of semiconductor metal oxide to decrease when exposed to air [2.19-2.22]. Equation (2) shows that when the temperature is less than 100 ^oC, the oxygen ions adsorbed at the MOXs release electrons and become O_2^-, and when the temperature is between 100 ^oC and 300 ^oC, O^- releases electrons from the MOX surface to become O, but when the temperature exceeds 300 °C, O^{2-} occurs on the MOX surface. The electron core–core shell structure is caused by the oxygen ions adsorbing on the surface of MOX.

$$O_{2\ (gas)} \rightleftarrows O_{2\ (ads)} \qquad (1)$$

$$O_{2\ (ads)} + e^- \rightleftarrows O_2^-{}_{(ads)}\ (T<100\ ^oC) \qquad (2)$$

$$O_2^-{}_{(ads)} + e^- \rightleftarrows 2O^-{}_{(ads)}\ (100\ ^oC\text{-}300\ ^oC) \qquad (3)$$

$$O^-{}_{(ads)} + e^- \rightleftarrows O^{2-}{}_{(ads)}\ (T>300\ ^\circ C) \qquad (4)$$

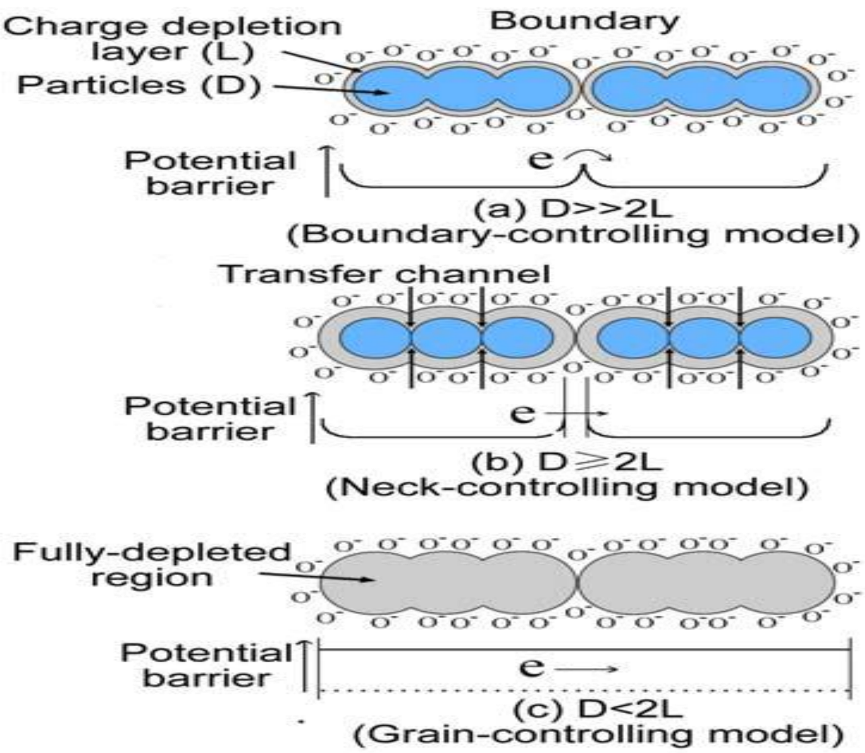

Fig. 2.3. Illustration of grain size dependence of conductance in semiconductor gas sensing materials mechanisms (a) D≫2L, grain boundary control (b) D=2L, neck control (c) D < 2L, grain control [12]. The shaded part shows the space charge region (high resistivity), while the un-shaded part shows the core region (low resistivity) [2.15].

2.3. SMOs gas sensors characteristics.

The following values govern a device's sensing operation: response, sensitivity, reversibility, response time, recovery time, life cycle, stability, operating temperature, and dynamic range.

2.3.1. <u>Response</u>: is a ratio between the resistance in air (R_{air}) and the resistance after subjection to the gas (R_{gas}) [1]. The response is expressed by:

$S = \frac{Rair}{Rgas}$ (N-type semiconductor) (5)

$S = \frac{Rgas}{Rair}$ (P-type semiconductor) (6)

2.3.2. Sensitivity: is defined as the change in the sensor's output signal obtained for an incremental change in the analyte's concentration or mass, i.e., the slope of the response-vs-concentration curve. It is also defined as the sensor's ability to distinguish between the analyte of interest and potential interferences [2.23, 2.24].The smallest concentration of the target gas volume that can be detected at the detection time is referred to as sensitivity. Sensitivity is defined as R_a / R_g for gas reduction and R_g / R_a for gas oxidation, where R_a is the resistance of the gas sensor in the reference gas (typically air) and R_g is the resistance of the gas sensor in the target gas [2.11].

2.3.3. Reversibility: the capacity of a sensor to recover from analyte exposure or return to its initial background / baseline condition [2.23, 2.24].

2.3.4. Response time: The reaction time of a sensor is the time it takes to respond from no load to a phase shift in load. Typically defined as the time required to climb to 90% of the final value in the measured variable from the commencement of phase input shift [2.23, 2.25].

2.3.5. Recovery time: of a shape-memory polymer is highly dependent upon the difference between the ambient testing temperature and the activation temperature of the polymer [2.26].

2.3.6. Life cycle: is the duration during which the sensor runs continuously [2.24, 2.27].

2.3.7. Stability: is a sensor’s ability over a given amount of time to produce reproducible data [2.6]. It is a key criterion in the production of gas sensors for the real market, as the sensors should generate a reliable and reproducible signal that corresponds to 17,000 h-26,000 h of service for at least 2-3 years [2.9].

2.3.8. Working temperature: is the temperature equivalent to optimum sensitivity [2.24].

2.3.9. Dynamic range: is the analyte concentration level between the detection limit and the maximum limiting concentration [2.24, 2.27].

2.3.10. Calibration curve: defines the relation between the concentration of target gas and the signal response [2.24].

2.3.11. Accuracy: refers to the degree of measurement precision as compared to the true value [2.51]. Accuracy represents the degree of exactness of a measurement compared to the true value.

2.4. Challenges faced by semiconductor metal oxides.

2.4.1. Humidity.

Environmental humidity is a significant problem in the development of gas sensors and has a role in impacting the sensitivity of SMO gas sensors, determining the adsorption rate by modifying the sensitivity of SMO gas sensors. Water molecules react with oxygen on the surface, causing a drop in baseline resistance, while humidity increases, causing a decrease in sensitivity. Water molecules are adsorbed on SMO surfaces, and OH- and H+ ions generated as the outcome of the dissociative adsorption process detailed in the equation below [2.5, 2.20].

$$H_2O \leftrightarrow OH^- + H \qquad (7)$$

2.4.2. Temperature.

Arsan et al. and Yamazoe and Shimanoe [2.32] provided a concise explanation of oxygen gas adsorption and target gas detection on the surface of SMOs. Temperature has a substantial influence on the adsorption of oxygen ions and the interaction of oxygen with analyte gases on the surface of SMO gas sensor material [2.33]. The sensitivity of SMOs is affected by the operating temperature; as the adsorption of oxygen species on the material surface increases, so does the temperature, but gas sensor sensitivity decreases. By applying high temperatures to the gas sensor, the sensors response will be affected by desorption of analyte gas, as reported by Sinha et al. [2.34] and Kamarudin et al.

Metal oxide gas sensors operate at temperatures ranging from 250 to 500 ºC, when chemisorbed oxygen ions species such as O^{2-}, O^{-}, and O_2^{-} develop on the surface. Chemical reactions restrict the response at low temperatures, whereas diffusion rates of gas molecules limit the response at high temperatures, but at the medium temperature, the rates of adsorption and desorption become identical and produce the maximum response [2.35]. Because SMOs gas sensor devices require a heater, it is advantageous to build low/self-powered sensors. SMO gas sensors can detect gas concentrations over 400ºC at the material's surface because thermal energy is required to activate the oxygen ions desorbed to react adsorbed surface gas molecules and perturb the detecting reaction barriers [2.36, 2.37].

2.4.3. Selectivity.

The semiconductor metal oxide gas sensing mechanism is based on the adsorption and desorption of oxygen species on its surface, and the response (under critical conditions such as high humidity) of SMOs gas sensors on diverse gases (oxidising and reducing gases) lowers the selectivity [2.38]. Gas sensor selectivity should still be more than one. In contrast to the reaction to intervening gases, greater selectivity results in a stronger gas sensors response to a target gas. Classically, gas sensors are sensitive to several gases and exhibit cross-sensitivity. It is also difficult to attain great gas sensor selectivity, which restricts the theoretical uses of gas sensors. Four common strategies for enhancing selectivity are (i) functionalization using noble-metal catalysts, (ii) altering the sensing temperature, (iii) employing heterojunctions and additives, and (iv) using filters. The usage of metal-organic frameworks (MOFs) as membranes has gained popularity in recent years since this new class of materials enhances selectivity [2.35]. Investigations were conducted to increase the selectivity of SMOs gas sensors toward specific gases because, as the sensors operate, the composition of the sensors would ultimately alter [2.40]. Suffers from limited selectivity, which may be remedied by simply doping the material with alternative substances.

2.5. Surface modification by noble metals.

Surface modification of SMOs is used to increase gas sensor responsiveness by utilizing noble metals such as Pt, Pd, Rh, Au, and Ag as activators of surface processes; the reactivity of a material may be altered by increasing the modifier concentration [2.41, 2.42]. Noble metals such as Pd and Pt have been employed as catalytically active dispersions on the surface of metal oxides to increase the performance and sensitivity of gas sensors [2.43]. In the case of tin oxide noble metals, Ag and Pd impact the work function while Pt works as a catalyst; the work function of Pd and Ag increases but can decrease to zero in the current reducing environment [2.44]. The additions of noble metals increase the sensitivity and selectivity of the sensor film while also lowering the operating temperature [48]. When compared to pure SnO2, Au-doped SnO2 responds strongly to CO, but when it comes to transition metals like Cu, Cu-doped SnO2 increases the reactivity of tin oxide to CO [2.45].

There are only two types of sensitization mechanisms proposed, chemical sensitization and electronic sensitization, for improving the sensing response of gas with respect to noble metals reported in 1983 by Yamazoe et al [2.46]. Morrison also reported the understanding of the two models by noble additives, the spill-over and Fermi-level control, which have the advantage of simplicity but do not explain the sensitization complexity by metal oxide additives. The complexity is caused by the gas sensing performance, material reactivity, common surface chemistry, and the electronic result [2.47].

Furthermore, Seiyama et al. explained in 1972 that additives modifying SMOs surface under specific conditions promote sensitivity and response rate, and Yamazoe et al. discovered an inverse relationship between response and grain size in 1991 on his studies, by adding dopants on a metal for modifying the synthetic parameters control the grain size [2.22]. The promoter in chemical sensitization (spill-over) in a semiconductor surface initiates a test gas to aid its catalytic oxidation; the promoter escalates gas sensitivity as the rate of chemical process increases, whereas the concentration of negatively charged oxygen adsorbed in the surface drops; the promoter has no effect on resistance, implying the gas sensing mechanisms remain constant, as illustrated in fig 2.4.a. [2.48].

In electronic sensitization, the noble metals operate as accepters on the semiconductor oxide surface, increasing the depletion layer, the noble metal doped metal oxide resistance changing much more than the basic metal oxide, and thereby increasing the gas response [2.49].

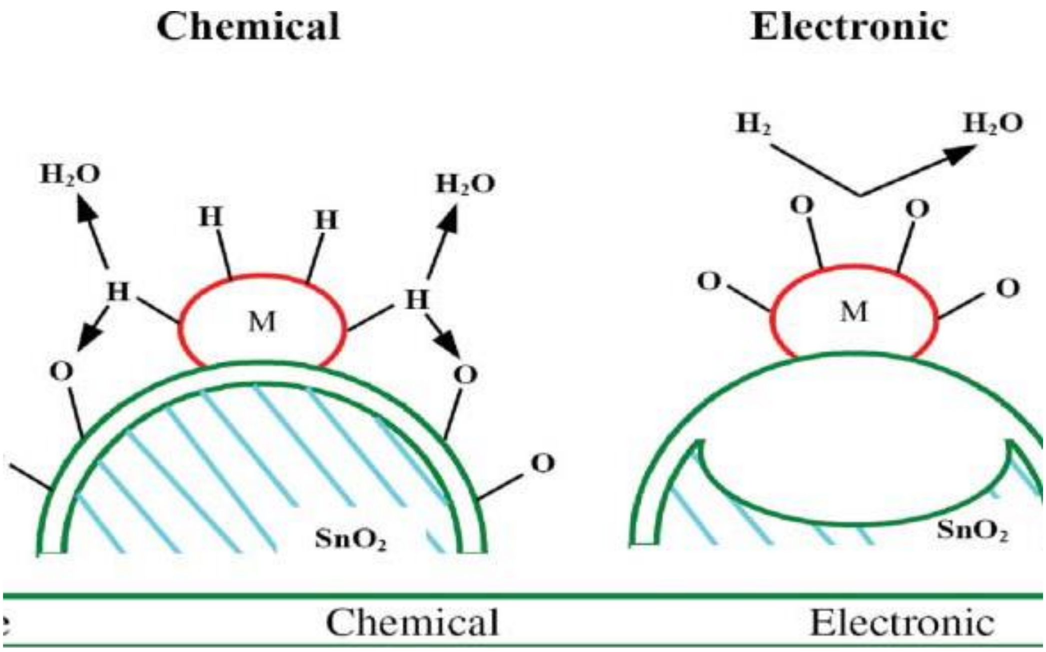

Fig. 2.4: The illustration of (a) chemical sensitization and (b) electronic sensitization of the promoter on SnO_2 surface [2.46].

2.6. Tin Dioxide.

This section provides and overview of tin dioxide, its properties and structure.

2.6.1. Bulk properties of Tin dioxide (SnO_2).

Tin dioxide (SnO_2) is a vital semiconductor metal oxide metal owing to its distinctive properties which includes low cost, and non-toxic [2.50]. SnO_2 has been used in many applications such as gas sensors [2.51], solar cell [2.52], transparent electrodes [2.53], catalyst, surge arrestors [2.54], radioactive waste management, and optoelectronic devices [2.55],

2.6.2. Gas sensing properties of SnO_2.

Due to qualities such as low cost, high sensitivity, chemical stability, high crystallinity, and ease to use, SnO_2 semiconductor was considered one of the successful materials for gas sensing application in earlier studies/literature [2.56]. The synthesis of SnO_2 gas sensors has used a variety of methods, including autoclave hydrothermal, sol gel, and co-precipitation [2.57, 2.58], spray pyrolysis, chemical vapor deposition [59] and combustion route [2.60].

Researchers have previously faced several obstacles when attempting to improve sensor performance by focusing on gas selectivity, operating temperature (low temperature, to conserve energy), stability, responsiveness, and sensitivity of gas sensors. As a result, average reports on pure SnO_2 and doped SnO_2 material sensors have been compiled and published, regardless of the problems encountered. Khuspe et al. [2.61] observed a response of 4.5 for 100ppm concentration of NO_2 generated by sol gel technique at a temperature of 50^{o}C. Using pure SnO_2 at room temperature, Xu et al. [2.54] found a response of 10ppm NO_2 and NH_3, as well as 1000ppm CO, ethanol, and H_2 gases using pure SnO_2 at RT where the sensors exhibited high response for NO_2 gas.

High sensitivity of SnO_2 nanoparticle is dependent of larger surface area where oxygen adsorption or desorption can take place, and by reducing the size of nanoparticle, SnO_2 sensors exhibit good performance towards various gases [2.55, 2.62].

SnO_2 is n-type semiconductor material, it is an electron carrier. The molecules of oxygen from the atmosphere (ambient air) are adsorbed on the surface of SnO_2 material forming oxygen ions, therefore the oxygen ions extract electrons from conduction band of SnO_2 forming depletion layer and restoring the flow of electrons therefore the resistance increases. Then when reducing gas is introduced such as CH_4, CO or H_2, it donates back the electrons to the SnO_2 material occupying empty electron vacancies and eradicating the depletion layer (depletion layer become thinner), therefore the resistance of the SnO_2 material decreases as flow of charges increases. When oxidising gas such as NO_2, O_3 or CO_2 is introduced to the surface of the SnO_2 material, it extracts more electrons from the conduction band which result in the increased width of the depletion layer. The electrons flow decreases, then the resistance increases. In Fig. 2.5, illustrate the decrease in potential barriers of SnO_2 when reducing gas is introduce to its surface.

Porosity also plays a crucial role in the interaction of the reagent and the material, it allows reagent to pass in and out through it. Nanoparticle porosity adjustments have also been shown to improve sensitivity [2.63]. The porous interconnected sensor surface enhances gas sponginess, adsorption, and desorption rates, affecting the sensor's response and recovery times [2.64]. Porous non-silica metal oxide submicrospheres with large surface areas and well-developed porosity can be created to increase interfacial interactions with reactants and to facilitate reactant and product transport and diffusion [2.65].

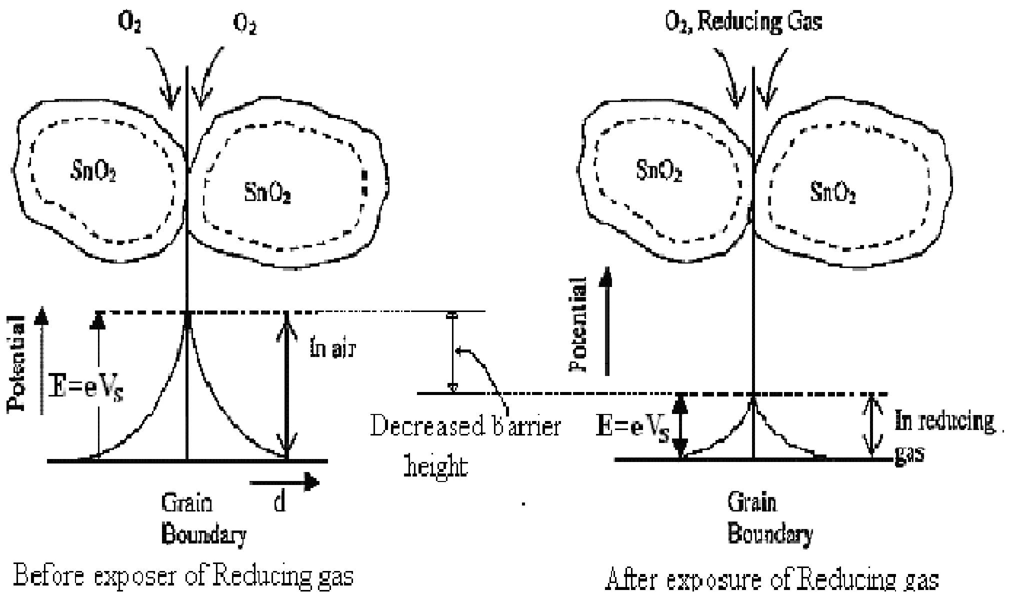

Fig. 2.5: The schematic illustration of SnO_2 gas sensing mechanism before and after exposure to reducing gas, highlighting the change in potential barriers [2.66].

2.6.3. Electrical and optical properties of SnO_2.

Due to the presence of intrinsic imperfection, oxygen vacancies (V_O), and tin interstitials, SnO_2 semiconductor has an n-type conductivity with a wide bandgap of around 3,6 eV. The tin interstitials donor level is fully ionized in the conduction band, but the single ionized oxygen vacancies (V_O^-) and double ionized oxygen vacancies (V_O^{2-}) donor levels associated to oxygen vacancies are located (0.03 and 0.15eV below the bottom of the CB). The defects are mostly oxygen vacancies that are positioned on the surface due to the high volume to ratio in the material, which helps trap surface electrons [V_O^{2-}] acts as shallow donor and (V_O^-) acts as deep donor [2.67-2.69].

SnO_2 is a good insulator in its stoichiometric state, but nonstoichiometry, or oxygen insufficiency, enhances its conductivity. The donor features of regular native defects have been empirically validated, despite the scattered values. The production energy of oxygen vacancies and tin interstitials in SnO_2 is quite low, according to Kilic and

Zunger [2.70]. These defects can then quickly form, and defect levels can be easily ionized [2.71].

2.6.4. Magnetic properties of SnO_2.

The Co-doped TiO_2 was reported the first oxide metal discovered at room temperature to be ferromagnetic, since then additional investigation on ferromagnetism on various dilute magnetic semiconductor (DMS) such as In_2O_3, ZnO, Cu_2O and SnO_2 that exhibit ferromagnetic behaviour near, or above room temperature have been undertaken [2.72-2.74]. It has been reported that pure SnO_2 display low RT-ferromagnetism because of intrinsic defects such as oxygen vacancies (V_o) and tin interstitial (Sn_i), therefore researchers have found doping metal oxide with transition metal beneficiary to stabilize ferromagnetic [2.75]. Fig. 2.6, show the magnetic properties of Co doped SnO_2.

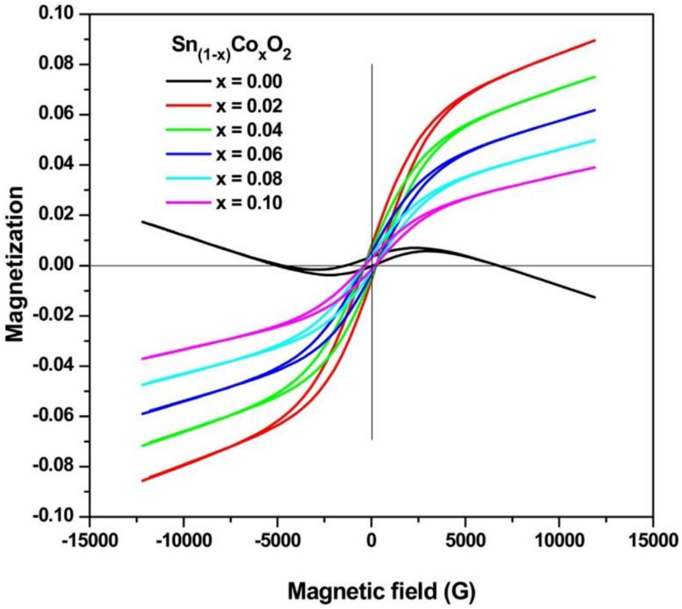

Fig. 2.6: M-H hysteresis curves of $Sn_{1-x}Co_xO_2$ (with $0 \leq x \leq 0.10$) nanoparticles [2.76].

2.6.5. Surface properties of SnO_2.

Surface and interface properties plays a crucial role for contact formation, gas adsorption, and oxygen exchange behaviour [2.77]. SnO_2 material have multiple layers, therefore its surface properties can be enhanced by removing the upper most layer especially oxygen layer [2.78]. SnO_2 surface can be improved by chemical or electronic sensitization and by addition of additives (dopants/impurities) such as Pt, Pd, Au and Ag which acts as sensitizers or catalyst [2.79, 2.80] and addition of dopants may result in the increase in SnO_2 powder surface area [2.81]. Different cation such as Ni, Mn, Fe, Mg were discovered to change the surface chemistry of SnO_2 particles at low temperature, influencing the selectivity to gases, particle behaviour in suspension and as a function of dopants concentration the grain size and crystallinity is decreased [2.82, 2.83].The interaction of material and reagent depend also on the size and surface area of the material, the surface area of the particle increases with the decrease in size of the nanoparticle [2.80].

The surface enables the interaction of SnO_2 and gases which promotes the high concentrated charge transfer to ensure high conductivity and the creation of defects during sintering of this oxide [2.84]. Surface properties of SnO_2 are also govern by dual valency of Sn. Therefore, depending on the oxygen chemical potential of the system, the dual valency permits a reversible shift of the surface composition from stoichiometric surfaces with Sn^{4+} surface cations reduced to surface with Sn^{2+} surface cations [2.85, 2.86]. Sn and V_0 are the defects in SnO_2, but V_0 is considered the main defects. SnO_2 is dominated by (110), (100) and (101) facets and the (110) plane is the most studied due to its higher stability [2.87, 2.88].

2.6.6. Structural properties of SnO_2.

The tin (Sn) and oxygen (O) atoms (illustrated in Fig. 2.7) has been arranged to form tetragonal rutile structure of tin oxide (SnO_2) with a space group symmetry of P42/mnm [89]. The unit cell of tin oxide contains atoms, two Sn atoms and four O atoms, six oxygen anions located at the apex of a normal octahedron surround each tin cation, and each oxygen is surrounded by three tin atoms located at the apex of an equatorial triangle [2.90, 2.91]. The lattice parameters of stannic oxide are a = b = 4.731 Å and c = 3.189 Å [2.92]. The Sn atoms are positioned at (000) and (½, ½, ½) whereas O atoms are positioned at ± (0, 0, 0) and ± (½+u, ½-u, ½) planes of the BCC to form a distorted tetrahedron [2.93]. The dual valency of Sn is a key to understanding some features of SnO_2 surface characteristics. The dual valency enables a reversible shift of the surface composition from stoichiometric surfaces with Sn^{+4} surface cations to a reduced surface with Sn^{+2} surface cations depending on the system's oxygen chemical potential. Surface reduction alters the surface electronic structure by creating surface states obtained from Sn 5s that are located deep within the band gap [2.94, 2.95].

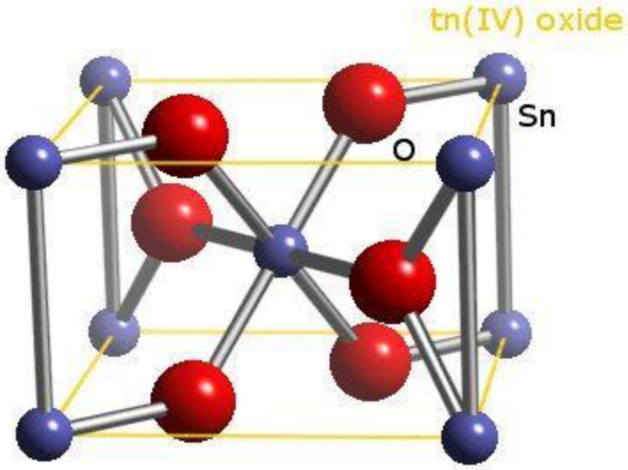

Fig. 2.7. Tetragonal structure of tin Oxide, the red spheres represent oxygen atoms and purple sphere represent tin atoms.

Table 2.1: The gas sensing performance of SnO_2 gas sensors.

Sensing materials	Deposition methods	Working Temperature (°C)	Analyte gas	Concentration (ppm)	Sensor response	Ref.
SnO_2	Sol-gel	200	NO_2	100	19	[2.61]
Fe-SnO_2	Pechini method	25	H_2S	25	79	[2.96]
Ag/PANI/SnO_2	polymerization	20	SO_2	50	20	[2.97]
SnO_2@rGO	hydrothermal	25	CH4	1000	5	[2.98]
Pt-SnO_2	precipitation	25	CH_4	100	29	

Table 2.1 compares the sensors response of the fabricated pure SnO_2 and doped SnO_2 by various noble metals, different techniques has been deployed in the synthesis of the sensors. The gases such as H_2S, SO_2, CH_4 and NO_2 of different concentrations as listed in table 2.1 exhibited unequal responses when exposed to the gas sensor at various operating temperature. The decorated sensors have higher response compared to the undoped sensors. Researchers reported that doping material with noble metals increases the sensitivity, response time and recovery time of the material when exposed to different gas.

2.7. Vanadium Pentoxide (V_2O_5).

V_2O_5 is an n-type semiconductor with a band gap of 2,38eV and it has an orthorhombic structure separated by van der Waals's force between its layers, it has been reported as both single crystal's structure and amorphous V_2O_5 layer [99] which make it suitable for wide applications such as gas sensor, catalysis [2.100-2.102], infrared detectors [2.103], solar cell [2.104], and cathode for Li ion batteries [2.105]. V_2O_5 crystal has oxygen vacancies (V_o) as its vital defects [106]. The formation of oxygen vacancies is when V_2O_5 is heated in vacuum and loses oxygen which results in dislocation and oxygen being removed from V_2O_5 [2.107], and the oxidation state of the adjacent vanadium atoms changes from V^{+5} to V^{+4} due to the presence of V_o defects [2.108].

2.8 Copper Oxide (CuO).

Copper oxide, CuO is a transition metal oxide with a p-type behaviour and narrow band gap of 1.2eV at room temperature [2.109, 2.110]. CuO has attracted interest in research due to its unique properties in various fields such as in catalysis [2.111], gas sensors [2.112], high temperature superconductors [2.113], electrode in lithium ion batteries [2.114], varistor etc. [2.115], and characterized by low cost, excellent chemical stability and environmental friendliness [2.116-2.118], easy to manufacture and non-poisonous [2.120]. CuO materials consist of monoclinic structure and various attractive characteristics, such as super thermal conductivity, high stability, antimicrobial activity and photovoltaic properties [2.119].

2.9. References.

2.1. Fatima Ezahra Annanouch. Design, Optimization and Characterization of Metal Oxide Nanowire Sensors. 2015. 7-13.

2.2. Giovanni Neri. First Fifty Years of Chemoresistive Gas Sensors. 2015. 1-11

2.3. Sofian M. Kanan. Oussama M. El-Kadri. Imad A. Abu-Yousef. Marsha C. Kanan. Semiconducting Metal Oxide Based Sensors for Selective Gas Pollutant Detection. 2009. 8158-8159.

2.4. G. Korotcenkov. Metal oxides for solid-state gas sensors: What determines our choice? 2007. 2.

2.5. Chengxiang Wang, Longwei Yin. Luyuan Zhang. Dong Xiang and Rui Gao. Metal Oxide Gas Sensors: Sensitivity and Influencing Factors.2010. 2088-2100.

2.6. Chandran Balamurugan. Sun-Ju Song. Ho-Sung Kim. Enhancing Gas Response Characteristics of Mixed Metal Oxide Gas Sensors. 2017. 2-3.

2.7. Priyanka Karnati, Sheikh Akbar∗ , Patricia A. Morris. Conduction mechanisms in one dimensional core-shell nanostructures for gas sensing: A review.2019. 127.

2.8. Raivo Jaaniso. Ooi Kiang Tan. Semiconductor gas sensors. 2013. 221.

2.9. Ananya Dey. Semiconductor metal oxide gas sensors: A review. 2018. 206-213.

2.10. Daniel Thevenot, Klara Toth, Richard Durst, George Wilson. Electrochemical biosensors: recommended definitions and classification. 2013. 2335.

2.11. Nazar Abbas Shah. Majeed Gul. Murrawat Abbas Muhammad Amin. (N.d.). Synthesis of Metal Oxide Semiconductor Nanostructures for Gas Sensors. 4-6.

2.12. Yu-Feng Sun. Shao-Bo Liu. Fan-Li Meng. Jin-Yun Liu. Zhen Jin. Ling-Tao Kong. Jin-Huai Liu. Metal Oxide Nanostructures and Their Gas Sensing Properties:A Review. 2012. 2614-2615.

2.13. Swati Sharma. Marc Madou. A new approach to gas sensing with Nanotechnology. 2012. 2453- 2454.

2.14. Ruchika. Ashok Kumar. Performance analysis of Zinc oxide based alcohol sensors. 2015. 430-431.

2.15. Francesca D’Anna. Maria Luisa Grilli. Rita Petrucci. Marta Feroci. WO_3 and Ionic Liquids: A Synergic Pair for Pollutant Gas Sensing and Desulfurization. 2020. 3.

2.16. Avner Rothschilda. Yigal Komem. The effect of grain size on the sensitivity of nanocrystalline metal-oxide gas sensors. 2004. 6374-6375.

2.17. Argha Sarkar. Santanu Maity. Pinaki Chakraborty. Swarnendu Kr. Chakraborty. Synthesize of ZnO Nano structure for toxic gas sensing application. 2016. 201.

2.18. Zhijie Li. Hao Li. Zhonglin Wu. Mingkui Wang. Jingting Luo. Hamdi Torun. PingAn Hu. Chang Yang, f Marius Grundmann. Xiaoteng Liu. YongQing Fu. Advances in designs and mechanisms of semiconducting metal oxide nanostructuresfor high-precision gas sensors operated at room temperature. 2019. 472.

2.19. Milua Masikini. Mahabubur Chowdhury. Ouassini Nemraoui. Review—Metal Oxides: Application in Exhaled Breath Acetone Chemiresistive Sensors. 2020. 6-8.

2.20. Tingting Lin. Xin Lv. Zhineng Hu. Aoshu Xu. Caihui Feng. Semiconductor Metal Oxides as Chemoresistive Sensors for Detecting Volatile Organic Compounds. 2019. 4-11.

2.21. Hongseok Kima, Zhicheng Caib, Sung-Pil Changa, Sunghoon Park. Improved sub-ppm acetone sensing properties of SnO_2 nanowire-based sensor by attachment of Co3O4 nanoparticles. 2020. 1134.

2.22. Prabakaran Shankar. John Bosco Balaguru Rayappa. Gas sensing mechanism of metal oxides: The role of ambient atmosphere, type of semiconductor and gases - A review. 2014. 2-5.

2.23. D.S.Ballantine.Jr. S.J.Martin. A.J.Ricco. G.C.Frye. H.Wohltjen R.M.White. E.T.Zellers. Chapter 5 - Chemical and Biological Sensors. 1997. 239-247.

2.24. Enobong Effiong Bassey. Deveopment and characterisation of metal oxide gas sensor. 2014. 39-46.

2.25. https://www.maximintegrated.com/en/glossary/definitions.mvp/term/Response%20Time/gpk/928.

2.26. David L. Safranski (N.d.). Introduction to Shape-MemoryPolymers David L. Safranski. 16.

2.27. E. Bochenkov, G. B. Sergee V. (N.d.). Sensitivity, Selectivity, andStability of Gas-SensitiveMetal-Oxide NanostructuresV. 33.

2.28. Hyo-Joong Kim, Jong-Heun Lee. Highly sensitive and selective gas sensors using p-type oxidesemiconductors: Overview. 2013. 608-609.

2.29. Sina Wrede. Haining Tian. Towards sustainable and efficient p-type metal oxide semiconductor materials in dye-sensitised photocathodes for solar energy conversion. 2020. 13854.

2.30. Seong-Yong Jeong. Jun-Sik Kim. Jong-Heun Le. Rational Design of Semiconductor-Based Chemiresistors and their Libraries for Next-Generation Artificial Olfaction. 2020. 5-9.

2.31. Mark T Greiner. Zheng-Hong Lu. Thin-film metal oxides in organic semiconductor devices: their electronic structures, work functions and interfaces.2013. 5-6.

2.32. Anil Kumar. Mukesh Kumar. Ravi Kumar. Rakesh Singh. B. Prasad. Dinesh Kumar. Numerical model for the chemical adsorption of oxygen and reducing gas molecules in presence of humidity on the surface of semiconductor metal oxide for gas sensors applications. 2018. 236.

2.33. ZHENG XiaoQi. CHENG HuanYu. Flexible and stretchable metal oxide gas sensors for healthcare. 2018. 211.

2.34. Abdulnasser Nabil Abdullah. Kamarulzaman Kamarudin. Syed Muhammad Mamduh. Abdul Hamid Adom. Zaffry Hadi Mohd Juffry. Effect of Environmental Temperature and Humidity on Different Metal Oxide Gas Sensors at Various Gas Concentration Levels. 2020. 2.

2.35. Ali Mirzaei. Jae-Hyoung Lee. Sanjit Manohar Majhi. Matthieu Weber. Mikhael Bechelany. Hyoun Woo Kim. Sang Sub Kim. Resistive gas sensors based on metal-oxide nanowires. 2019. 126-127.

2.36. Sven Jonda. Max Fleischer. Hans Meixner. Temperature control of metal-oxide gas sensors by fuzzy logic. 1996. 396.

2.37. Rahul Kumar. Xianghong Liu. Jun Zhang. Mahesh Kumar. Room-Temperature Gas Sensors Under Photoactivation: From Metal Oxides to 2D Materials. 2020. 2.

2.38. Kyoungjin Hwang. Junseong Ahn. Incheol Cho. Kyungnam Kang. Kyuyoung Kim. Jungrak Choi. Kyriaki Polychronopoulou. Inkyu Park. Microporous Elastomer Filter Coated with Metal Organic Frameworks for Improved Selectivity and Stability of Metal Oxide Gas Sensors. 2020. 13338.

2.39. A. Mirzaei. B. Hashemi. K. Janghorban. a-Fe_2O_3 based nanomaterials as gas sensors. 2019. 3111.

2.40. Krystyna Schneider. Wojciech Maziarz. V_2O_5 Thin Films as Nitrogen Dioxide Sensors. 2018. 2.

2.41. S. Basu. P. K. Basu. Nano-crystalline Metal Oxides for Methane Sensors: Role of Noble Metals. 2009. 6-7.

2.42. Adeel Afzal. β-Ga_2O_3 nanowires and thin films for metal oxide semiconductor gas sensors: Sensing mechanisms and performance enhancement strategies. 2019. 547.

2.43. Supab Choopun. Niyom Hongsith. Ekasiddh Wongrat. (n.d). Metal-Oxide Nanowires for Gas Sensors. 3.

2.44. S. Mohammad-Yousefi. S. Rahbarpour. H. Chafoorifard. The effect of noble metal additives on the optimum operating temperature of SnO_2 gas sensors. 2017. 1-2.

2.45. Jeyapaul Sam Jebakumar and Asokan Vimala Juliet. Palladium-Doped Tin Oxide Nano-sensor for the Detection of the Air Pollutant Carbon Monoxide Gas. 2020. 3-4.

2.46. Zain Ul Abideen. Jae-Hun Kim. Jae-Hyoung Lee. Jin-Young Kim. Ali Mirzae. Hyoun Woo Kim. Sang Sub Kim. Electrospun Metal Oxide Composite Nanofibers Gas Sensors: A Review. 2017. 374.

2.47. David Degler. Udo Weimar. Nicolae Barsan. Current Understanding of the Fundamental Mechanisms of Doped and Loaded Semiconducting Metal-Oxide-Based Gas Sensing Materials. 2019. 2228- 2230.

2.48. Guruviah Velmathi. Sanganeni Mohan. Rabinder Henry. Analysis of Factors for Improving Functionality of Tin Oxide Gas Sensor. 2015. 1-4.

2.49. Prabhakar Rai. Sanjit Manohar Majhi. Yeon-Tae Yu. Jong-Heun Lee. Noble metal@metal oxide semiconductor core@shell nano-architectures as a new platform for gas sensor applications. 2015. 76231.

2.50. Archita Bhattacharjee. M. Ahmaruzzaman. Tanur Sinha. A novel approach for the synthesis of SnO_2 nanoparticles and its application as a catalyst in the reduction and photodegradation of organic compounds. Spectrochimica Acta Part A: Molecular and Biomolecular Spectroscopy. (2015). 136. p751-760.

2.51. Ganhua Lu. Kyle L. Huebner. Leonidas E. Ocola. Marija Gajdardziska-Josifovska. Junhong Chen. Gas Sensors Based on Tin Oxide Nanoparticles Synthesized from a Mini-Arc Plasma Source. Journal of Nanomaterials. (2006). Volume 2006. p1-7.

2.52. Simin Tazikeh. Amir Akbari. Amin Talebi. Emad Talebi. Synthesis and characterization of tin oxide nanoparticles via the Co-precipitation method. Materials Science-Poland. (2024). 32(1). p98-101.

2.53. Madzlan Aziz. Saad Saber Abbas. Wan Rosemaria Wan Baharom. Size-controlled synthesis of SnO_2 nanoparticles by sol–gel method. Materials Letters. (2013). 91. 31-34.

2.54. C. Ararat Ibarguen. A. Mosquera. R. Parra. M.S. Castro. J.E. Rodr´ıguez-Paez. Synthesis of SnO_2 nanoparticles through the controlled precipitation route. Materials Chemistry and Physics. (2007). 101. p433–440.

2.55. Fatemeh Davar. Masoud Salavati-Niasari. Zienab Fereshteh. Synthesis and characterization of SnO_2 nanoparticles by thermal decomposition of new inorganic precursor. Journal of Alloys and Compounds. (2010). 496. p638–643.

2.56. Amrit P. Sharma. Pashupati Dhakal. Dhiren K. Pradhan. Makhes K. Behera. Bo Xiao. Messaoud Bahoura. Fabrication and characterization of SnO_2 nanorods for room temperature gas sensors. AIP ADVANCES 8, (2018). p 095219-1.

2.57. Lin Tan. Lihong Wang. Yude Wang. Hydrothermal Synthesis of SnO_2 Nanostructures with Different Morphologies and Their Optical Properties. Journal of Nanomaterials.(2011). Volume 2011, Article ID 529874. p1.

2.58. S.Sasikala. R. Thanal. A. Kanimozhi. S. Siva. Synthesis and characterization of zinc doped tin oxide Nanoparticles by co-precipitation method. JETIR.(2018). Volume 5. p974.

2.59. Ganesh E Patil. Dnyaneshwar D Kajale. Vishwas B Gaikwad. Gotan H Jain. Preparation and characterization of SnO_2 nanoparticles by hydrothermal route. International Nano Letters (2012). 2:17. p1-5.

2.60. T. Krishnakumar. R. Jayaprakash. Nicola Pinna. A.R. Phani. M. Passacantando. S. Santucci. Structural, optical and electrical characterization of antimony-substituted tin oxide nanoparticles. Journal of Physics and Chemistry of Solids. (2009). 70. p993–999.

2.61. G.D. Khuspe. R.D. Sakhare. S.T. Navale. M.A. Chougule. Y.D. Kolekar. R.N. Mulik. R.C. Pawar. C.S. Lee. V.B. Patil. Nanostructured SnO_2 thin films for NO_2 gas sensingapplications. Ceramics International 3. (2013). p8673–8679.

2.62. S.Sasikala. R. Thanal. A. Kanimozhi. S. Siva. Synthesis and characterization of zinc doped tin oxide Nanoparticles by co-precipitation method. JETIR.(2018). Volume 5. p974.

2.63. Min Ah Han. Hyun-Jong Kim. Hee Chul Lee. Jin-Seong Park. Ho-Nyun Lee. Effects of porosity and particle size on the gas sensing properties of SnO2 films.

Applied Surface Science. (2019). https://doi.org/10.1016/j.apsusc.2019.03.043.

2.64. Songlin Li. Min Zhang. Hai Wang. Simulation of gas sensing mechanism of porous metal oxide semiconductor sensor based on finite element analysis. Scientific reports. (2021). 11. p1-11.

2.65. Yash Boyjoo. Meiwen Wang. Vishnu K. Pareek. Jian Liu. Mietek Jaroniec. Synthesis and applications of porous non-silica metal oxide submicrospheres. The Royal Society of Chemistry (2016). 45. p6013-6047.

2.66. Manal Madhat Abdullah. Mahdi Hassan Suhail. Sabah Ibrahim Abbas. Fabrication and Testing of SnO_2 Thin Films as a Gas Sensor. Archives of Applied Science Research. (2012).4 (3). p1279-1288.

2.67. Saleem Azara Hussain. Rashid Owaid Kadhim. Sura Noaman Tarrad. Structural and optical properties of Tin Oxide and Indium doped SnO_2 thin films deposited by thermal evaporation technique. Journal of Advances in Physics. (2016). Volume 12. p4394.

2.68. Pedro H. Suman. Electrical properties of tin oxide materials. (.N.D). P41-42. https://doi.org/10.1016/B978-0-12-815924-8.00003-7.

2.69. Sumaira Mehraj. M. Shahnawaze Ansari. Attieh A. Al-Ghamdi. Alimuddin. Annealing dependent oxygen vacancies in SnO_2 nanoparticles: Structural, electrical and their ferromagnetic behavior. Materials Chemistry and Physics.171. (2016). 109-118.

2.70. Lin Tan. Lihong Wang. Yude Wang. Hydrothermal Synthesis of SnO_2 Nanostructures with Different Morphologies and Their Optical Properties. Journal of Nanomaterials.(2011). Volume 2011, Article ID 529874. p1.

2.71. Celso M. Aldao. Surface and interface electronic properties of tin oxide.(.N.D). . https://doi.org/10.1016/B978-0-12-815924-8.00005-0.

2.72. Jasneet Kaur. Jyoti Shah. R.K. Kotnala. Kuldeep Chand Verma. Raman spectra, photoluminescence, and ferromagnetism of pure, Co and Fe doped SnO2 nanoparticles. Ceramics International. (2012). 38. p5563–5570.

2.73. Z.M. Tian. S.L. Yuan. J.H. He. P. Li. S.Q. Zhang. C.H. Wang. Y.Q. Wang. S.Y. Yin. L. Liu. Structure and magnetic properties in Mn doped SnO_2 nanoparticles synthesized by chemical co-precipitation method. Journal of Alloys and Compounds. (2008). 466.p26–30.

2.74. He Jianga. Xiao Fang Liu. Zhi Yu Zou. Zhang Ben Wu. Bo He. Rong Hai Yu. The effect of surfactants on the magnetic and optical properties of Co-doped SnO2 nanoparticles. Applied Surface Science. (2011). 258. p236–241.

2.75. Yuting Fu. Ning Sun. Long Feng. Shuai Wen. Yukai An. iwen Liu. Local structure and magnetic properties of Fe-doped SnO2 films. Journal of Alloys and Compounds. (2017). 698 . p863-867.

2.76. N. Afify. Gh. Abbady. D. Hamad. R.F. Abdelbaki. El Sayed Yousef. E.R. Shaabane. Mohamed N. Abd-el Salam. The effective role of dilute Co on SnO2 nanoparticles: Structural, optical and magnetic characterization properties for spintronics. Sensors and Actuators A. (2021). 331. p1-9.

2.77. Karsten Rachut. Christoph Körber. Joachim Brötz. Andreas Klein. Growth and surface properties of epitaxial SnO_2. Physica Status Solidi A 211. (2014). No. 9. p1997–2004.

2.78. Matthias Batzill. Khabibulakh Katsiev. James M. Burst. Yaroslav Losovyj. Wolfgang Bergermayer. Isao Tanaka. Ulrike Diebold. Tuning surface properties of SnO2(1 0 1) by reduction. Journal of Physics and Chemistry of Solids. (2006). 67. p1923–1929.

2.79. Zain Ul Abideen. Jae-Hun Kim. Sang Sub Kim. Optimization of metal nanoparticle amount on SnO_2 nanowires to achieve superior gas sensing properties. Sensors and Actuators B. (2017). 238. p374–380.

2.80. A. Borhaninia. A. Nikfarjam. N. Salehifar. Gas sensing properties of SnO_2 nanoparticles mixed with gold nanoparticles. Trans. Nonferrous Met. Soc. (2017). China 27. p1777−1784.

2.81. L.M. Fang. X.T. Zu. Z.J. Li. S. Zhu. C.M. Liu. W.L. Zhou. L.M. Wang. Synthesis and characteristics of Fe3+-doped SnO_2 nanoparticles via sol–gel-calcination or sol–gel-hydrothermal route. Journal of Alloys and Compounds. (2008). 454. p261–267.

2.82. Ricardo H.R. Castro. Gilberto J. Pereira. Douglas Gouve. Surface modification of SnO2 nanoparticles containing Mg or Fe: Effects on sintering. Applied Surface Science. (2007). 253. p4581–4585.

2.83. Ameer Azama. Arham S. Ahmed. Sami S. Habiba. A.H. Naqvi. Effect of Mn doping on the structural and optical properties of SnO_2 nanoparticles. Journal of Alloys and Compounds. (2012). 523. p83–87.

2.84. J. A. Varela. L. A. Perazolli. E. Longo. E. R. Leite & J. A. Cerri. Effect of atmosphere and dopants on sintering of SnO_2. Radiatron energy and Defects in Sulid. (1997). 146, pp 131- 143.

2.85. Soumen Das. V. ayaraman. SnO2: A comprehensive review on structures and gas sensors. Progress in Materials Science. (2014). 66. p112–255.

2.86. Yoann Porte. Robert Maller. Hendrik Faber. Husam N. AlShareef. Thomas D. Anthopoulosb. Martyn A. McLachlan. Exploring and controlling intrinsic defects formation in SnO2 thin film. Journal of Materials Chemistry C. (2016). 4. P758-765.

2.87. Binaya Kumar Sahu. A. Das. Arun K. Prasad. G. Mangamma. The Role of In-Plane Oxygen Vacancy Defects in SnO_2 Nanoparticles for CH4 Sensing. Journal of Nanoscience and Nanotechnology. (2019). 19. p7764–7770.

2.88. Kostiantyn V. Sopiha. Oleksandr I. Malyi. Clas Persson. Ping Wu. Chemistry of Oxygen Ionosorption on SnO_2 Surfaces. Applied material and interface. (2021). 13. p33664−33676.

2.89. Pedro H. Suman. Electrical properties of tin oxide materials. (2020) 41-60. https://doi.org/10.1016/B978-0-12-815924-8.00003-7.

2.90. Alexander Gaskov. Marina Rumyantseva. Artem Marikutsa. Tin oxide nanomaterials: Active centers and gas sensor properties. (2020). p163-218. https://doi.org/10.1016/B978-0-12-815924-8.00007-4.

2.91. Marcelo Ornaghi Orlandi. Tin oxide materials: synthesis, properties, and application. p4.

2.92. Christina Hartsell Drake. Understanding the Low Temperature Electrical Properties of Nanocrystalline SnO_2 for Gas Sensor Applications. (2007). 7. https://www.proquest.com/docview/304745459?parentSessionId=jMgxw1X8hyqtzUL%2FcrMEAW4JbPR8LrP6Naa2NJ9UrUs%3D&accountid=16460.

2.93. John W. Masika. Stannic Rutile Tetragonal Tin Oxide Ground State and Optical Properties Studied by Local Spin Density Approximation, the Greens Function and Bethe Salpeter Equation. (2015). 33. http://erepository.uonbi.ac.ke/handle/11295/91075.

2.94. Batzill, M.; Diebold, U. The surface and materials science of tin oxide. Progress in Surface Science. (2005).79. 47-154.

2.95. SIMIN TAZIKEH. AMIR AKBARI. AMIN TALEBI. EMAD TALEBI. Synthesis and characterization of tin oxide nanoparticles via the Co-precipitation method. Materials Science-Poland, 32(1), 2014, pp. 98-101.

2.96. S Navazani. M Hassanisadi. M.M Eskandari. Z Talaei. Design ande valuation of SnO2-Pt/MWCNTs hybrid system as room temperature-methanesensor. Synthetic Metals. (2020). 260. p116267.

2.97. Haoyuan Xu. Jianzhong Li. Peidong Li. Junjie Shi. Xuanwen Gao. Wenbin Luo. Highly Efficient SO2 Sensing by Light-Assisted Ag/PANI/SnO_2 at Room Temperature and the Sensing Mechanism. Applied Material and Interfaces. (2021). 13. p49194−49205.

2.98. Shiva Navazani. Ali Shokuhfar. Mostafa Hassanisadi. Aldo Di Carlo. Nikta Shahcheraghi. Fabrication and characterization of a sensitive, room temperature methane sensor based on SnO_2@reduced graphene oxide-polyaniline ternary nanohybrid. Materials Science in Semiconductor Processing. (2018). 88. p139–147.

2.99. H.M.R. Giannetta. C. Calaza. D.G. Lamas. L. Fonseca. L. Fraigi. Electrical transport properties of V_2O_5 thin films obtained by thermal annealing of layers grown by RF magnetron sputtering at room temperature. Thin Solid Films. (2015). 589. p730–734.

2.100. A.A. Manea. M.P. Suryawanshi. J.H. Kimc, A.V. Moholkar. Fast response of sprayed vanadium pentoxide (V_2O_5) nanorods towards nitrogen dioxide (NO_2) gas detection. Applied Surface Science. (2017). 403. p540–550.

2.101. Veena Mounasamy. Ganesh Kumar Mani. Dhivya Ponnusamy. Kazuyoshi Tsuchiya. P.R. Reshma. Arun K. Prasad. Sridharan Madanagurusamy. Investigation on CH_4 sensing characteristics of hierarchical V_2O_5 nanoflowers operated at relatively low temperature using chemiresistive approach. Analytica Chimica Acta. (2020). 1106. p148-160.

2.102. Nitu Singh. Ahmad Umar. Neha Singh. H. Fouad. Othman Y. Alothman. Fozia Z. Haque. Highly sensitive optical ammonia gas sensor based on Sn Doped V_2O_5 Nanoparticles. Materials Research Bulletin. (2018). 108. p266–274.

2.103. Y. Vijayakumar. Ganesh Kumar Mani. M.V. Ramana Reddy. John Bosco Balaguru Rayappan. Nanostructured flower like V_2O_5 thin films and its room temperature sensing characteristics. Ceramics International. (2015).41. p2221–2227.

2.104. R. Suresh. K. Giribabu. R. Manigandan. S. Praveen Kumar. S. Munusamy. S. Muthamizh. V. Narayanan. Characterization and dopamine sensing property of V_2O_5@polyailine nanohybrid. Synthetic Metals. (2014). 196. p151–157.

2.105. B. Etemadi, J. Mazloom, F.E. Ghods. Phase transition and surface morphology effects on optical, electrical and lithiation/delithiation behavior of nanostructured Ce-doped V_2O_5 thin films. Materials Science in Semiconductor Processing. (2017). 61. p99–106.

2.106. Chih-Chiang Wang. Chia-Lun Lu. Fuh-Sheng Shieu. Han C. Shih. Enhanced photoluminescence properties of Ga-doped V_2O_5 nanorods via defect structures. Chemical Physics Letters. (2020). 738. p1-6.

2.107. F.N. Dultsev. L.L. Vasilieva. S.M. Maroshina. L.D. Pokrovsky. Structural and optical roperties of vanadium entoxide sol–gel films. Thin Solid Films. (2006). 510. p255-259.

2.108. Qi Wang. Mathew Brier. Siddharth Joshi. Ajinkya Puntambekar. Vidhya Chakrapani. Defect-induced Burstein-Moss shift in reduced V2O5 nanostructures. PHYSICAL REVIEW B. (2016). 94. p1-12.

2.109. Qiaobao Zhang. Kaili Zhang. Daguo Xu. Guangcheng Yang. Hui Huang. Fude Nie. Chenmin Liu. Shihe Yang. CuO nanostructures: Synthesis, characterization, growth mechanisms, fundamental properties, and applications. Progress in Materials Science. (2014). 50. p208-337.

2.110. S.M Butte. S.A Wanghuley. Optical properties of Cu_2O and CuO. AIP conference Proceedings. (2020). 5. p1-6.

2.111. Shama Rehman, A. Mumtaz, S. K. Hasanain. Size effects on the magnetic and optical properties of CuO nanoparticles. Journal of Nanoparticle Research. (2011). 13. p2497–2507.

2.112. Dahlang Tahir. Sven Tougaard. Electronic and optical properties of Cu, CuO and Cu2O studied by electron Spectroscopy. JOURNAL OF PHYSICS: CONDENSED MATTER. (2012). 24. p1-9.

2.113. Xiaojun Zhang. Dongen Zhang Æ Xiaomin Ni. Jimei Song. Huagui Zheng. Synthesis and electrochemical properties of different sizes of the CuO particles. Journal of Nanoparticles Research. (2008). 10. p839–844.

2.114. Shama Rehman. A. Mumtaz. S. K. Hasanain. Size effects on the magnetic and optical properties of CuO nanoparticles. Journal of Nanoparticles Research. (2011).13. p2497–2507.

2.115. Aleksandar Živkovi´c. Nora H. de Leeuw. Exploring the formation of intrinsic p-type and n-type defects in CuO. Physical Review Materials. (2020). 4. p1-10.

2.116. Dangxin Wu. Qiming Zhang. LSDA+U study of cupric oxide: Electronic structure and native point defects. Physical Review B 73. (2006). 73. P1-6.

2.117. Azad Kumar. Deepak Kuma. Gajanan Pandey. CHARACTERISATION OF HYDROTHERMALLY SYNTHESISED CuO NANOPARTICLES AT

DIFFERENT pH. Technological Advances and Scientific Research. (2016).2 . p166-169.

2.118. Yonglong Shen. MeilanGuo. Xiaohong Xia. GuoshengShao. Role of materials chemistry on the electrical/electronic properties of CuO thin films. Acta Materialia. (2015). 85. p122–131.

2.119. Muhammad Arif Khan. Nafarizal Nayan. Shadiullah. Mohd Khairul Ahmad. Chin Fhong Soon. Surface Study of CuO Nanopetals by Advanced Nanocharacterization Techniques with Enhanced Optical and Catalytic Properties. Nanomaterial. (2020). 10. p1-18.

2.120. Xinhong Zhao. Peng Wang. Zaoxue Yan. Naifei Ren. Room temperature photoluminescence properties of CuO nanowire arrays. Optical Materials. (2015). 42. p544–547.

CHAPTER 3

3. Characterization.

X-ray diffraction was used to analyse structural features such as crystallinity, crystallite size, and so was the samples. Scanning Electron Microscopy (SEM) and transmission electron microscopy (TEM) were utilized to investigate surface appearance, chemical composition, and interior structure. UV-visible and photoluminescence spectroscopy were used to investigate optical characteristics such as the bandgap and point defects. Electron paramagnetic spectroscopy were used to analyze the paramagnetic flaws. The Brunner-Emmet-Teller surface area analyzer was used to evaluate the porosity and surface area of the nanostructures. While x-ray photoelectron spectroscopy was used to investigate the chemical state.

3.1. X-Ray Diffraction.

X-ray diffraction (XRD) is a popular analytical method for determining crystalline structure, measuring internal stress, and the size and shape of crystalline zones. The x-ray beam strikes the material, infiltrating and scattering in various directions, resulting in scattering and incident angles shown in Fig. 3.1. The waves in motion either add up constructively or cancel each other destructively directed Braggs Law (equation 3.1.). (Equation 3.1.).Therefore each material's XRD pattern differs, indicating that each crystalline material has a distinct crystalline structure.

$$n\lambda=2d\sin\Theta \qquad (3.1).$$

where n is an integer (n=1), λ= 1.5418 Å, wavelength of the beam corresponding to Cu Kα emission, d is the lattice spacing between diffracting planes, Θ is the angle between incident x-rays and lattice plane [3.1].

The tetragonal lattice parameter (a=b≠c) for tetragonal phase structure [3.4] is determine by equation 3.2.

$$\frac{1}{d} = \frac{h^2+k^2}{a^2} + \frac{l^2}{c^2} \qquad (3.2)$$

The average dimension of the crystal that create crystalline powder is related to the peak showed by Scherer equation [3.5], see equation 3.3.

$$D = \frac{K\lambda}{\beta cos\theta} \qquad (3.3)$$

Where D is the size of the crystal, λ is the wavelength of x-ray used, β is the full width at half maximum (FWHM) of the peak in radians and K is the proportionality constant, θ is the angle.

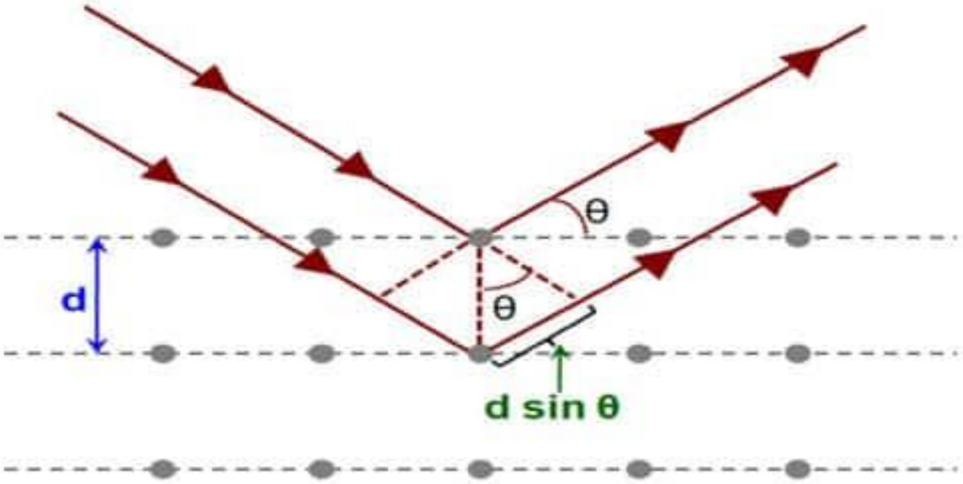

Fig. 3.1. Illustration of Bragg's law [3.2].

3.2. Photoluminescence (PL)

PL is a technique used to identify crystalline quality and purity [3.3]. In PL beam of light traveling in the form of a photon (carrying energy, E=hf) strikes the sample resulting in the energy being transferred (energy is absorbed) to the sample in the process called photo-excitation. The absorbed photons make electrons transition from the valence band to the conduction band of the material. Then, when electrons return to the ground state releases energy which includes the non-radiative process or radiative process as shown in Fig. 3.2 (a). The energy can degenerate through light or luminescence, it is referred to as the photoluminescence process.

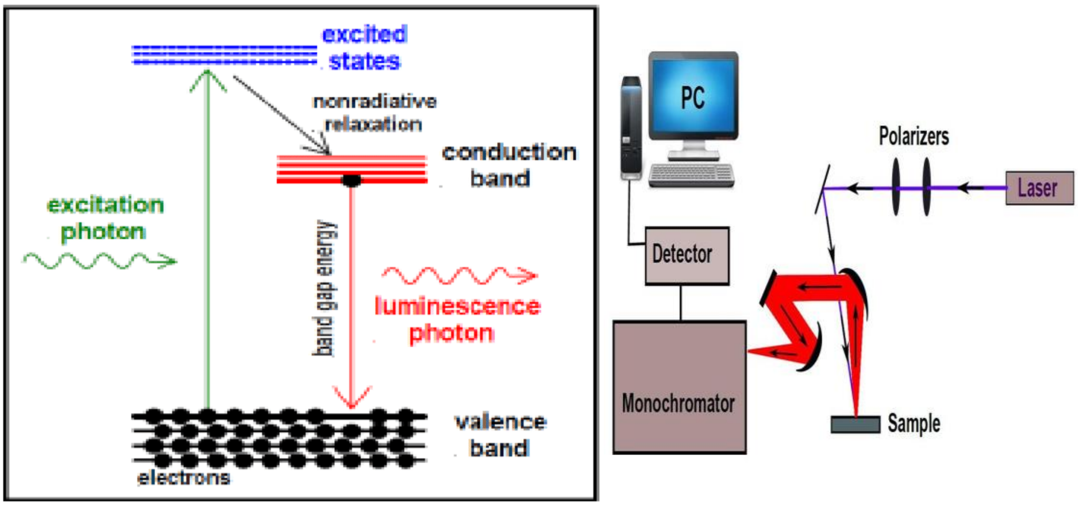

Fig. 3.2. (a) photoluminescence spectroscopy principles [3.6], (b) . Schematic diagram of the PL setup [3.7].

3.3. Scanning Electron Microscopy (SEM).

Scanning electron microscopy (SEM) is an imaging method with a resolution of 2nm used to image the microstructure and morphology of the material. As the low-energy electron beam is transmitted to the material and scans the sample surface, numerous interactions in the surface occur, resulting in the emission of electrons and photons [3.8, 3.9]. An electron probe is scanning over the surface, and there is an interaction between electrons and material at different depths to produce secondary electrons and back-scattered electrons [3.10], electrons are emitted and recorded on the surface of the specimen, and image contrast is achieved by varying the height [3.9]. The texture, size, shape of the features, chemical composition, crystalline structure, and orientation of the sample built in the material are all disclosed by signals from electron-sample interactions (electron beam interacting with specimen) [3.11, 3.12]. The specimen accepts energy generated by incident electrons when it indirectly knocks out an atom, so the electrons are converted to atoms in the specimen, converted electron which discharges the atoms are called the secondary electron, and there will be electron collisions until it reaches the specimen surface [3.13].

The electron cannon emits electron beams, which go via the condense lenses to the pair of deflection coils in the electron column, where they are deflected in the X and Y axes before interacting with the sample. The deflection guarantees that the scan is rectangular [3.10], implying that the sample caught by the rectangular picture displayed in Fig. 3.3. The interaction of the material and electron beams results in energy loss owing to scattering and absorption [3.4, 3.15].

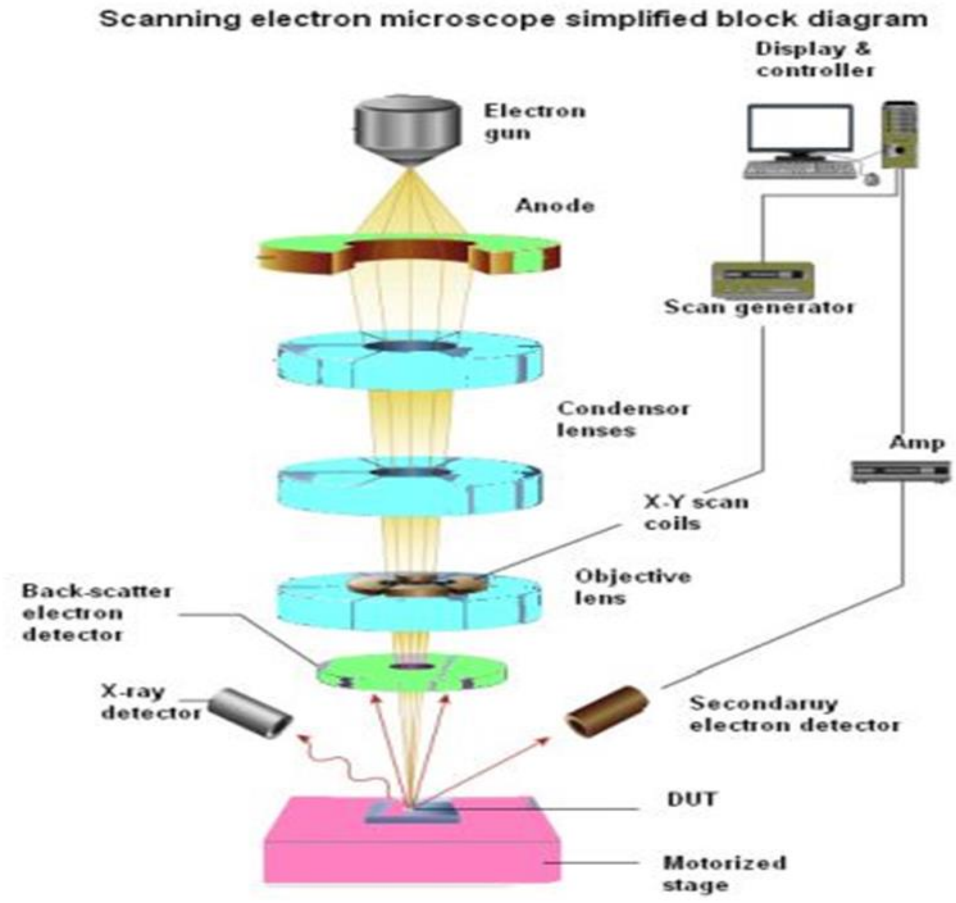

Fig. 3.3. Basic illustration diagram of SEM [3.14].

3.4. Transmission Electron Microscopy (TEM).

Transmission electron microscopy (TEM) is a valuable technique for characterizing nanomaterials. Electron microscopy is used to explore the internal structure of a material and analyze the characteristics at an atomic scale. The TEM has a distinct advantage over the SEM in that it delivers a high spatial resolution. These approaches use transmitted electrons to magnify images, with electron-beam energies ranging from 60 to 350keV [3.16-3.18]. The electron cannon (which creates electron beams and a condenser system to concentrate the beams into an item), the image-recording system, and the image-producing system are the three major structures of a TEM, as illustrated in Fig. 3.4. [3.19]. Because of the interaction of electrons transmitted via the specimen, the picture is expanded and concentrates on the screen (fluorescent screen) [3.20]. TEM uses an extremely high voltage to power the cathode, which subsequently allows the electron beam to generate a picture. The top of the TEM has an electron cannon, which emits electrons and drives them into the microscope vacuum tube. The TEM also employs an electromagnetic (EM) lens, by which electrons are concentrated into a very sufficient beam. The beam is then directed through the extremely tiny object, and electrons impact or scatter the screen at the bottom of the microscope, as seen in fig. 3.3. [3.21, 3.22] formalized paraphrase.

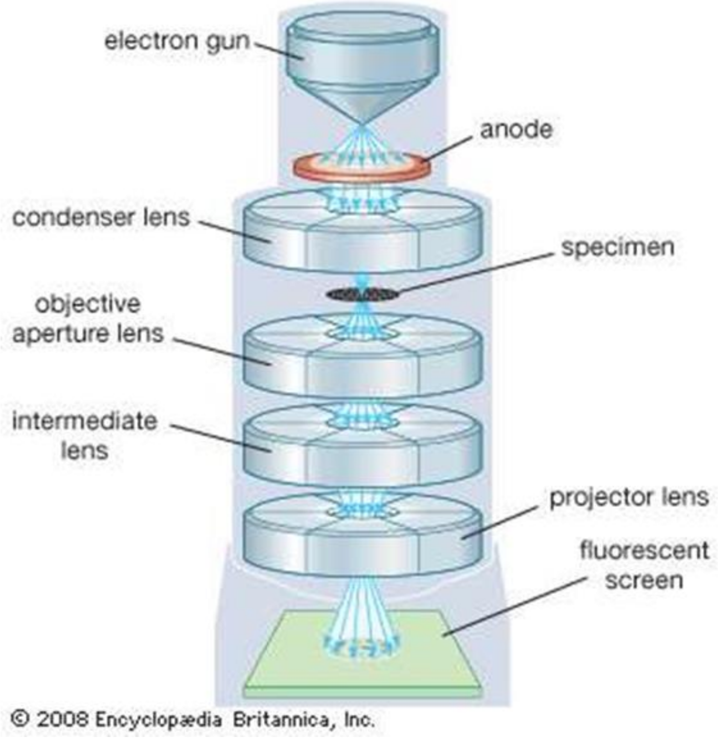

Fig. 3.4. Transmission electron microscopy diagram [3.19].

3.5. Brunauer-Emmett-Teller (Bet).

The Brunauer-Emmett-Teller (BET) theory describes the adsorption of gas molecules on solid surfaces and is used to calculate the surface area of a material. For surface area measurement, this theory applies to a system of two or more layers and employs a probing gas that does not chemically react with the adsorbents on the material's surface. Nitrogen (N_2) is often recognized as the most effective adsorbent for probing using the BET approach. As a result, the N_2 boiling temperature is commonly used in BET analysis. Surface area may be determined at many temperature scales using BET techniques, regardless of their low frequencies, using gases such as argon, carbon dioxide, and water as surface adsorbents [3.23]. The BET equation is as follow:

$$\frac{x}{V(1-x)}=\frac{1}{VmC}+\left(\frac{x.C^\wedge-1}{Vm.C}\right) \qquad (3.4).$$

Where V is the volume of adsorbed molecules, V_m is the monolayer volume, C is the BET constant, and x is the relative pressure (P/P0) [3.25].

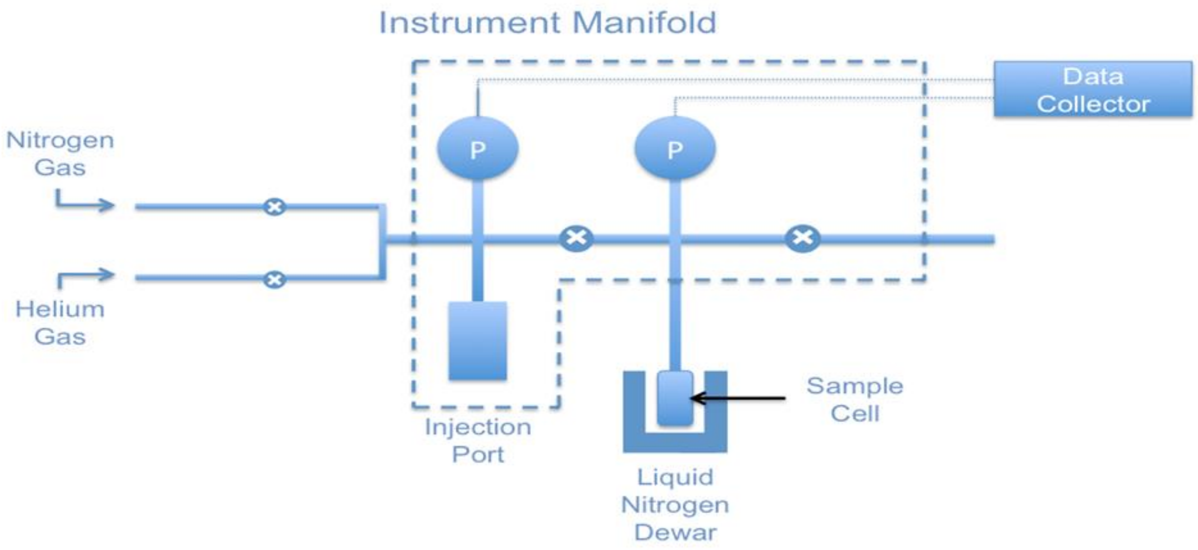

Fig. 3.5. Schematic illustration of BET apparatus [3.24].

3.6. X-Ray Photoelectron Spectroscopy (XPS).

X-ray photoelectron spectroscopy (XPS) is a technique for determining the elemental composition, chemical state, empirical formula, and electronic state of material [3.26-3.28]. The XPS technique includes the measurement of photoelectrons produced by the sample because of single energy x-ray photon irradiation [3.29]. The XPS spectrum is obtained by measuring the number of electrons and their kinetic energy [3.30, 3.31].

In 1887, Hertz discovered the photoelectric effect, which became the cornerstone of this approach. It is expanded in XPS that electrons are released by irradiation light on the material surface, and Rutherford came up with the equation 3.5 after the photoelectric effect in 1914, which explains the electron energy measured as the difference of x-ray energy and electron energy [3.32] as:

$$E_k=hv - E_B \tag{3.5}$$

In the instance of Maxwell's theory, the electron energy is directly proportional to light intensity, but this was not confirmed experimentally, it later revealed that emitted electron energy is accurately proportional to incident light frequency. Furthermore, Albert Einstein proposed that light energy is distributed discontinuously across space. The light is composed of energy quanta, which he subsequently dubbed photons, with energy HV, where h is Planck's constant, and V is light frequency. The emission occurs if the energy gained by the electron in the solid material exceeds the least amount of energy required for the electron to depart the surface (work function) [3.33]. Fig.3.6 shows the schematic diagram of an XPS setup.

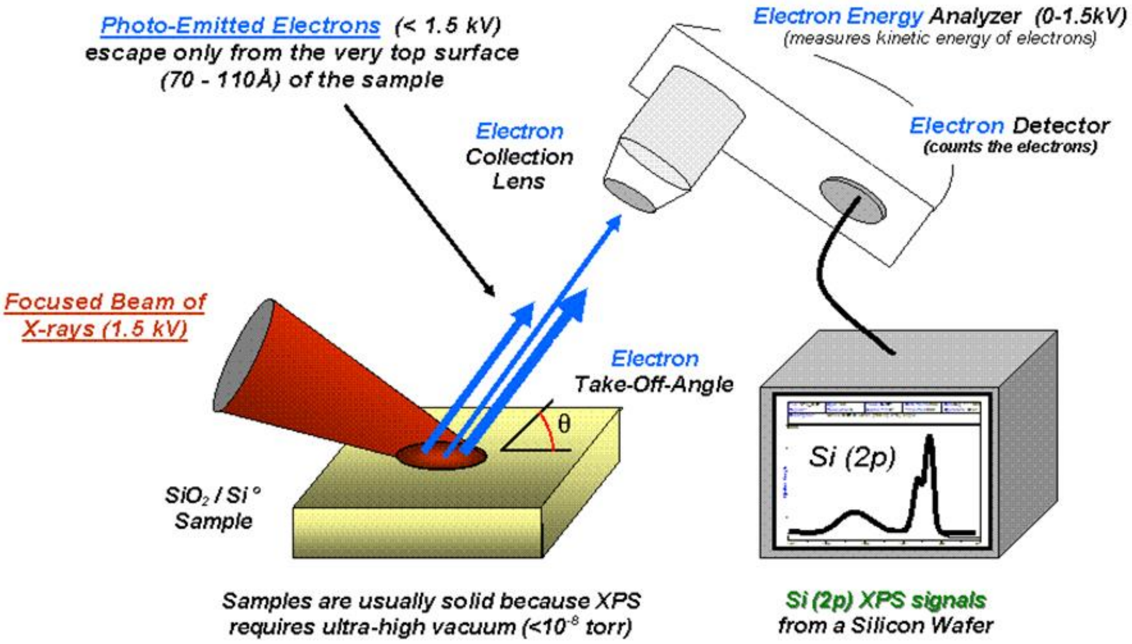

Fig. 3.6. Schematic setup of XPS [3.34].

3.7. Electron Paramagnetic Resonance (EPR) Spectroscopy.

EPR spectroscopy is a prominent technique for examining unpaired electrons (the Zeeman Effect) in a material, as well as the complexity of metal or organic radicals. This technique functions similarly to nuclear magnetic resonance (NMR), explaining the incident of atomic particle resonance as the effect of high-frequency electromagnetic radiation absorption due to external magnetic fields, except that instead of spins of atomic nuclei, electron spins are excited [3.35]. In the absence of an external magnetic field, electron spins are degenerate; quantum numbers $m_s = -1/2$ (which indicates parallel directions) and $m_s = +1/2$ (which indicates antiparallel directions) characterize electron spin degeneracy by the magnetic field. Unpaired electrons can only be aligned in one of two ways (spin-up or spin-down) f the applied field, and these alignments are proportional to the applied magnetic field intensity [3.36, 3.37]. The difference in energy after degeneracy is given by:

$$\Delta E = hf = g\mu_B B_0 \qquad \text{where } \mu_B \text{ is given by} \quad \mu_B = \frac{eh}{2mc} \quad \text{and } V = hf \qquad (3.6)$$

Where ΔE is the energy difference, μ_B is the Bohr magneton, h is Planck's constant, B_0 magnetic field, g_s is the electron spin g-factor, f is the frequency of radiation, e is the electron charge [3.38].

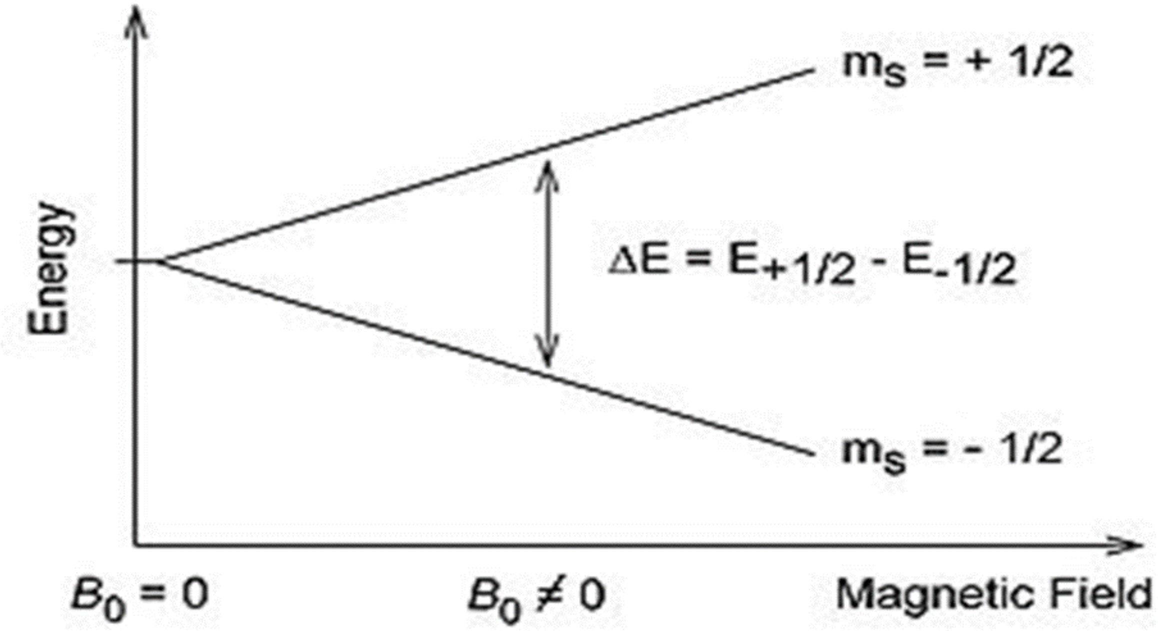

Fig. 3.7. Energy levels for electron spins due to applied magnetic field B [38].

3.8. Ultraviolet-Visible (UV-Vis).

The ultraviolet-visible (UV-Vis) approach is used to evaluate the transmittance and absorbance of a light that passes through a substance in the UV or visible spectrum at a specified wavelength. Not all light goes through or is absorbed by the sample in this procedure. UV-Vis has a wavelength range of 190-820 nm. The concentration of the sample is calculated using absorbance (by using Lambert's law) in equation 3.7, and the corresponding absorbance measured over a wide range of wavelengths may be identified using the absorbance, the absorbance spectrum [3.39-3.43]. The spectrum is created chemically by the absorption of visible or ultraviolet light.

Beer-Lambert law: $A = \log (I_0/I) = \varepsilon lc$ (3.7)

where A is the absorbance, ε is molar absorption constant of the analyte for a certain wavelength, c is the concentration of the analyte ($\text{mol}\cdot\text{l}^{-1}$) and l is the path length, I_0 is incident radiation, and I is the transmitted radiation. The Beer-Beer Law define the relation of Absorbance with concentration of the analyte and the path length, the absorbance is directly proportional to the analyte concentration and the path length.

UV-Vis Spectroscopy is an optical method that detects the change in UV and visible light intensity as a function of wavelength as it interacts with materials. UV-Vis spectroscopy primarily investigates electron transitions. Transitions from n orbitals to anti-bonding π* and σ* orbitals in conjugated organic molecules are typical instances; d-d transitions in transition metal ions; charge transfer transitions in certain organic and transition metal compounds; band gap transitions in semiconductors are further examples. Fig.3.8. the light source is directed to the dispersion device through the entrance slit, the light with different energy disperses into different frequency (colours). The light with different frequencies passes the exit slit and heat the sample to the detector where the light it measures the light absorbed, transmitted or reflected by the sample at each wavelength.

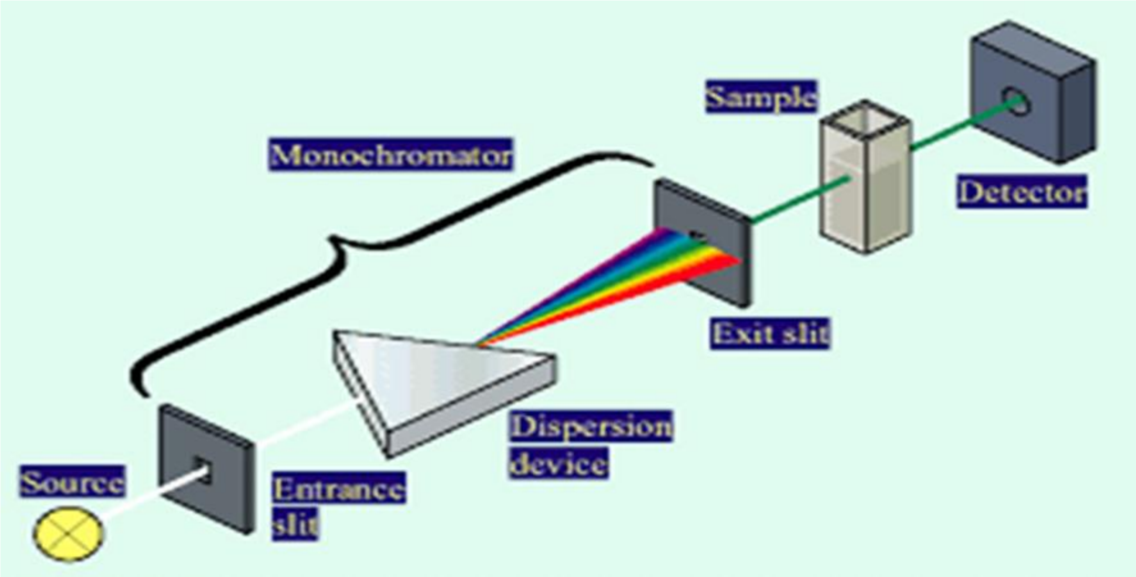

Fig. 3.8. Schematic illustration of UV/Vis spectroscopy [3.44].

3.9. Autoclave Hydrothermal Synthesis Method

In this study, the autoclave hydrothermal method was applied in the chemical synthesis of single crystals at high temperatures and pressures in a sealed and heated container under crucial solvent or mixture conditions. This synthesis process functions at temperatures above the boiling point of water and pressures more than 1 atm [3.45].

This method of synthesis has several advantages, including the ability to produce high-quality crystals at high temperatures, produce nanomaterial with little or no material loss due to high vapor pressure, control nanomaterial structure through a liquid phase or multiphase chemical reactions in the synthesis procedure, low-cost apparatus, and the ability to act as a catalyst to form desired material, as well as disadvantages, such as the inability to monitor crystals. There are two types of hydrothermal synthesis reactors: polytetrafluoroethylene (PTFE) or Teflon lined autoclave reactors and PPL lined autoclave reactors (see Fig. 3.9). The hydrothermal reactor consists of two major components: a high-quality stainless-steel jacket (outer) and a Teflon liner (inner) [3.49].

Fig. 3.9. Stainless steel autoclave with the inner part Teflon liner.

3.10. The material used In the preparation of the nanoparticles.

Sodium hydroxide (NaOH), Tin chloride dehydrate ($SnCl_2.2H_2O$), distilled water, Urea, ammonium hydroxide (NH_4OH), vanadium pentoxide (V_2O_5), and Copper oxide (CuO).

3.10.1. Preparation of Sno_2 nanoparticle.

SnO_2 sphere were prepared using hydrothermal technique. Certain amount of Tin (ii) chloride dehydrates ($SnCl_2.2H_2O$) powder were dissolved in 150ml distilled water, the solution were stirred continuously at 70 ºC using a magnetic rod. Ammonium hydroxide was added dropwise to maintain the pH of the solution, pH of 9.00 was obtained. The solution was then deposited in to 45ml cylindrical Teflon liner then into stainless steel autoclave reactor, heated at 180 ºC for 16 hours using an ECOTHERM oven. The contents were cooled to room temperature, the precipitates were centrifuged using mode TJ-6 centrifuge machine thoroughly with distilled water and dried at 80 ºC for 24 hours to obtain SnO_2. The SnO_2 powder was annealed at 300 ºC for 1 hour.

References

3.1. https://cms.eas.ualberta.ca/xrd/how-xrd-works/.

3.2. https://www.researchgate.net/fig./Braggs-law-A-two-dimensional-crystal-lattice-and-a-set-of-imaginary-planes-is_fig10_47418334.

3.3. N.S.Bajaj. R.A.Joshi. Chapter 3 - Energy materials: synthesis and characterization techniques. 2021. p61-68. 10.1016/B978-0-12-823710-6.00019-4.

3.4. Simin Tazikeh. Amir Akbari. Amin Talebi. Emad Talebi. Synthesis and characterization of tin oxide nanoparticles via the Co-precipitation method. 2014. 99-100.

3.5. Raül Díaz Delgado. Tin Oxide Gas Sensors: An Electrochemical Approach. 2002. 27-41/.

3.6. Vallikkodi Mahalingam. Synthesis, growth and characterization of piperazinium p-Aminobenzoate and Piperazinium p-Chlorobenzoate nonlinear optical single crystals. 2018. p38. 10.13140/RG.2.2.16046.82243.

3.7. Aurangzeb Khan. Synthesis, characterization and luminescence properties of zinc oxide nanostructure. 2006. 31-32.

3.8. Meisam Omidi. Atena Fatehinya. Masomeh Farahani. Zahra Akbari. Saleheh Shahmoradi. Fatemeh Yazdian. Mohammadreza Tahriri. Keyvan Moharamzadeh. Lobat Tayebi. Daryoosh Vashaee. (n.d.) Characterization of biomaterials. 102-103.

3.9. Nidhi Raval. Rahul Maheshwari. Dnyaneshwar Kalyane. Susanne R. Youngren-Ortiz. Mahavir B. Chougule. Rakesh K. Tekade. (n.d.). Importance of Physicochemical Characterization of Nanoparticles in Pharmaceutical Product Development. 375-376.

3.10. Emily Nagle. Scanning electron microscopy (SEM). 2020. (https://chem.libretexts.org/Courses/Franklin_and_Marshall_College/Introduction_to_Materials_Characterization__CHM_412_Collaborative_Text/Electron_and_Probe_Microscopy/Scanning_electron_microscopy_(SEM)).

3.11. Susan Swapp. Scanning Electron Microscopy (SEM). (https://serc.carleton.edu/research_education/geochemsheets/techniques/SEM.html).

3.12. Anders Brostrøm. Kirsten I. Kling. Karin S. Hougaard. Kristian Mølhave. Complex Aerosol Characterization by Scanning Electron Microscopy Coupled with Energy Dispersive X-ray Spectroscopy. 2020. 1.

3.13. Alyamani and O. M. Lemine. FE-SEM Characterization of Some Nanomaterial. 2012.

3.14. David Herres. The difference between scanning electron microscopes and tunneling scanning electron microscopes. 2019. (https://www.testandmeasurementtips.com/the-difference-between-scanning-electron-microscopes-and-tunneling-scanning-electron-microscopes-faq/)

3.15. Antonis Nanakoudis. What is SEM? Scanning Electron Microscopy Explained. 2019.(https://www.thermofisher.com/blog/microscopy/what-is-sem-scanning-electron-microscopy-explained/).

3.16. P. Senthil Kumar. K. Grace Pavithra. Mu. Naushad.(n.d.) Characterization techniques for nanomaterials. 109.

3.17. Thara Seesaard. Teerakiat Kerdcharoen. Chatchawal Wongchoosuk. (n.d). Hybrid materials with carbon nanotubes for gas sensing. 204.

3.18. S. Schweiger. J.L.M. Rupp. (n.d.). Strain and interfaces for metal oxide-based memristive devices. 312. Ganjali Mansoureh. Vahdatkhah Parisa. (n.d.). Synthesis of metal nanoparticles using laser ablation technique. 586.

3.19. David C. Joy. (n.d.). Transmission electron microscope. (https://www.britannica.com/technology/transmission-electron-microscope).

3.20. Bioscience. Transmission Electron Microscope (TEM). 2018. (http://www.biosciencenotes.com/transmission-electron-microscope-tem/).

3.21. Cheadle Centre for Biodiversity and Ecological Restoration. (n.d.). The Transmission Electron Microscope. (https://www.ccber.ucsb.edu/ucsb-natural-history-collections-botanical-plant-anatomy/transmission-electron-microscope).

3.22. Chris Woodford. Electron microscopes. 2020. (https://www.explainthatstuff.com/electronmicroscopes.html).

3.23. Mahmoud Nasrollahzadeh, Monireh Atarod. Mohaddeseh Sajjadi,S. Mohammad Sajadi. Zahra Issaabadi. (.N.d.). Plant-Mediated Green Synthesis of Nanostructures: Mechanisms, Characterization, and Applications. 2019. 258-263.

3.24. Pavan M. V. Raja. Andrew R. Barron. BET Surface Area Analysis of Nanoparticles. 2020.

3.25. Majid Naderi. Chapter Fourteen - Surface Area: Brunauer–Emmett–Teller (BET). 2015. 591.

3.26. *R.R. Mather.* Surface modification of textiles by plasma treatments. 2009. 302.

3.27. *Roger W. Welker.* Size Analysis and Identification of Particles. 2012. 211.

3.28. *Owen J. Guy. Kelly-Ann D. Walker*. Graphene Functionalization for Biosensor Applications. 2016. 98-99.

3.29. *D.R. Baer.S. Thevuthasan.* Characterization of Thin Films and Coatings. 2010. 755.

3.30. Bin Hu. Man He. Beibei Chen. Magnetic nanoparticle sorbents. 2020. 246.

3.31. Efrat Korin. Natalya Froumin. Smadar Cohen. Surface Analysis of Nanocomplexes by X-ray Photoelectron Spectroscopy (XPS). 2017. 882.

3.32. Steffen Oswald. X-ray Photoelectron Spectroscopy in Analysis of Surfaces. 2013. 2.

3.33. G. Greczynski. L. Hultman. X-ray photoelectron spectroscopy: Towards reliable binding energy referencing. 2019. 3.

3.34. https://en.wikipedia.org/wiki/X-ray_photoelectron_spectroscopy.

3.35. https://en.wikipedia.org/wiki/Electron_paramagnetic_resonance.

3.36. K.C.Khulbe. A.F.Ismail. T.Matsuur. Chapter 3 - Electron Paramagnetic Resonance (EPR) Spectroscopy. 2017. 48.

3.37. Ahmed M. Maghraby. Introductory Chapter: Electron Paramagnetic Resonance. 2019. 1-2.

3.38. https://phys.libretexts.org/Courses/University_of_California_Davis/UCD%3A_Biophysics_200A_Current_Techniques_in_Biophysics/Electron_Paramagnetic_Resonance.

3.39. Bahrudeen S. Hameed. Chandra S. Bhatt. Bharathkumar Nagaraj. Anil . K. Suresh. Chromatography as an Efficient Technique for the Separation of Diversified Nanoparticles. 2018. 513.

3.40. Cintil Jose Chirayil. Jiji Abraham. Raghvendra Kumar Mishra. Soney C.George. Sabu Thomas. Instrumental Techniques for the Characterization of Nanoparticles. 2017. 19-20.

3.41. P. Senthil Kumar. K. Grace Pavithra. Mu.Naushad. Characterization techniques for nanomaterials Characterization techniques for nanomaterials. 2019. 113.

3.42. Fellipy S. Rocha. Anderson J. Gomes. Claure N. Lunardi. Serge Kaliaguine. Gregory S. Patience. Experimental Methods in Chemical Engineering: Ultraviolet Visible Spectroscopy|UV-Vis. 2018. 1-3.

3.43. http://www.chromedia.org/chromedia?subNav=lnijabEsHiemBpdmBlIEcCAtBN&waxtrapp=fotjtbEsHiemBpdmBlIEcCAtB

3.44. https://www.ssi.shimadzu.com/products/uv-vis spectrophotometers/faqs/instrument-design.html

3.45. *S.-H. Feng, G.-H. Li.* Hydrothermal and Solvothermal Syntheses.2017. 73-75.

3.46. https://eng.thesaurus.rusnano.com/wiki/article729.

3.47. Yong X. Gan. Ahalapitiya H. Jayatissa. Zhen Yu. Xi Chen. Mingheng Li. Hydrothermal Synthesis of Nanomaterials. 2020. 1.

3.48. Muhammad Luqman Bin Mohd Napi. Fabrication And Characterization of Nanostructured Fluorine Doped Tin Oxide Thin Film for Dssc by Hydrothermal Method. 2017. 15-16.

3.49. https://www.techinstro.com/hydrothermal-autoclave-reactor/

CHAPTER 4

Low Temperature Tunability on CO Selectivity, Low Detection Limit Based on SnO_2-Hollowspheres Induced by Various Bases*

4.1. Introduction

The daily population activities linked to the emission of various hazardous gases that can be toxic, explosive, and flammable such as CO, H_2S, SO_2, NO_x, CH_4, CO_2 and volatile organic compounds have a negative impact on human lives and the environment [4.1-4.4]. Owed to its nature, carbon monoxide (CO) may not be openly detected by human nose unless at higher and lethal concentration. CO harming may result to instant deaths due to suffocation. This extremely poisonous gas kills numerous people yearly because of building and shack fires and the use of gas heaters in homes [4.5]. Therefore, fabrication of portable CO gas sensors is very vital for prompt detection of this deadly gas. Various semiconductor metal oxides (SMOs) (e.g., SnO_2, CuO, TiO_2, V_2O_5 and WO_3) have been used as gas sensors for detection of CO [4.6-4.9]. Amongst these SMOs, SnO_2 remained the most used material in the gas sensing field, due to its unique properties, such as bandgap of 3.6 eV, superior stability, accessibility, low-cost and can be easily synthesized in various forms. Additionally, it possesses superior electron mobility (160 $cm^2 \cdot V/s$) [4.10-4.12].

Nonetheless, SnO_2 has been suffering poor sensitivity as well as selectivity when exposed to a target gas. In addition it also operates well at higher sensing temperature, which result to higher power consumption. Several studies have attempted to improve

---

* The contents of this work were published in Surfaces and Interfaces 31 (2022) 101954.

the gas sensing performance of SnO_2 through altering its properties, by either doping, or incorporating other metal oxides to form heterostructure. For instance, Mauraya et al [4.13] has reported the CO sensing characteristics of SnO_2 prepared using vacuum evaporation. They reported a response of 70.7% towards 915 ppm CO gas at a functional temperature of 400 °C. Kim et al. [4.14] prepared Au-SnO_2-co-decorated WS_2 nanosheet based sensor and tested towards CO gas. They reported a response of roughly 3.7 towards 50 ppm CO with a tuned applied voltage of 4.7 V. Viet et al. [4.15] reported a CO response of roughly 1.5 at 150 °C. The CuO-SnO_2 nanocomposites-based sensor prepared using co-precipitation method showed a response of 3.52% towards 100 ppm CO gas at 200 °C. Kim et al. [4.16] reported a low operating temperature gas sensing for the detection of CO gas utilizing the 2D MoS_2 gas sensor.

In contrast to SnO_2, vanadium pentoxide (V_2O_5), is a unique n-type material composed of a layered structure, having properties, such as good chemical and thermal stability, wide optical band gap, good thermoelectric property, which makes it applicable in gas sensing applications. Though, it is vital to point out that limited work has been done on CO gas sensing using a V_2O_5 based sensor. For instance, Yeh et al. [4.17] prepared CuO/V_2O_5 hybrid nanowires using a facile chemical route. They reported a response of 1.5 towards 50 ppm CO at 300 °C. Moreover, Abkenar et al. [4.18] reported on CO sensing using Au-V_2O_5 nanosensor, which showed a response of 58 400 °C. Based on the points mentioned above, it is clear that limited studies exist on the low operating temperature sensing, using bare SnO_2 and V_2O_5 nanostructures.

Thus, in the current work, we report on the low temperature tunability on the CO selectivity derived from pure SnO_2-Hollowspheres prepared using a NaOH base. The results showed the effect of base in achieving different morphologies and surface defects which later contribute to the sensing performance. The presence of O_v was confirmed using both in-situ photoluminescence (PL) analyses and electron paramagnetic resonance (EPR).

4.2. Experimental method

4.2.1. Materials

Tin chloride dehydrate ($SnCl_2.2H_2O$) and vanadium pentoxide (V_2O_5), sodium hydroxide (NaOH, purity 99%), ammonium (NH_4OH) (30-33% NH_3 in water, 99.99%), and Urea (purity 99%), were purchased from Sigma-Aldrich and were used without further purification.

4.2.2. Synthesis of nanoparticles.

The influence of base on the morphology of pure SnO_2 and V_2O_5 nanostructures was investigated using NaOH, NH_4OH and Urea at the reaction temperature of 180 °C. As a result, the certain amount of $SnCl_2.2H_2O$, and V_2O_5 powder were added in separate beakers with 150 ml of distilled water, the solutions were stirred for one hour using magnetic stirring at 70 ºC. To maintain the pH, NaOH, NH_4OH and Urea were added drop wise until the pH of 9.00 of each solution was recorded/reached using a pH meter. The solutions were then transferred into a Teflon lined stainless steel autoclave (purchased from Labotec (pty) LTD) and were heated for 16 hours in an oven at 180 ºC. The products were washed and centrifuged discarding the solvent ten times using a time interval of ten minutes in a mode-TJ-6 centrifuge machine. The final powders were dried at 80 ºC for 24 hours in the oven, before annealed at 450 ˚C and grinded using mortar and pistil. Then SnO_2, and V_2O_5 powders were produced and recorded as SnO_2-NaOH, SnO_2-NH_4OH and SnO_2-Urea, and V_2O_5-NaOH, V_2O_5-NH_4OH and V_2O_5-Urea.

4.2.3. Characterization techniques

The structure of the materials was probed using a PANalytical X'-pert PRO-PW 3040/60 X-ray diffractometer (XRD) furnished with a source radiation of CuKα (λ= 0.154 nm). The scanning electron microscopy (SEM, ZEISS Auriga)) equipped with an energy dispersive X-ray spectroscopy (EDS) facility was utilized to examine the surface morphology and elemental composition of the materials. The surface defects and paramagnetic features were probed using a completely powered imaging spectrometer with a Kimmon IK series 325 nm laser photoluminescence spectroscopy and FSA JEOL electron paramagnetic resonance (EPR), respectively.

4.2.4. Gas Sensing Characteristics

Various SnO_2 and V_2O_5 sensing devices were developed by pasting the unvaryingly slurry onto the alumina substrates (size: 2 mm × 0.5 mm) with two Pt electrodes. The fabricated films were dried at 200 ºC in an oven for an hour to maintain a proper adhesion. A commercial KSGAS6S KENOSISTEC gas testing station (acquired from Italy) was utilized to study the change in the sensor resistance. The atmospheric conditions were controlled using MKS Instruments Deutschland GmbH mass flow controllers, which provided 5 - 100 ppm concentrations of carbon monoxide (CO), methanol, ethanol, hydrogen sulphide (H_2S), methane (CH_4) and nitrogen dioxide (NO_2) into a sealed testing chamber containing a volume of 1 litre by diluting the analyte gases in synthetic air. The output signal was extracted by applying a constant bias of 0.5 V to the sensing materials. The analyses were accomplished at different operational temperatures of 25, 75 and 150 ºC. The change in sensor resistance was monitored by a Keithley 6487 picoammeter/voltage source meter. Relative humidity (RH) measurements were regulated at 40 % using a water bath humidity generation chamber. The sensor response was computed by the change of the resistance utilizing the following formulas: R_a/R_g and R_g/R_a (R_a: resistance in dry air, R_g: resistance in gas) for reducing and oxidizing gases, respectively.

4.3. Results and discussions

4.3.1. Surface morphology and Structural Characteristics

The effect of various bases, such as NaOH, NH_4OH and Urea on the preparation of pure material SnO_2 is discussed in this section. Fig. 4.1 (a) and (b) show low magnification and high magnification images of SnO_2-NaOH. A porous cluster with a chirped/etched like surface is shown in Fig. 4.1 (a). More additionally, high magnification images in Fig. 4.1 (b) revealed hollow-spheres distributed on the surface. Fig. 4.1 (c) and (d) shows the low magnification and high magnification images of the SnO_2-NH_4OH. The low magnification displays block like structures, which appear to be covered and surrounded by nanoparticles on the surface. The high magnification images, however, displays nanoflakes-like structures. The low magnification images of SnO_2-Urea exhibit spheres in Fig. 4.1(e) while the high magnification indeed shows hierarchically arranged nanoflakes forming a spherical shape which has a diameter range of 0.3-1μm. The study indicates that different bases have the effect in the structural morphology of the material. The EDS mapping showed that the materials consisted of Sn and O only (see supporting information, Fig. S1). The carbon peak was due to the carbon tape used during the sample preparation.

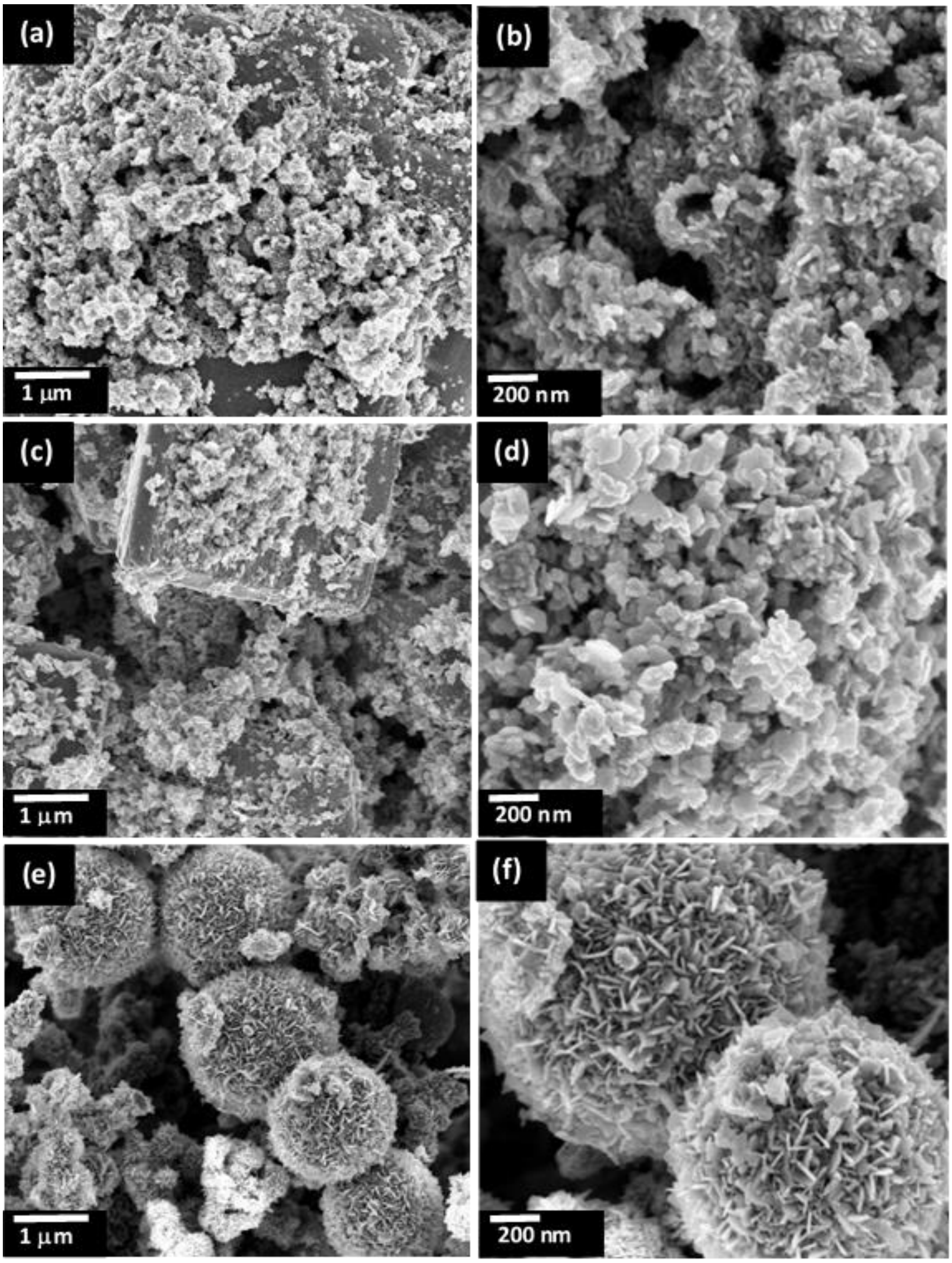

Fig. 4.1: SEM images of low and high magnification of (a-b) SnO_2-NaOH, (c-d) SnO_2-NH_4OH and (e-f) SnO_2-Urea.

The influence of different bases on the morphology of the V_2O_5 nanostructure was also investigated as shown in Fig. 4.2. The low- and high- magnification images in Fig. 4.2 (a) and (b) show V_2O_5 –NaOH nanorods like structure, which are attached to one another and well aligned. The rods have a diameter range of 100 – 150 nm and length that is more than 5 µm. The low and high magnification of V_2O_5-NH_4OH in Fig. 4.2 (c) and (d) displayed shorter rods, which appeared to have been broken. Upon using the Urea as a base (see Fig. 4.2 (e) and (f)), the low magnification indeed confirms that thicker rod (diameter range ~10 µm) like structure are favoured, which are hexagonal in shape. The length of this hexagonally shaped V_2O_5-Urea is also in the range of > 30 µm.

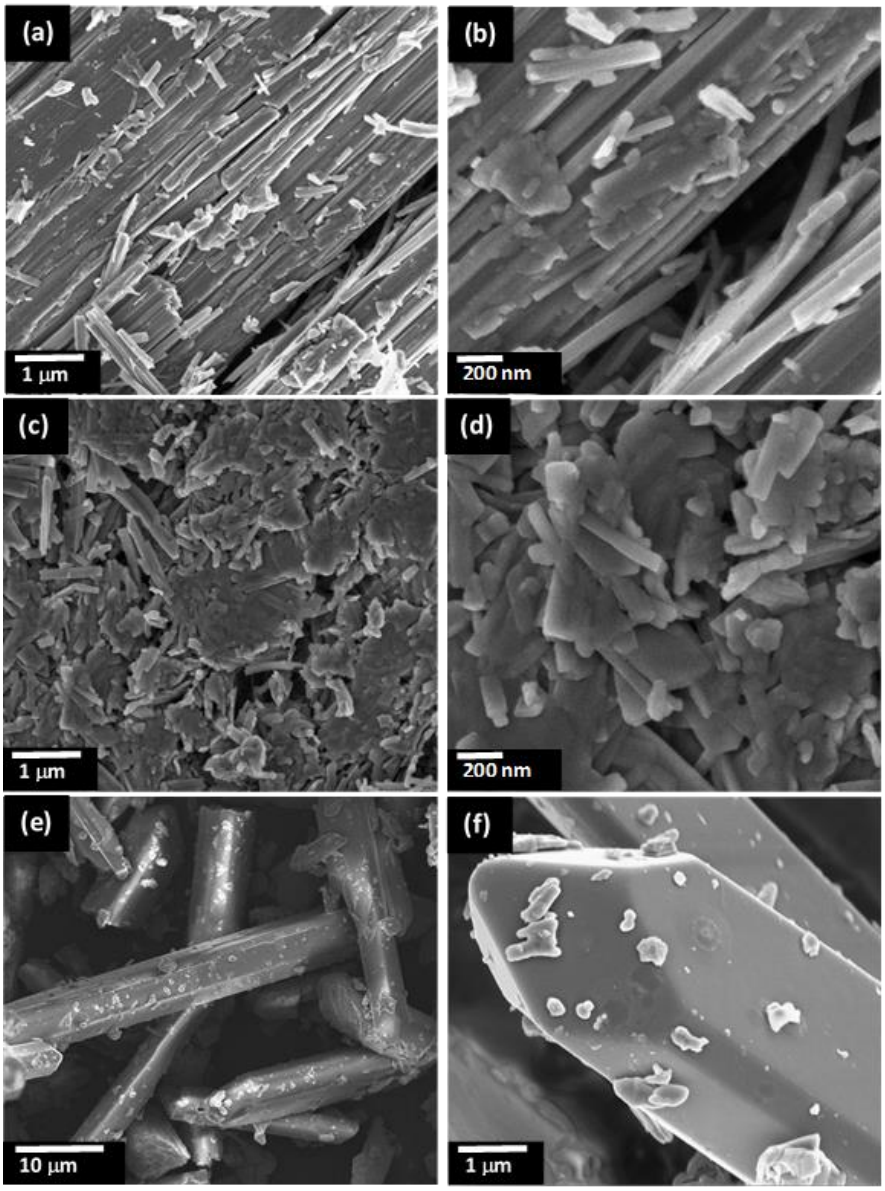

Fig. 4.2: SEM images of low and high magnification of (a-b) V_2O_5-NaOH, (c-d) V_2O_5-NH_4OH and (e-f) V_2O_5-Urea.

Fig. 4.3 illustrates the XRD patterns of the various SnO_2 and V_2O_5 prepared using three different bases, which included NaOH, Urea and NH_4OH. The diffraction patterns in Fig. 3 (a) show peaks at 2θ= 20º, 34º, 38º, 52º, 54º and 63º corresponding to (110), (101), (200), (211), (220) and (310), respectively. An additional peak positioned at 30º, is observed on all the samples and indicating poor crystallization of $Sn_6O_4(OH)_4$ as hydroxide intermediate are still present post annealing (confirmed by ICDD 46-1486) [4.19]. As noted, the SnO_2-NH_4OH nanostructure presents improved crystallinity in comparison to SnO_2-NaOH, and SnO_2-Urea as indicated by sharper peaks. Furthermore, a shift to higher angles due to increased strain was also observed in this order: SnO_2-NaOH> SnO_2-Urea > SnO_2-NH_4OH, as observed in magnified patterns of (101) peaks (see Fig. 4.3(b)). This is further justified by the calculated crystallite sizes of 8.6 nm, 8.8 nm and 16.9 nm for the SnO_2-NaOH, SnO_2-Urea, SnO_2-NH_4OH, respectively. The crystallite sizes were calculated using the Scherrer formula. Fig. 3 (c) displays the XRD patterns of the V_2O_5 nanostructures prepared using various bases. As presented, the sample prepared using NaOH base indeed shows an orthorhombic V_2O_5 structure (confirmed by the ICDD 41-1426), showing peaks at 20.2. 26.1, 30.91, 41.1, and 51.1° correspond to (001), 110, (301), (002) and (020) respectively. Nonetheless, the samples prepared using NH_4OH and Urea display several phases, which may include the V_2O_3 and V_4O_7. Moreover, we carried out the EDS, which indeed showed the materials do not contain any impurities.

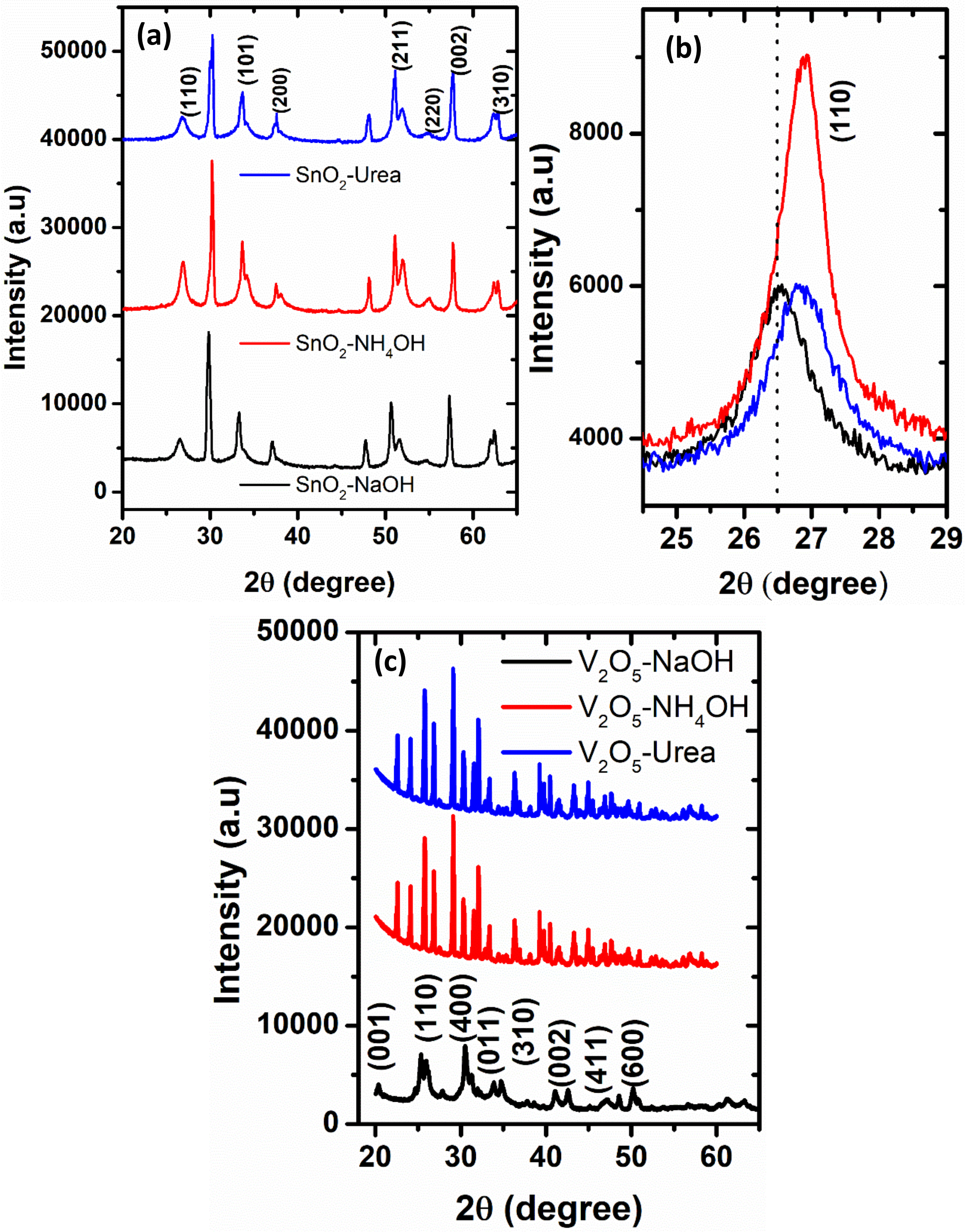

Fig. 4.3: XRD patterns of (a) SnO_2- NaOH, SnO_2-NH_4OH, SnO_2-Urea and (b) V_2O_5-NaOH, V_2O_5-Urea and V_2O_5-NH_4OH.

4.3.2. Electrical and Gas Sensing Characteristics.

The electrical characteristics of SnO_2 and V_2O_5 based sensors were examined toward both reducing and oxidizing gases at various operating temperatures. Fig. 4 (a) and

(b) illustrates the variation of the resistance in air (R_a) as a function of operational temperature. As noted from the Fig., the R_a decreases with the increase operational temperature, displaying the distinctive intrinsic behaviour of a semiconductor metal oxide-based sensors. All the sensors follow the same trends of R_a changes with operational temperature. Both SnO_2 and V_2O_5 based sensors prepared from NH_4OH base displayed higher R_a compared to other bases. This increased electrical resistance could be associated with improved crystallinity [4.20].

To understand the role of operational temperature on the gas sensing performance of various sensors towards different gases, the sensors were tested at 25, 75 and

150 ºC, as shown in Fig. 4.4. According to Safety, Health and Welfare at Work (Chemical Agents) Regulations, 2001, the maximum occupational exposure limit value (OELV) concentration of a CO at work for 8 hours is 20 ppm [4.21], while for Occupational Safety and Health Administration Permissible Exposure Limits (OSHA PEL) for CO is 50-60 ppm for 8hr shift [4.22]. Furthermore, the American Conference of Governmental Industrial Hygienists (ACGIH) has recommended a CO a threshold limit value (TLV) of 25 ppm [4.22]. Consequently, in the current work we showed the response versus temperature towards 20 and 60 ppm CO. Remarkably, while the sensors were able to detect either 20 or 60 ppm CO at room temperature, nonetheless, the sensors showed a good response at low operating of 75 ºC. At higher temperature of 150 ºC, the sensor response reduced, signifying that the 75 ºC is the optimum temperature. Such low operating temperature demonstrates that the sensors indeed reveal a characteristics of low power consumption. Among the sensors, the SnO_2-NaOH based sensor revealed a superior response of roughly 16 at 20 ppm, more interestingly the response doubled (i.e., $R_a/R_g \approx 32$) as the concentration increased to

60 ppm. Kim et al. [4.14] reported a response of 3.687 within the CO concentration of interest~ 50 ppm, however, this was achieved under an optimized applied voltage of 4.7 V using the Au-SnO_2-co-decorated WS_2 nanosheet gas sensor. A higher CO response of roughly 52% was observed by Mauraya et al. [4.23] at an operating temperature of 400 ºC using PdO/SnO_2 structure prepared by a direct oxidation of Pd metal on SnO_2 films. According to the authors, such multi-fold improvement of CO response was related to (i) improved surface area induced by PdO loading that delivered additional free surface sites for the adsorption of oxygen, (ii) increase of oxygen molecules catalytic dissociation and (iii) modulation of the electron depletion region at PdO/SnO_2 p-n heterostructure because of ionic oxygen adsorption/desorption. Furthermore, Zhou et al. [4.26] reported a CO response of 23.18 at an enhanced temperature of 250 ºC at 100 ppm. They associated such improved CO response to rapid rate of diffusion, easy adsorption of polar CO molecules, and lower activation energy of CO to CO_2 conversion in comparison to other gaseous molecules [4.27].

To display the real reason behind the higher response observed at 75 ºC, the real-time response ability of SnO_2-NaOH based sensor to various CO concentrations, the response/recovery properties of the sensor towards 5- 100 ppm CO at 75 and 150 ºC were investigated, as depicted in Fig. 4.4 (e) and (f). As noted, the sensors displayed a noticeable electrical signal changes at various CO concentrations. The sensors presented a response when the gas was injected in the chamber and recovered almost completely when the gas was removed. The rapid decrease in resistances upon exposure to CO gas in all operating temperatures confirmed that the sensors have the n-type semiconducting properties.

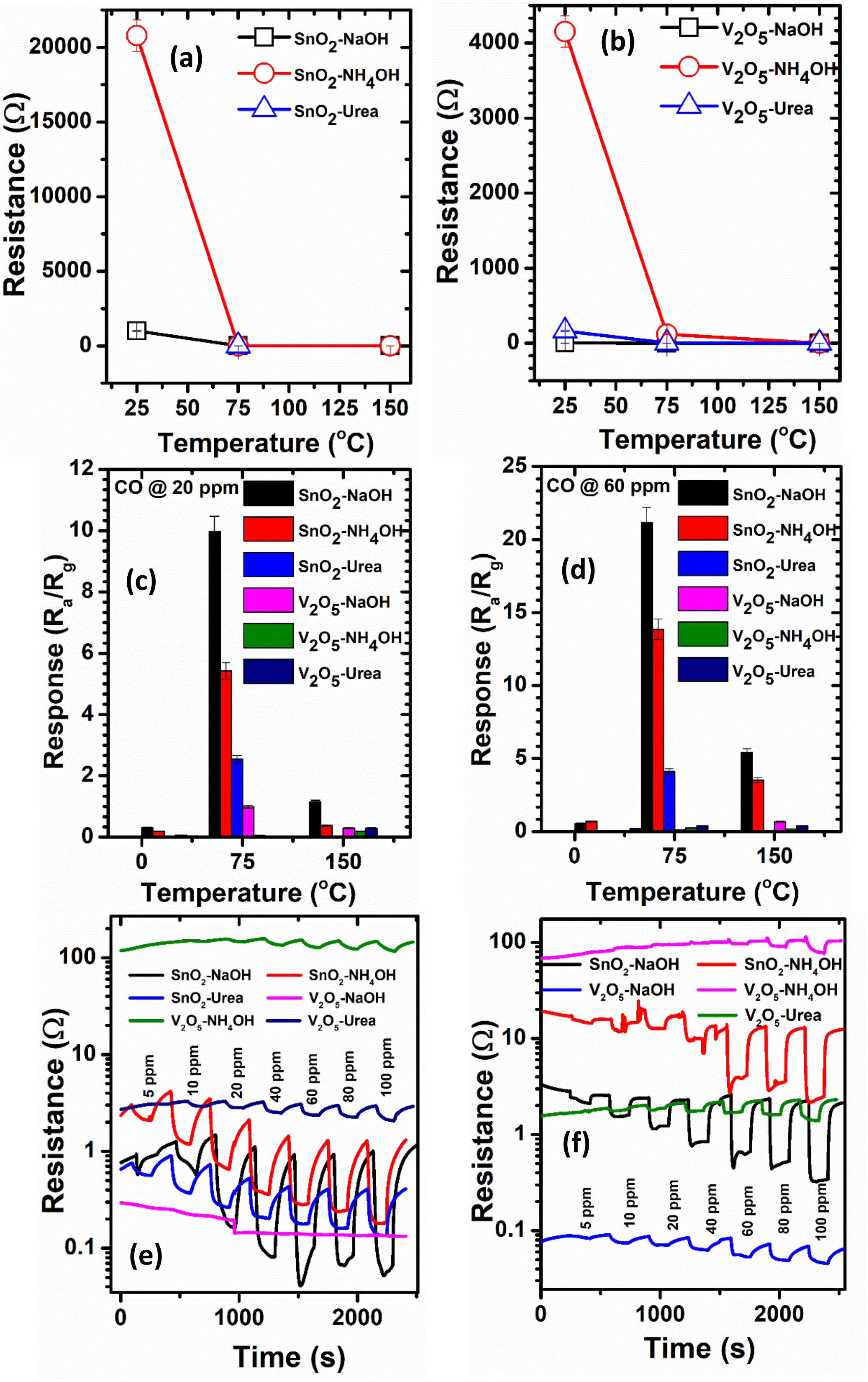

Fig. 4.4. (a-b) Resistance in air (R_a) versus operating temperature, (c and d) response versus operating temperature and (e and f) real-time resistance at 75 and 150 °C.

Fig. 4.5 shows the response versus gas CO concentration for various gas sensors at operating temperature of 75 ºC. The sensing response of the SnO_2 derived from NaOH base showed improved response in comparison to other sensors at 75 ºC thereafter at higher temperature the response reduced (see Fig. A2). Such decrease is described as the adsorption saturation, when the operational temperature increased the target gas was desorbed before interaction with oxygen ions on the SnO_2 surface, consequently reducing the response [4.26].

As demonstrated in Fig. 4.5 (a), a linear increase in response is observed from 5-60 ppm CO exposure to SnO_2-NaOH, SnO_2-Urea and SnO_2-NH_4OH. As previously noted, a concentration of 20-50 ppm is recommended as a OELV or TVL for 8hr work-shift. This denotes that the current sensor could be very useful for detection of CO at workplace or households. As presented in Fig. 5 (c), the sensors responses were fitted with a linear fit, demonstrating a pronounced potential in practical applications. SnO_2-NaOH demonstrated higher sensitivity of 0.30 ppm^{-1} in comparison to other sensors, SnO_2-NH_4OH (i.e., 0.21 ppm^{-1}), SnO_2-Urea (0.05 ppm^{-1}), V_2O_5-NaOH (0.0008 ppm^{-1}), V_2O_5-NH_4OH (0.0033 ppm^{-1}) and V_2O_5- Urea (0.005 ppm^{-1}). The correlation coefficients R^2 of approximately 0.97–1, validated that the sensors are consistent and can be considered as promising for quantitative detection of CO gas. Besides, based on the standard that is defined by IUPAC (signal-to-noise ratio of 3), the theoretical limit of detection of various sensors towards CO gas was calculated as depicted in Fig. 4.5 (c). As noted, the SnO_2-NaOH based sensor displayed the lowest Limit of Detection (LoD) compared to its counter, thus this further confirm the significant role of oxygen vacancy in enhancing the sensing abilities. This minimal LoD is lesser than 5 ppm that could not be practically tested because of the sensor measurement system limits. This smaller LoD could be used to detect CO gas at the lowest ppb concentration. This establishes that the current sensors offer an effective key for the CO detection at ppb-level for indoor air quality monitoring.

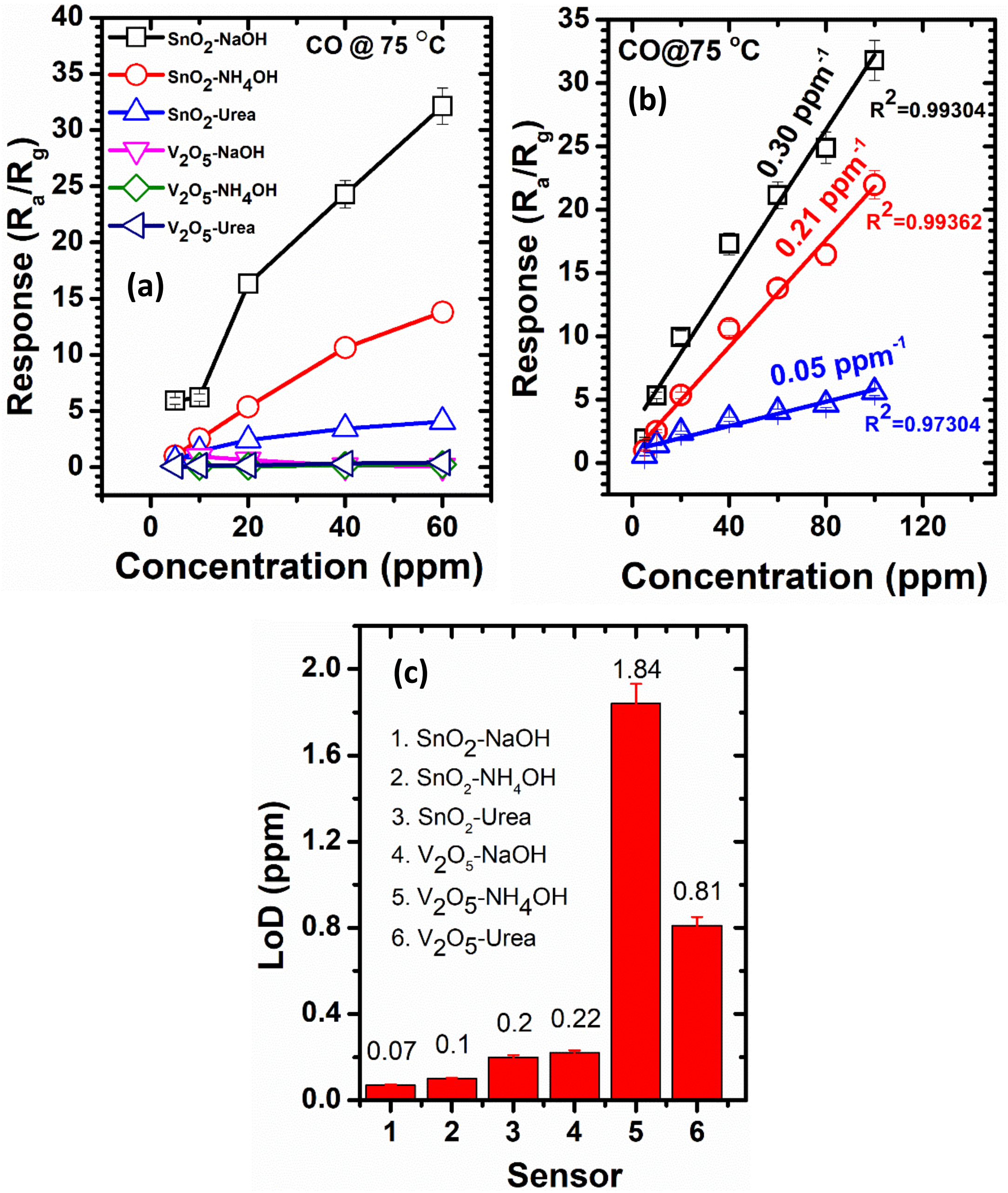

Fig. 4.5: Response versus CO concentration for various sensors tested at 75 ºC, (b) sensitivity plot of various SnO_2 based sensors and (c) LoD of various sensors towards CO at 75 °C.

To further meet the requirements for real life sensor application, rapid response (T_{res}) and recovery (T_{rec}) times are vital parameters in real application. Generally, the T_{res} and T_{rec} are times required for the resistance of the sensor to fluctuate from R_a to 90% of the total resistance change (R_g) in the instance of adsorption and desorption, respectively. Fig. A3 displays the T_{res} and T_{rec} of all the sensors towards 60 ppm CO gas. As demonstrated, the SnO_2-NaOH displayed a remarkable T_{res} and T_{rec} in comparison to its counterparts at 75 °C. Such low response and recovery percentage maybe because of the increased oxygen vacancies (V_O), resulting to increase conductivity of the sensor, further confirming a rapid charge transfer swiftness during the sensing process. Generally, in SMO-based gas sensor, an absolute response-recovery sequence comprises the adsorption-desorption of the CO gas on the surface of sensing layer and the charge-transfer process.

Selectivity is also vital parameter in gas sensing, more especially for real application. Thus, Fig. 4.6 demonstrates the selectivity radar plot of six sensors tested towards CO in the presence of other interference target gases, including ethanol, methanol, CH_4, H_2S and NO_2 at optimized temperature of 75 ºC. As presented in Fig. 4.6, the sensors displayed a superior selectivity towards CO gas. The detection of the sensors towards the target gases, are as follows CO>H_2S>ethanol>methanol>NO_2>CH_4. Compared with the other sensors, the SnO_2-NaOH displayed superior selectivity towards 60 ppm CO at 75 ºC. Such selectivity could be justified by lower bonding energy of CO (358 kJ/mol) associated to its equivalents, such as CH_4 (431 kJ/mol), H_2S (432 kJ/mol), NO_2 (473 kJ/mol), ethanol (458 kJ/mol) and methanol (427 kJ/mol) [4.27, 4.28]. Because of the comparatively less bond energy of CO, the elevated reaction activity of CO molecules contributed to the enhanced selectivity, mainly at the low operative temperature [4.29]. The CO detection can also be justified by rapid rate of diffusion, easy adsorption of polar CO molecules, and lesser activation energy of CO to CO_2 conversion in comparison to other gases [4.30]. Previous studies on pristine SnO_2 based sensor have displayed very inferior CO selectivity [4.31, 4.32]. Thus, the current selectivity clearly shows that our sensor could be used for detection of CO at low temperature.

Moreover, the cross-selectivity of the various sensors towards CO and the other interfering gases, H_2S (S_{CO}/S_{H2S}), ethanol $(S_{CO}/S_{Ethanol})$, NO_2 $\left(S_{CO}/S_{NO_2}\right)$, methanol $(S_{CO}/methanol)$, and CH_4 $\left(S_{CO}/S_{CH_4}\right)$ was examined in Fig. 4.6 (b). This relatively higher response ratio of $\left(S_{CO}/S_{NO_2}\right)$ suggests that the NO_2 did not interfere much with the CO gas, in comparison to H_2S which showed very low response ratio indicating higher interference of H_2S.

Response versus CO concentration, Fig 4.6 (d) – (e) repeatability at 20 and 40 ppm CO in the presence of 40 %RH. Real-time resistance plot of showing a long-term stability of a fresh sensor and that tested after three months and Fig 4.6 (f) – (g) response versus CO concentration of a fresh sensor and that tested after three months. In addition to the selectivity, the long-term stability is also another vital parameter for real application. As a result, we have studied the long-term stability of the SnO_2-NaOH based sensor. Fig. 4.6 (b) displays the real-time resistance plot of the fresh sensors and that tested after three months in dry air. The real-time resistance plot still shows a clear response after three months, though it drifts compared to the fresh sensors. The response plot clearly shows that after three months the sensors were stable at lower concentrations (5-10 ppm), only drifted by at 18, 22 and 40 % at 20, 40 and 60 ppm, respectively.

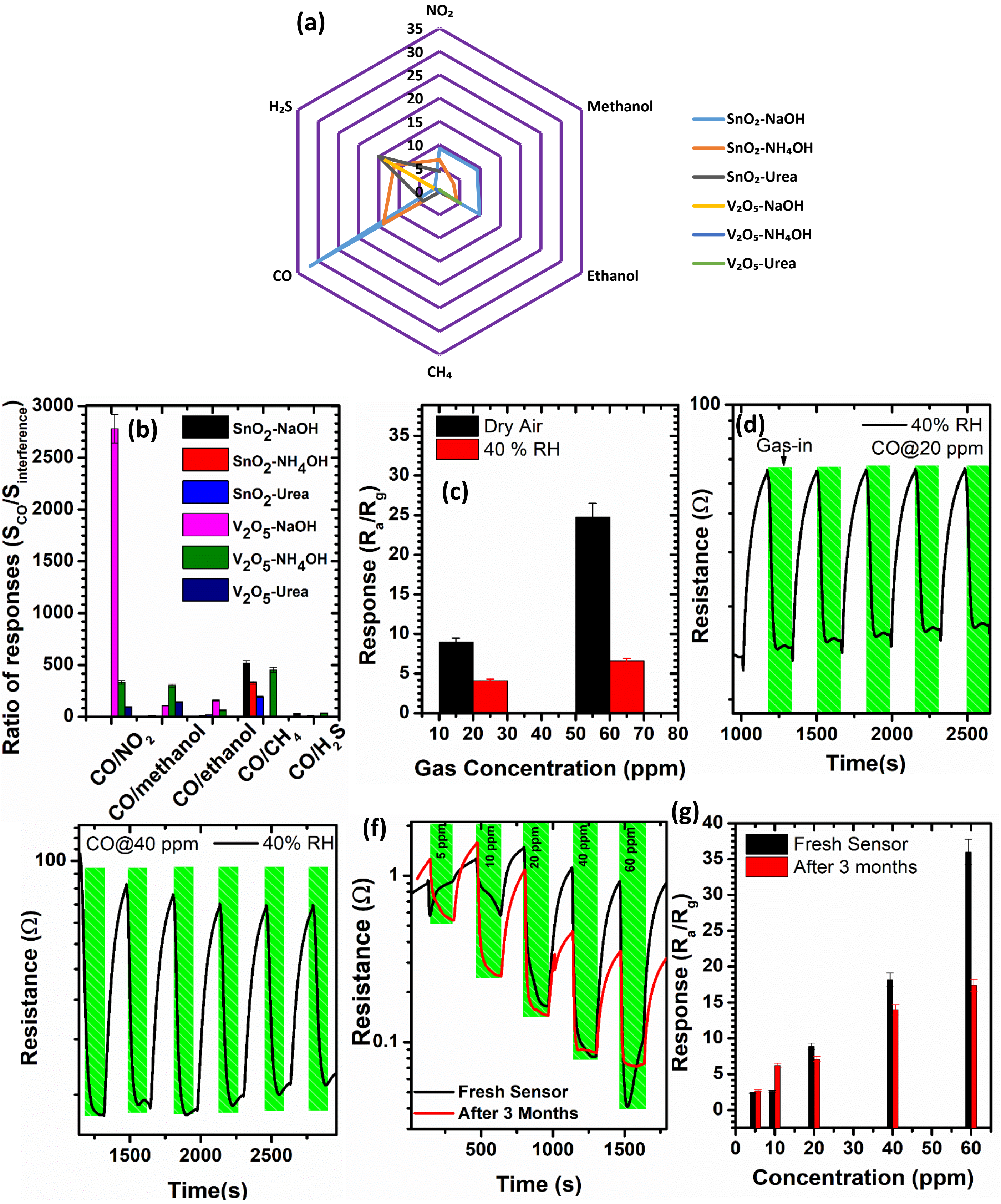

Fig. 4.6: Selectivity radar plot of six sensors tested towards CO, including ethanol, methanol, CH_4, H_2S and NO_2 at optimized temperature of 75 ºC, (b) The cross-

selectivity of various sensors towards CO, (c) Response versus CO concentration in the presence of 40% RH, (d-e) repeatability at 20 and 40 ppm CO in the presence of 40 %RH. (f) Real-time resistance plot of showing a long-term stability of a fresh sensor and that tested after three months and (g) response versus CO concentration of a fresh sensor and that tested after three months.

Table 4.1 associates the CO sensing performances of our fabricated SnO_2-NaOH based sensor with the various sensors reported in the literature. Most of the sensors are incorporated with noble metals, which makes sensing fabrication to be very expensive. For instance, Kim et al. [4.14] used Au-SnO_2-co-decorated WS_2 nanosheet based sensor for detection of CO gas at room temperature, showing a response of 3.2. Though an expensive noble metal, such as Pd was loaded on SnO_2 by Mauraya et al. [4.23], nonetheless the sensor still revealed smaller response at elevated temperature of 400 ºC. In addition, the review article by Majan et al. [4.33] indicated that the SnO_2 is indeed a workhorse for CO sensing compared to other materials. They have also indicated that to reduce the operating temperature of SnO_2 based sensor, doping with additive, like Pd and Pt or incorporation of other SMO or other materials was considered as a best approach. However, such additives, Pt or Pd are very expensive, which increase the costs of the sensor. Thus, based on Table 1 and the ref. [4.33], our current sensor (i.e., SnO_2-NaOH) indeed showed better sensing capabilities in terms of low operating temperature, lower detection limit. While in terms of an economical point of view, our sensor still demonstrated the lowest fabrication costs.

Table 4.1: Summary of the CO gas sensing performances of different gas sensor materials.

Materials	Method	CO (ppm)	Temp. (ºC)	Response	T_{res} (s)	T_{rec} (s)	Refs.
SnO_2-NaOH	**Hydrothermal**	**60**	**75**	**22**	**23**	**96**	**This work**
SnO_2	Vacuum evaporation	915	400	77.7%	21	74	13
Au-SnO_2-co-decorated WS_2 nanosheet	Precipitation	50	RT	3.687			[4.14]
MoS_2 nanosheets-decorated SnO_2 nanofibers	On-chip electrospinning	100	200	1.5	-	-	[4.15]
Au/MoS2	Chemical vapour deposition	500	60	15%	-	-	[4.16]
CuO/V_2O_5	chemical route	50	300	1.5			[4.17]
Au-V_2O_5	sol-gel method	100	475	40	-	-	[4.18]
TiO_2-layer-modified SnO_2	Atomic layer deposition	1	300	44%*	~500		[4.34]
SnO_2 thin film	Spray pyrolysis	260	350	34	28	94	[4.35]
SnO_2 nanowire	Spray pyrolysis	260	350	1	25	28	[4.36]
SnO_2	Sol-gel method	50	220	55	20	N/A	[4.37]
Ni-SnO2	screen printing	50	375	40	6	39	[4.38]
In/Pd/SnO_2	Sol-gel	50	140	20	15	20	[4.39]
Pt-SnO_2 nanoneedles	Hydrothermal	100	250	23.18	15	14	[4.40]

Concen., temp. and refs correspond to concentration, temperature and references. *Response = $((R_a/R_g)*100)$.

To further validate the long-term stability of our current sensor towards CO gas, the sensor was stored for 6 months and the effect of storage in the sensor resistance in air (R_a) was investigated, see Fig. 4.7(a). As shown in Fig. 4.7(a), the Ra increased with the storage time, and this increase is more significant for six months storage. As confirmed from the stability analyses, (see the inset, Fig. 4.7(a)), the sensor response decreased after six months of storage, confirming the change in R_a has significant effect on the sensing performance. Such decrease could be due to absorption of moisture during storage.

Furthermore, the SnO_2-NaOH based sensor was tested towards CO at various exposure times, of 5-, 30-, 60- ,180- and 500 min. It was observed that the change in sensor resistance increases with the exposure time. Such behaviour can be witnessed on the sensor response (see Fig. 4.7(c)), which increases with the exposure time. This behaviour clearly shows that the exposure time has a significant effect on the sensing performance. This proposes that our current SnO_2-NaOH based sensor possesses numerous active sites on the surface that need adequate time to be accessed. This demonstrates good signs that these structures possess great ability to be utilized as acetone detection and monitoring even in reduced oxygen environment. This behaviour was also witnessed by Mokoena et al. [4.27], using the p-type NiO nanostructures, which was tested towards propanol vapour.

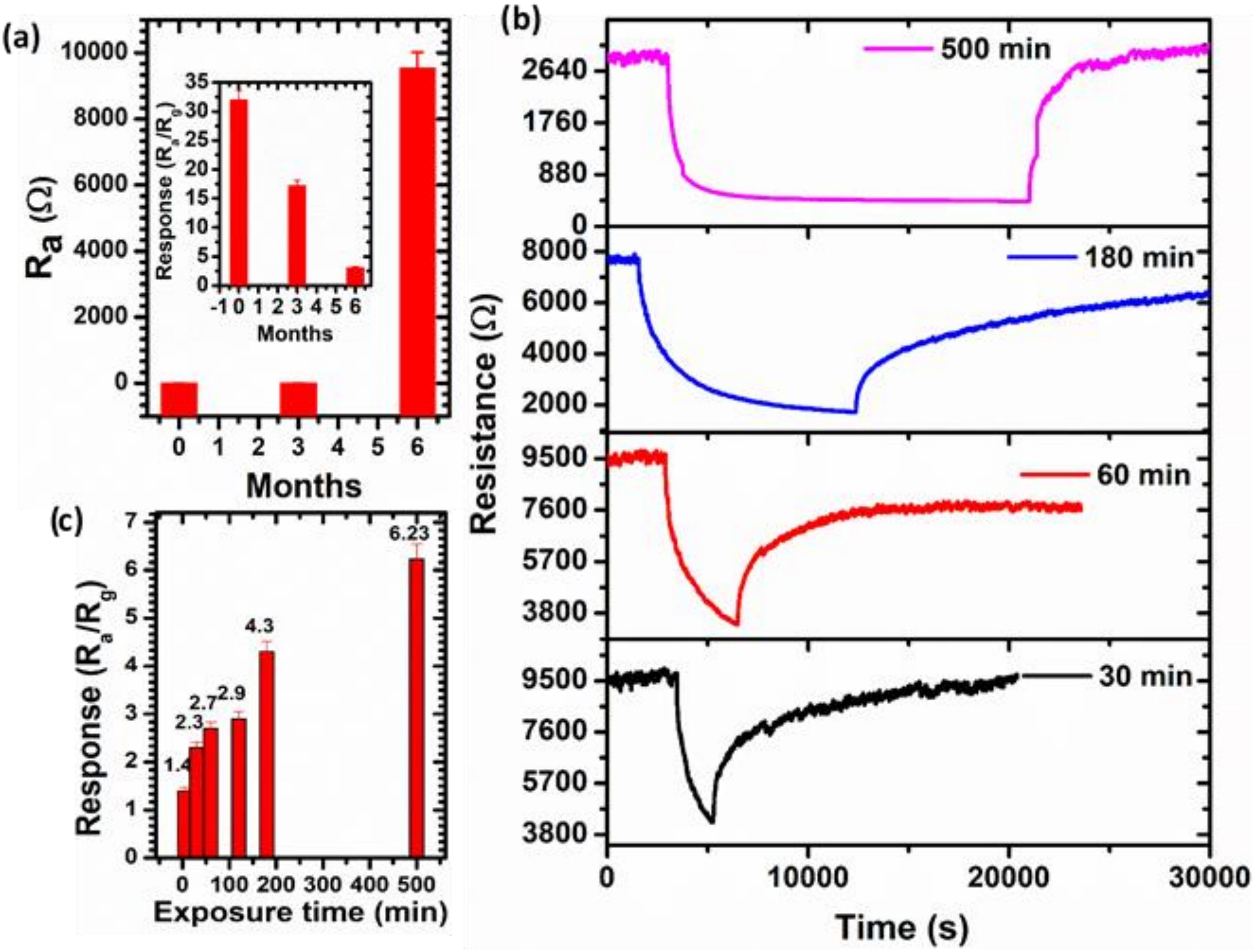

Fig. 4.7: R_a of the SnO_2-NaOH versus number of months, (b-c) Resistance and response versus exposure time towards 60 ppm CO gas at 75 °C. Note inset corresponds to long-term stability.

4.3.3. Gas sensing mechanism.

The gas sensing mechanism of SnO_2 based sensor as an n-type is based on the change in resistance. Basically, when the sensing layer is exposed in air, the molecular oxygen species gets absorbed on the surface of the sensor. Because of the higher oxygen electron affinity, the oxygen species adsorbed on the surface of the SnO_2-NaOH sensing layer receive electrons from the SnO_2-NaOH conduction band and gets chemisorbed ions [4.41, 4.42]. Based on the sensing temperature, particular oxygen species formed (e.g., O_2^-, O^-, and O^{2-}), result in a creation of a depletion layer to increase the sensing resistance. Lately, the V_O has been accepted to enhance the sensing performance. The presence of V_O in an n-type SnO_2-NaOH sensor hastens the adsorption of charge transfer of the CO gas. Basically, individually V_O provides two electrons, as a result, a higher relative V_O concentration in the SnO_2-NaOH hollowspheres leads in a greater number of electrons that can be absorbed and utilized for gas sensing performance. In addition, studies have anticipated the new radical Sn^{4+}-O_2^- that is paramagnetically dynamic and plays a vivacious part in the gas sensing mechanism: as depicted using Kruger Vink notation (Eqs. 4.1-4.3) [4.43].

$$O_O^X \Leftrightarrow V_O^{\bullet} + \tfrac{1}{2}O_2 + e^- \tag{4.1}$$

$$O_O^X \Leftrightarrow V_O^{\bullet\bullet} + \tfrac{1}{2}O_2 + 2e^- \tag{4.2}$$

$$Sn^{4+} - O_2^- \Leftrightarrow Sn^{3+} + V_O^{\bullet\bullet} + O_2 + 3e \tag{4.3}$$

Thus, upon introducing the CO gas, the adsorbed oxygen ions (O_2^-) interact with the CO molecules and release the trapped electrons back to the conduction band that lessen the depletion layer (see scheme 1), which reduces the sensor resistance. The reaction of the CO molecules on the sensor surface is depicted in eq. 4.4 as:

$$2CO(gas) + O_2^-(ads) \rightarrow 2CO_2(gas) + e^- \tag{4.4}$$

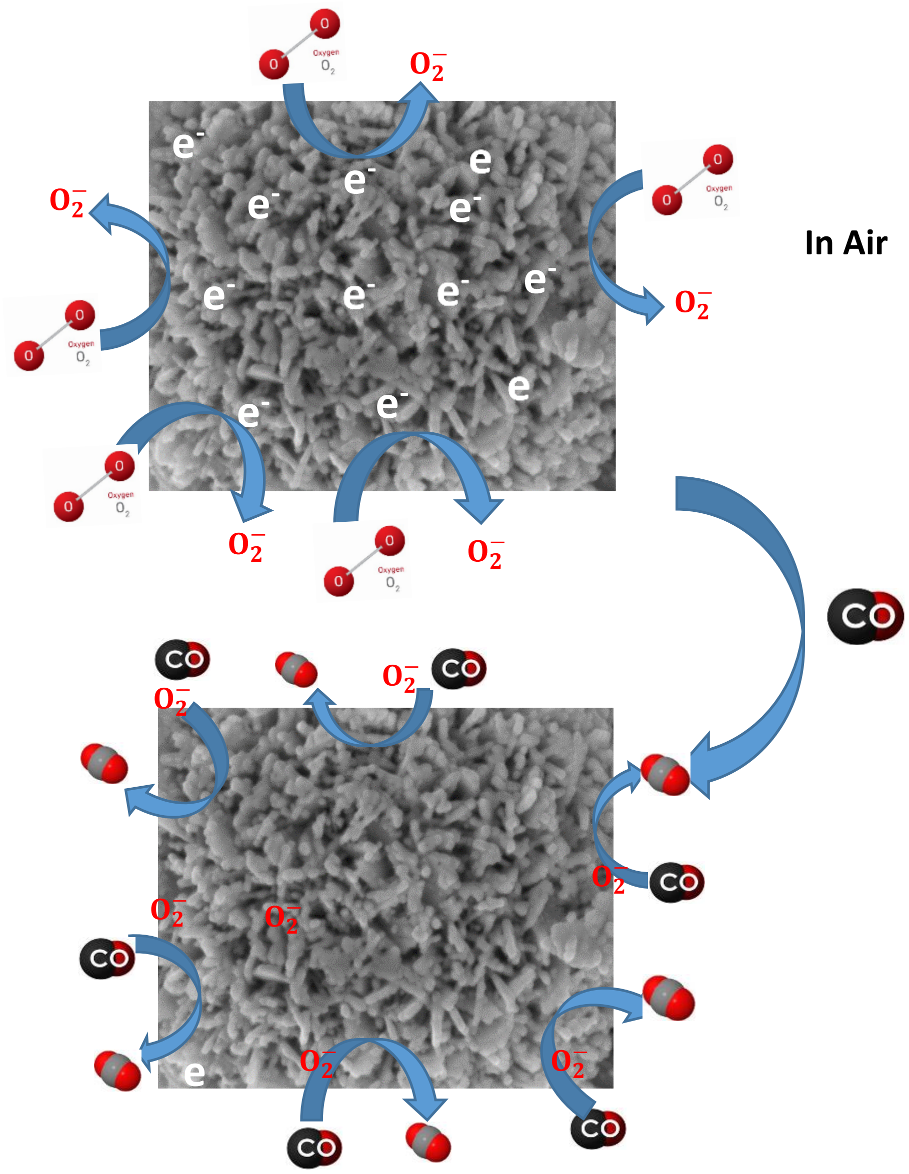

Scheme 1: Schematic drawing displaying the mechanism of SnO$_2$-NaOH towards CO gas.

To elucidate the reason behind improved response of the SnO$_2$-NaOH based sensor to CO further analyses were performed. According to the XRD analyses, all the SnO$_2$ based materials displayed the same exposed facets, and crystal structures. Nonetheles, the in-situ analyses from both PL and EPR showed that the SnO$_2$-NaOH possess more V$_O$ defects.

EPR studies in Fig. 4.8(a) demostrate that all the SnO_2 and V_2O_5 nanostructures pesent are paramagnetic signal. The paramagnetic signals of the SnO_2-NaOH, SnO_2-NH_4OH, SnO_2-Urea are located at 341.9 mT, 337.1 mT and 340.5 mT, respectively. While the V_2O_5-NaOH, V_2O_5-NH_4OH and V_2O_5-Urea all illustrated the signal at 340.2 mT, showing no shift on the magnetic field. The magnetic field shift observed for the various SnO_2 nanostructures was also witnessed on the XRD results. This was justified as the change in the morphological and structural changes. It is interesting to note that the SnO_2-NaOH shows a broad peak-to-peak (ΔH) signal in comprasion to its counterparts (see Fig. 4.4(a)). This broad signal denotes that the material indeed posseses a singificant amount of defects. It is futher noted that both the SnO_2-NaOH and SnO_2-NH_4OH showed the g-factor of 2.01 associated to the presence of superoxide radical O_2^- that formed due to the electrons transfer trapped in V_O. [4.44, 4.45,]. While the SnO_2-Urea showed a g-factor of 2.2. The V_2O_5 displayed a g-factor of 1.949 associated to characteristic of V^{4+} aggregates [4.46]. As noted in Fig. 4.8(a) and (b), the EPR intensity of the SnO_2-NaOH is larger than that of other SnO_2 structures and as well of those of V_2O_5 nanostructures, denoting higher relative concentration of V_O.

We further carried out the in-situ EPR analyses for SnO_2-NaOH at various temperatures 293K (25 ºC), 373K (75 ºC) and 448 K (150 ºC) to mimic the sensing analyses. As depicted in Fig. 8(c), a slight increase in the paramagnetic signal at 75 ºC is observed, while at 150 ºC, the signal reduced strongly compared to that at 25 and 75 ºC, respectively. The increase in paramagnetic signal is related to a higher relative concentration of V_O. Such increased signal at 75 ºC fits well with the superior response witnessed at the same temperature (i.e. 75 ºC).

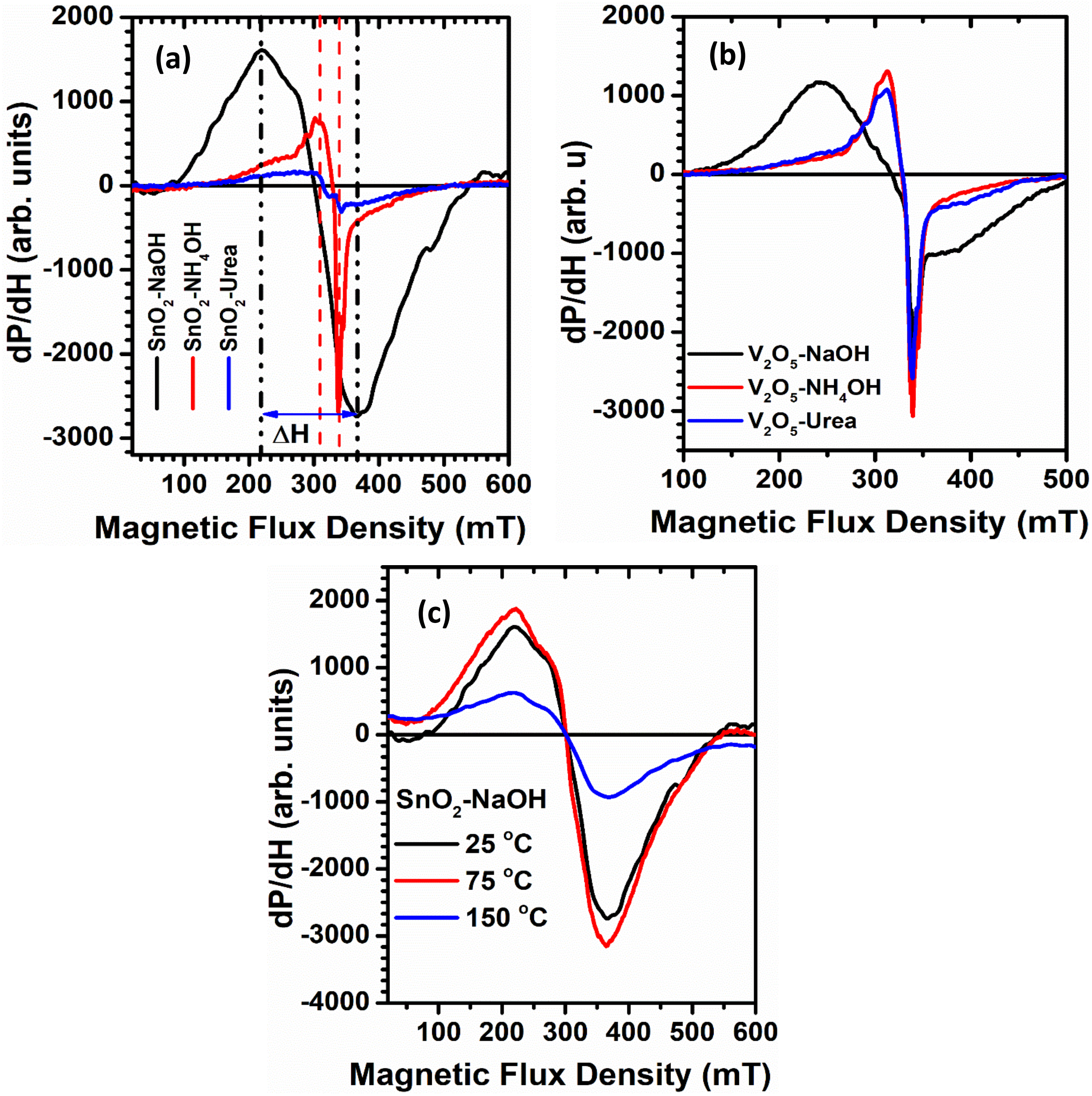

Fig. 4.8: EPR spectra of the various (a) SnO_2 and (b) V_2O_5 nanostructures.

To further support the improved sensing performance induced by SnO_2-NaOH towards CO gas, we conducted the in-situ PL analyses at the same temperatures (23, 75 and 150 °C) used during the gas sensing measurements (see Fig. 4.9). It is interesting that among the nanostructures, only the SnO_2-NaOH displays a strong shoulder in the region of 2.82-3.22 eV and a broad emission of 1.93 – 3.2 eV (Fig. 4.9). This unique emission is consistent with the broad paramagnetic signal observed on the EPR analyses. Besides, the images in the insets also validate that the base indeed plays a role on the luminescence properties, since the colour changes from black to reddish, then to grey for the SnO_2-NaOH, SnO_2-NH_4OH and SnO_2-urea, respectively. Furthermore, from the supporting information (Fig.A4), the deconvoluted peaks for the SnO_2-NH_4OH and SnO_2-urea samples show peaks at 2.27-3.31 eV, respectively. Basically, typical kind of oxygen defects that behave like luminescence centers in the SnO_2 band gap are V_O, V_O^+ and V_O^{++}. Thus, for the SnO_2, the peak at 3.0 eV is associated to the near band edge (NBE), while the broad emission peak at 2.88-1.92 eV is associated with surface oxygen deficiency state V_o and electron transition mediated by V_O [4.19]. For the V_2O_5, the emission at 3.1 eV and 2.8 eV are linked to the main transition between the conduction band, E_C (V3d states) and valence band V_B (O2p states) and the band edge transition in V_2O_5 [4.47]. Moreover, the images of the V_2O_5 shows a clear colour change from black to yellow and then to reddish for the V_2O_5 -NaOH, V_2O_5 -NH_4OH, and V_2O_5-Urea, respectively.

As noted from Fig. 4.9, the in-situ study denotes that the emission of both SnO_2 and V_2O_5 for all the bases decreases with the operating temperature. It is remarkable to note that while the full width at half-maximum (FWHM) becomes narrower for all other samples with the in-situ temperature, nonetheless, the FWHM of the SnO_2 reflected not to decrease, especially at 75 °C.

The PL emission peak of the temperature in-situ analyses at 75 °C of various bases were compared for both SnO_2 and V_2O_5 (see Fig. 4.9(g) and (h). Among the SnO_2 based samples, the SnO_2-NaOH still revealed a higher intensity and its emisison becoming broad from 1.5 to 3.2 eV. When comapring the SnO_2 and V_2O_5 samples prepared using various bases, it is observed in Fig. 4.6 that the SnO_2-NaOH contains a higher number of defects in comparison to other materials.

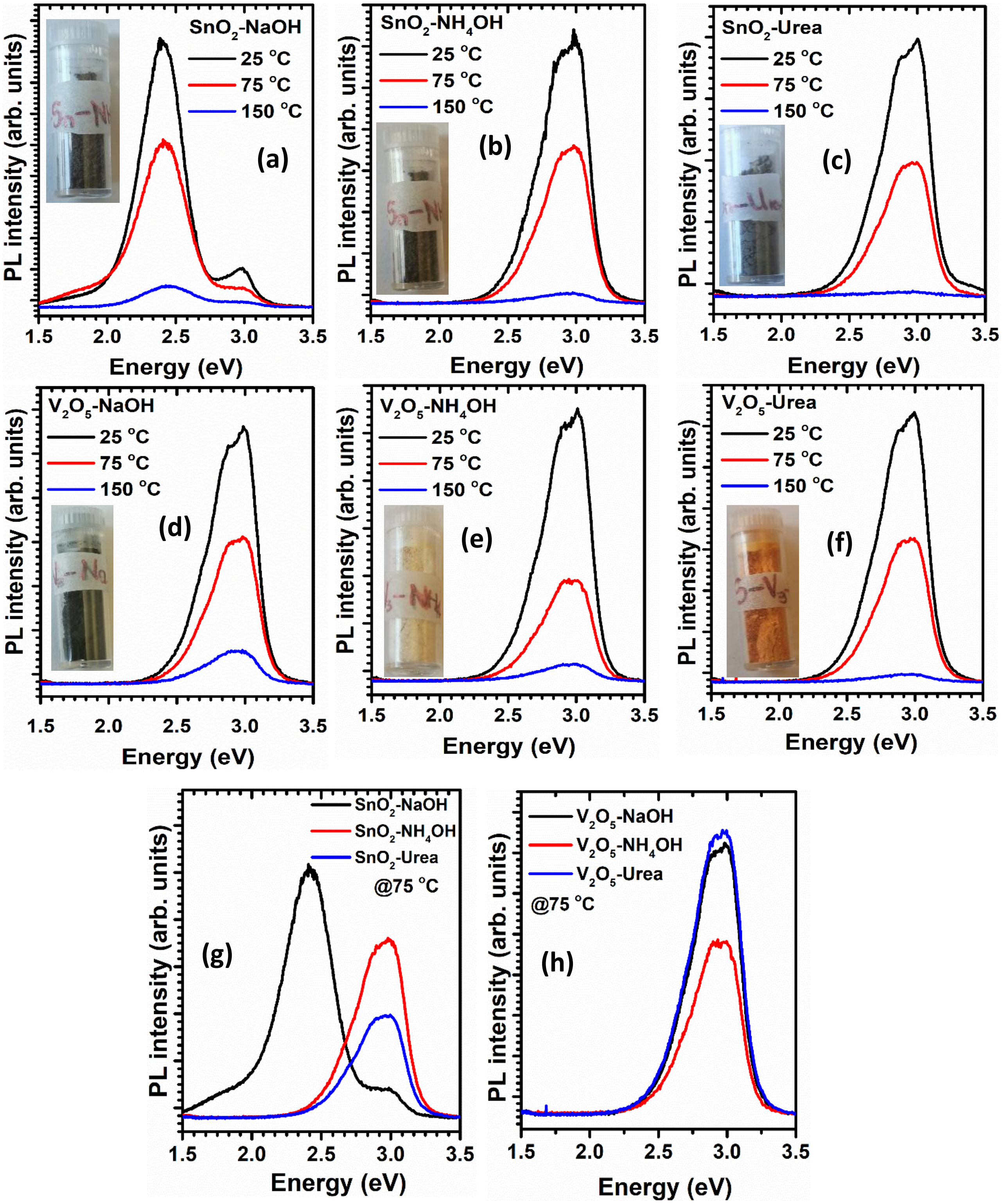

Fig. 4.9: PL emission spectra of SnO_2, V_2O_5 nanostructures prepared using various bases measured at different temperatures and comparison of SnO_2 and V_2O_5 nanostructures at 75 °C.

The increase in sensing response is also associated with the smaller crystallite sizes observed for the SnO_2-NaOH, which lead to higher sensitivity and of course increased surface defects, such as V_O. For instance, based on the energy level theory, the particle size of SMO influences the resistances of the materials. Yamazoe et al. [4.48] stated the SnO_2 based sensing sensitivity with particle sizes in the range of 5 and 32 nm. They observed that the sensitivity of SnO_2 based sensor improves strongly once the particle's diameter is smaller than two times the electron depletion layer thickness (L). Besides, Kortidis et al. [4.49] have shown a clear correlation between the crystallite sizes and gas sensing performance, when using ZnO nanostructures prepared at various reaction temperatures. Basically, their sensing response was improved for the smallest crystallite sizes of the material.

Besides, the base may also play a role on the sensing characteristics, since the SnO_2 prepared from NaOH base showed improved response in comparison to other bases (NH_4OH and urea). This could probably be due to the strength of the base, which follows in this manner, i.e., NaOH>NH_4OH>Urea, where the strong base leads to improved formation of porous structures, allowing better gas desorption/adsorption, resulting to superior sensing performance. This demonstrates that the surface enlargement phenomenon is affected by the nature and strength of the base. Sikhwivhilu et al. [4.50] have shown that TiO_2 samples treated with NaOH were more porous and displayed higher surface area in comparison to those treated with other bases (i.e., LiOH or NH_4OH).

To further validate our findings, we linked the sensing performance with the number of spins and the PL intensity ratio extracted from both the in-situ EPR and PL analyses, see Fig. 4.10. Since the V_O has the capabilities of enhancing the gas detection and sensitivity, as a result the existence of a superior amount of V_O may be able to enhance the oxygen adsorption, which in turn improve the interaction between the adsorbed oxygen and the CO gas. Therefore, this justifies the observed increase in CO response with the number of spins (or paramagnetic V_O) and as well as the PL intensity ratio in Fig. 4.10(a) and (b). This behaviour indeed displays a clear correlation. Hence, the quantity of paramagnetic V_O is linked to the amount of electrons achieving the E_C of SnO_2 [4.43, 4.45]. Motsoeneng et al. [4.46] reported a correlation between the number of spins and propanol response using a SnO_2 hollowspheres based sensor. They also found that the propanol response increases with the paramagnetic V_O. Though their sensing response was roughly 15 at 75 °C. which was twice smaller than the current response (~22). Moreover, Oosthuizen et al. [4.41] reported a clear correlation between the response versus the relative concentration of V_O and surface to volume ratio.

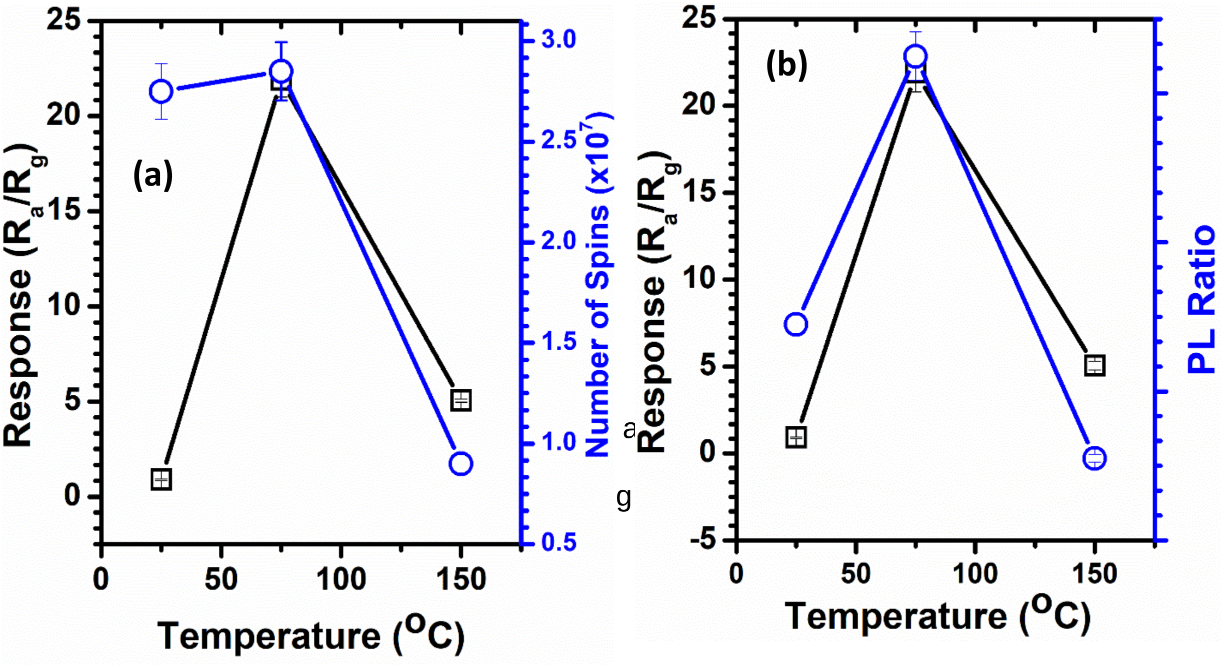

Fig. 4.10: (a) Response versus number of spins and (b) Response versus PL intensity ratio of SnO_2-NaOH based sensor at various operating temperature. Note that the analyses were done using both in-situ PL and EPR.

Lee et al. [4.51] have reported using the DFT calculation that the presence of V_O does not only enhance the electron concentration in E_c of the sensing layer. It further persuades a creation of the local built-in electric field, enhancing the electron migration proportion in the sensing layer. Additionally, the electron transfer movement after interaction with the adsorbed oxygen, is better in comparison to that after interaction with CO gas. The presence of V_O is beneficial to endorsing the creation of numerous adsorbed O_2^- on the sensing layer surface, establishing an extensive electron depletion layer. Consequently, existence of V_O plays a significant character in enlightening the CO gas response of the SnO_2-NaOH based sensor.

4.5. References.

[4.1] I. Manisalidis, E. Stavropoulou, A. Stavropoulos, E. Bezirtzoglou, Environmental and health impacts of air pollution: A Review. Front. Public Health, 8 (2020) 1-10.

[4.2] X. Yan, Y. Wu, R. Li, C.Shi, R. Moro, Y. Ma, L. Ma, High-performance UV-assisted NO_2 sensor based on chemical vapor deposition graphene at room temperature, ACS Omega. 4(10) (2019) 14179-14187.

[4.3] M. Matooane, J. John, R. Oosthuizen, M. Binedell, Vulnerability of South African communities to air pollution, Proceedings: 8th World Congress on Environmental Health, 2004, ISBN: 0-9584663-7-8.

[4.4] J. Wichmann and K. Voyi, Air pollution epidemiologic studies in South Africa - Need for freshening up, Rev. Environ. Health 20(4) (2005) 265-301.

[4.5] L.D. Prockop, R.I. Chichkova, Carbon monoxide intoxication: an updated review, J. Neurol. Sci. 262 (2007) 122–130.

[4.6] M. Mashock, K. Yu, S. Cui, S. Mao, G. Lu, J. Chen, Modulating gas sensing properties of CuO nanowires through creation of discrete nanosized p–n junctions on their surfaces, ACS Appl. Mater. Interfaces 4 (2012) 4192–4199.

[4.7] M. Law, H. Kind, B. Messer, F. Kim, P. Yang, Photochemical sensing of NO_2 with SnO_2 nanoribbon nanosensors at room temperature. Angew. Chem. 41(2002) 2405–2408.

[4.8] D. Chen, J. Ye, Hierarchical WO_3 hollow shells: dendrite, sphere, dumbbell, and their photocatalytic properties, Adv. Funct. Mater. 18 (2008) 1922–1928.

[4.9] Z. Tshabalala, K. Shingange, F. Cummings, O. Ntwaeaborwa, G. Mhlongo, D. Motaung, Ultra-sensitive and selective NH_3 room temperature gas sensing induced by manganese-doped titanium dioxide nanoparticles, J. Col. Interf. Scie. 504 (2017) 371-386.

[4.10] N. Yamazoe, G. Sakai, K. Shimanoe, Oxide semiconductor gas sensors, Catal. Surv. Asia 7 (2003) 63–75.

[4.11] J.-H. Kim, A. Mirzaei, J.-Y. Kim, J.-H. Lee, H.W. Kim, S. Hishita, S.S. Kim, Enhancement of gas sensing by implantation of Sb-ions in SnO_2 nanowires, Sens. Actuators B Chem. 304 (2020) 127307.

[4.12] S. Das, V. Jayaraman, SnO_2: A comprehensive review on structures and gas sensors, Prog. Mater. Sci. 66 (2014) 112–255.

[4.13] A.K. Mauraya, P.Singh, S. Muthiah, S.S. Kushvaha, S.K. Muthusamy, Effect of post-oxidation processes and thickness of SnO_2 films prepared by vacuum evaporation on CO gas sensing characteristics, Ceramics International 47 (2021) 13015–13022.

[4.14] J.-H. Kim, J.-Y. Kim, A. Mirzaei, H.W. Kim, S.S. Kim, Synergistic effects of SnO_2 and Au nanoparticles decorated on WS_2 nanosheets for flexible, room-temperature CO gas sensing, Sens. Actuators: B. Chemical 332 (2021) 129493.

[4.15] N.N. Viet, L.V. Thong, T.K. Dang, P.H. Phuoc, N.H. Chien, C.M. Hung, N.D. Ho, N.V. Duy, N.V. Toan, N.T. Son, N.V. Hieu, MoS_2 nanosheets-decorated SnO_2 nanofibers for enhanced SO_2 gas sensing performance and classification of CO, NH_3 and H_2 gases, Analytica Chimica Acta 1167 (2021) 338576.

[4.16] Y. Kim, S. Kang, N.-C. Oh, H.-D. Lee, S.-M. Lee, J. Park, H. Kim, Improved Sensitivity in Schottky Contacted Two-Dimensional MoS_2 Gas Sensor, ACS Appl. Mater. Interfaces 11 (2019) 38902–38909.

[4.17] Bu-Yu Yeh,a Bo-Sung Jian,a Gou-Jen Wang b and Wenjea J. Tseng, CuO/V_2O_5 hybrid nanowires for highly sensitive and selective H_2S gas sensor, RSC Adv. 7 (2017) 49605-49612.

[4.18] G.N. Abkenar, J.P Viricelle, M. Rieu, P. Breuil, Study of two vanadium based materials as working electrode for developing a selective mixed-potential ammonia sensor, Proceedings 2 (2018) 770; doi:10.3390/proceedings 2130770.

[4.19] A. Azam, S.S. Habib, N.A. Salah, F. Ahmed, Microwave-assisted synthesis of SnO_2 nanorods for oxygen gas sensing at room temperature, International Journal of Nanomedicine 8 (2013) 3875-3882.

[4.20] Z.P. Tshabalala, H.C. Swart, D.E. Motaung, Fabrication of TiO_2 nanofibers-based sensors for enhanced CH_4 performance induced by notable surface area and acid treatment, Vacuum 187 (2021) 110102.

[4.21]https://www.hsa.ie/eng/Publications_and_Forms/Publications/Chemical_and_Hazardous_Substances/Carbon_Monoxide.pdf (accessed on the 11th July 2021).

[4.22] https://www.epa.gov/indoor-air-quality-iaq/carbon-monoxides-impact-indoor-air-quality (accessed on the 11th of July 2021).

[4.23] A. Mauraya, D. Mahana, P. Pal, S. Muthiah, P. Singh, S. Muthusamy, Effect of bulk and surface modification of SnO_2 thin films with PdO catalyst on CO gas sensing characteristics prepared by vacuum evaporation process, J. Alloy. Comp. 843 (2020) 155979.

[4.24] Q. Zhou, L. Xu, A. Umar, W. Chen, R. Kumar, Pt nanoparticles decorated SnO_2 nanoneedles for efficient CO gas sensing applications, Sensors and Actuators B: Chemical, 256 (2018) 656-664.

[4.25] M.M. Doroodmand, S. Sepehri, T. Poorshamsi, Room temperature quartz crystal microbalance-based CO sensor using commercial piezoelectric crystal modified with carbon nanostructures, Sci. Adv. Mater. 7 (2015) 1379–1386

[4.26] S. Basu, P.K. Basu, Nanocrystalline metal oxides for methane sensors: role of noble metals, Sensors, 86 (2009), pp. 1968-1988.

[4.27] T.P. Mokoena, H.C. Swart, K.T. Hillie, Z.P. Tshabalala, M. Jozela, J. Tshilongo, D.E. Motaung, Enhanced propanol gas sensing performance of p-type NiO gas sensor induced by exceptionally large surface area and crystallinity, Applied Surface Science, 571 (2022) 151121.

[4.28] Z.S. Hosseni, A. Iraji zad, A. Mortezaali, Room temperature H_2S gas sensor based on rather aligned ZnO nanorods with flower-like structures, Sens. Actuators B, 207 (2015) 865-871.

[4.29] T.P. Mokoena, Z.P. Tshabalala, K.T. Hillie, H.C. Swart, D.E. Motaung, The blue luminescence of p-type NiO nanostructured material induced by defects: H_2S gas sensing characteristics at a relatively low operating temperature, Applied Surface Science, 525 (2020) 146002 (19 pages).

[4.30] M.M. Doroodmand, S. Sepehri, T. Poorshamsi, Room temperature quartzcrystal microbalance-based CO sensor using commercial piezoelectriccrystal modified with carbon nanostructures, Sci. Adv. Mater. 7 (2015) 1379–1386.

[4.31] N.D. Khoang, D.D. Trung, N.V. Duy, N.D. Hoa, N.V. Hieu, Sens. Actuators B 174(2012) 594.

[4.32] D.D. Trung, L.D. Toan, H.S. Hong, D.T. Lam, T. Trung, N.V. Hieu, Talanta 88 (2012)152.

[4.33] S. Mahajana, S. Jagtap, Metal-oxide semiconductors for carbon monoxide (CO) gas sensing: A review, Applied Materials Today 18 (2020) 100483.

[4.34] J.-H. Lee, A. Mirzaei, J.-H. Kim, J.-Y. Kim, A.F. Nasriddinovd, M.N. Rumyantsevad, Hyoun Woo Kim, S.S. Kim, Gas-sensing behaviors of TiO_2-layer-modified SnO_2 quantum dots in self-heating mode and effects of the TiO_2 layer Sensors & Actuators: B. Chemical 310 (2020) 127870.

[4.35] E. Brunet. T. Maier. G.C. Mutinati. S. Steinhauer. A. Köck. C. Gspan. W. Grogger. Comparison of the gas sensing performance of SnO2 thin film and SnO2 nanowire sensors. 2012. 113.

[4.36] D. Dang Trung. N. Duc Hoa. P. Van Tong. N. Van Duy. T.D. Dao. H.V. Chung. T. Nagao. Nguyen Van Hieu. Effective decoration of Pd nanoparticles on the surface of SnO_2 nanowires for enhancement of CO gas-sensing performance. (2013) 129-131.

[4.37] S.K. Tripathy, B.P. Hota, Carbon Monoxide Sensitivity of Tin Oxide Thin Film Synthesized by Sol Gel Method, The African Review of Physics (2012) 7:0047

[4.38] K.-Il Choi, M. Hübner, A. Haensch, H.-J. Kim, U. Weimar, N. Barsan, J.-H. Lee, Ambivalent effect of Ni loading on gas sensing performance in SnO_2 based gas sensor, Sensors and Actuators B: Chemical, 183 (2013) 401-410.

[4.39] T. Zhang, L. Liu, Q. Qi, S. Li, G. Lu, Development of microstructure In/Pd-doped SnO_2 sensor for low-level CO detection, Sensors and Actuators B: Chemical, 139, (2009) 287-291.

[4.40] Q. Zhou. L. Xu. A. Umar. W. Chen. R. Kumar. Pt nanoparticles decorated SnO2 nanoneedles for efficient CO gas sensing applications. Sensors and Actuators B: Chemical, 256, (2018) 656-664.

[4.41] D.N. Oosthuizen, D.E. Motaung, H.C. Swart, Gas sensors based on CeO_2 nanoparticles prepared by chemical precipitation method and their temperature-dependent selectivity towards H_2S and NO_2 gases, Applied Surface Science, 505 (2020) 144356.

[4.42] Z. Tshabalala, T. Mokoena, M. Jozela, J. Tshilongo, T. Hillie, H. Swart, D. Motaung, TiO_2 Nanowires for Humidity-Stable Gas Sensors for Toluene and Xylene. ACS Applied Nano Materials 4 (2021) 702-716.

[4.43] L. Armelao, D. Barreca, E. Bontempi, C. Canevali, L. E. Depero, C.M. Mari, R. Ruffo, R. Scotti, E. Tondello, F. Morazzoni, Can Electron Paramagnetic Resonance Measurements Predict the Electrical Sensitivity of SnO_2-based Films? Appl. Magn. Reson. 22 (2002) 89−100.

[4.44] R.G. Motsoeneng, I. Kortidis, S. Sinha Ray, D.E. Motaung, Designing SnO_2 Nanostructure-Based Sensors with Tailored Selectivity toward Propanol and Ethanol Vapors, ACS Omega 4 (2019) 13696−13709.

[4.45] M. Epifani, J.D. Prades, E. Comini, E. Pellicer, M. Avella, P. Siciliano, G. Faglia, A. Cirera, R. Scotti, F. Morazzoni, J.R. Morante, The Role of Surface Oxygen Vacancies in the NO_2 Sensing Properties of SnO_2 Nanocrystals. J. Phys. Chem. C 112 (2008) 19540− 19546.

[4.46] A.I. Kokorin, V.I. Pergushov, A.I. Kulak, EPR Evidence for Dynamic Rearrangements of Vanadium Paramagnetic Centers on the Surface of V-Doped Titanium Dioxide, Catalysis Letters 150 (2020) 263–272.

[4.47] T.K. Le, M. Kang, S.W. Kim, A review on the optical characterization of V_2O_5 micro-nanostructures, Ceramics International, 45 (2019) 15781-15798.

[4.48] N. Yamazoe, New approaches for improving semiconductor gas sensors, Sens. Actuators, B 5 (1991) 7–19

[4.49] I. Kortidis, H.C. Swart, S. Sinha Ray, D.E. Motaung, Detailed understanding on the relation of various pH and synthesis reaction times towards a prominent low temperature H_2S gas sensor based on ZnO nanoplatelets, Results in Physics 12 (2019) 2189–2201.

[4.50] L.M. Sikhwivhilu · S. Sinha Ray · N.J. Coville, Influence of bases on hydrothermal synthesis of titanate nanostructures, Appl Phys A (2009) 94: 963–973

[4.48] J.H. Lee, D.Y. Jo, J.W. Choung, C.H. Kim, H.C. Ham, K.Y. Lee, Roles of noble metals (M = Ag, Au, Pd, Pt and Rh) on CeO_2 in enhancing activity toward soot oxidation: active oxygen species and DFT calculations. J. Hazard. Mater. 403, (2021) 124085.

CHAPTER 5

Room temperature gas sensing of SnO_2/CuO heterostructures for the detection of NO_2 gas: Low-power Consumption gas sensor

5.1. Introduction

The demands of gas sensors have increased over the years as a means of minimizing the risk of air pollution and identifying dangerous, flammable, and poisonous gases that might endanger human heaths and the environment. Among other gases NO_2 is the most toxic gas. In South Africa, the populations are endangered from the sources that release NO_2 during operation, such as car exhaust, household and mining industries [5.1, 5.2]. Gas sensors are useful in coal industries to monitor the leakage of NO_2 from the containers and machines during manufacturing, which may lead to harm or explosion. Whereas in some houses where they used gas, wood, oil, kerosene, cigarettes and coal burning appliance, such as stoves, heaters, furnaces, boilers and fireplaces and gas engines, in cars and home generators, which contribute to the elevation of NO_2 levels makes gas sensor devices more preferable [5.3-5.6]. Semiconductors metal oxide (SMOs) gas sensors, among other gas sensors mentioned in the literature, have gained researchers' attention because of their chemical and physical characteristics [5.7]. Large sensitivity, low operating temperature (RT), stability, selectivity, and high surface area are some challenges that have been encountered in gas sensing [5.8]. To meet this requirement, researchers have introduced doping and annealing processes for materials [5.9]. Gas sensors are needed that have fast reaction times, high sensitivity, fast recovery times, low working temperatures, and strong selectivity for a variety of gases.

Copper oxide CuO, a p-type semiconductor metal oxide with a band gap of 1.7 eV, finds extensive use in gas sensors [5.10]. Due to its potential use in gas sensors, solar cells, lithium-ion batteries, and light emission, among other things, Tin dioxide (SnO_2) which is an n-type semiconductor metal oxide with a wide band gap of 3.6 eV, has attracted interest in several research areas. This is because of its chemical and physical characteristics, which include low cost, low resistance, high transparency, and high electrical conductivity [5.11]. To improve the materials' detecting capabilities, SnO_2/CuO composite has been synthesized for use in gas sensors using facile hydrothermal procedures.

5.2. Experimental method

5.2.1. Material used

Tin chloride dehydrate ($SnCl_2.2H_2O$) and Copper (II) acetate monohydrate ($C_4H_8CuO_5$).

5.2.2. Synthesis

The autoclave hydrothermal method was employed to synthesis pure SnO_2, CuO and SnO_2/CuO with various molar concentrations (0.5:1.0M, 1.0:0.5M and 1.0:1.0). The certain amount of $SnCl_2.2H_2O$ and ($C_4H_8CuO_5$), 0.5M of $SnCl_2.2H_2O$ and 1.0M of $C_4H_8CuO_5$ precursors were added in separate beakers with 150ml of distilled water, the solution was stirred for 1 hour using magnetic stirrer. The solution was then deposited in a Teflon liner then into autoclave stainless steel before heated at 180ºC in an oven for 16 hours. The solution was then cooled and the products was centrifuged 10 times in the time interval of 10 minutes using mode-TJ-6 centrifuge machine. The product was heated (dried) at 90ºC, the final product SnO_2 and CuO power were then grinned using pestle and mortar. The power were then characterized. The same procedure was repeated for SnO_2/CuO with the mole ratio of (1.0:0.5M and 1.0:1.0).\

5.2.3. Characterization

The structure of the materials was probed using a (XRD, Bruker AXS D8 Advance x-ray diffractometer, Cu Kα radiation λ= 0.154056). The scanning electron microscopy (SEM, ZEISS Auriga) and transmission electron microscopy (Tecnai) were utilized to examine the surface morphology, internal structure and elemental composition of the materials. UV-vis spectrometer was used to study the optical characteristics of the the materials.

5.3. Results and discussion.

Fig. 5.1 displays the XRD patterns of SnO_2/CuO with various molarity (0.5: 1.0M, 1.0: 1.0M and 1.0: 0.5) and of pure CuO and SnO_2 respectively. The SnO_2/CuO, CuO and SnO_2 samples were annealed at 400 ºC for two hours. The XRD pattern for pure SnO_2 depict all peaks in an amorphous nature implying the disorderly arrangement within each diffracting angles. All peaks for pure CuO shifted with approximately 1º to lower diffracting angles, which may be attributed to crystallite sizes and lattice strain. Moreover, sharper peaks are observed indicating that CuO has higher crystallinity with low intensities which may be due to chaotic arrangement (disorder) of crystal at all the diffracting angles. The present of unknown peak is observed at $2\theta=25.46^{\circ}$ which is due to impurities. The CuO XRD pattern depicts a monoclinic structure despite the shifts, forming a single CuO phase.

The XRD pattern of SnO_2/CuO-0.5:1.0M depicts peaks at 2θ=26.75º, 2θ=33.86 º, 2θ=35.66 º, 2θ=38.84 º, 2θ=49.90 º, 2θ=51.12 º, 2θ=58.40 º and 2θ=61.67 º which correspond to the following planes of SnO_2 (110), (101), (200), (210), (211), (220), (022) and (310) which confirm that SnO_2 has a tetragonal structure which agree with the standard (JCPDS card no. 01-077-0452). The broad peaks observed at 2θ=26.75º, 2θ=33.86 º and 2θ=51.12 º exhibited that the material has poor crystallinity for those diffracting peaks which may be due to the synthesis method applied. The XRD pattern of SnO_2/CuO-1.0:1.0M reveals peaks at 2θ=26.81º, 2θ=33.95º, 2θ=35.68 º, 2θ=38.86 º, 2θ=49.00 º, 2θ=52.00 º, 2θ=58.38 º and 2θ=61.80 º corresponding to the following planes of SnO_2 (110), (101), (200), (210), (211), (220), (022) and (310), the present of sharper peaks are observed indicating good crystallinity and broad peaks indicating poor crystallinity at other diffracting angles are also observed. The XRD pattern for SnO_2/CuO-1.0:0.5M and SnO_2/CuO 1.0:1.0M depict similar peaks but with different unequal intensities. The materials formed only one phase and there are no unknown peaks revealing that the materials are pure. The molar concentrations have impacts on the crystallinities of the materials, this is supported by various XRD pattern as some peaks are amorphous and some has improved crystallinity. The crystallite sizes (D) of the materials listed in Table 5.1 were calculated using Debye's Scherrer equation:

$$D=\frac{K\lambda}{\beta\cos(\theta)} \qquad (5.1)$$

where D is the particle size, K is known as the Scherer's constant (K=0.9), λ is the X-ray wavelength (1.5406Å), β (in radians) is full width at half maximum (FWHM) of the diffraction peak and θ is the diffracting angle between planes. The space (d) between the crystal layer is calculated using equation (5.2)

$$d=\frac{n\lambda}{2sin(\theta)} \tag{5.2}$$

where *λ* is the wavelength of the x-ray, *d* is the spacing of the crystal layer and *θ* is the incident angle.

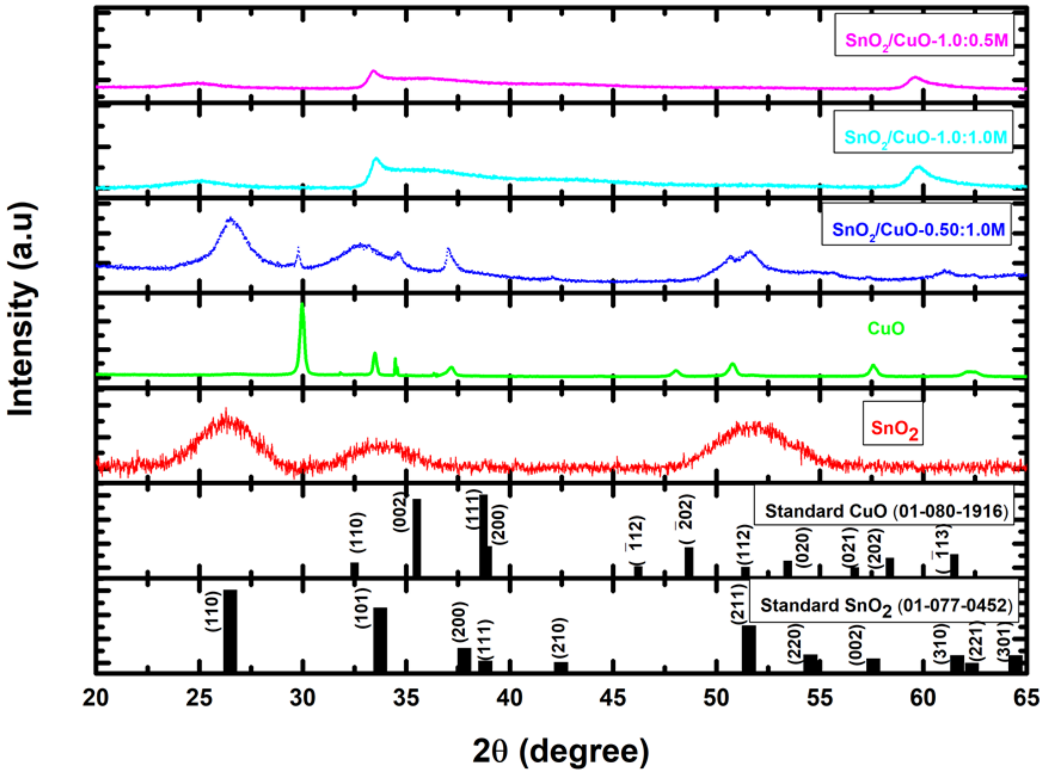

Fig. 5.1: XRD pattern of pure SnO_2 and CuO, SnO_2/CuO with different molar concentration and SnO_2, CuO standard JCPDS.

Table 5.1. Calculated values for FWHM using Origin and Crystallite size using Scherrer equations and Lattice parameters for the synthesized SnO_2, CuO, SnO_2/CuO with different molar concentrations.

Material	FWHM β (rad)	d-spacing (nm)	Crystallite size by Debye's formula (nm)	Position (º)	planes
SnO_2	0.036	0.14	3.95	26,34	(110)
CuO	0.040	0.12	3.46	24.82	(110)
SnO_2/CuO- 1.0:0.5M	0.010	0.08	14.01	38.86	(111)
SnO_2/CuO- 1.0:1.0M	0.040		3.58	26.78	(110)
SnO_2/CuO- 0.5:1.0M	0.006	0.12	24.09	38.86	(111)

Fig. 5.2 shows the SEM micrographs of the SnO_2/CuO heterostructures. The SnO_2/CuO- (1.0:0.5M) in Fig. 5.2(a) shows agglomerated nanoparticles. While the SnO_2/CuO- (1.0:1.0M) in Fig. 5.2(b) displays spherical nanoparticles with an average diameter of 50 nm. The surface morphology shows a porous structure, which could be suitable for adsorption gas molecules. The SnO_2/CuO- (0.5:1.0M) in Fig. 5.2(c) shows larger nanoparticles, with an average diameter of 70-100 nm.

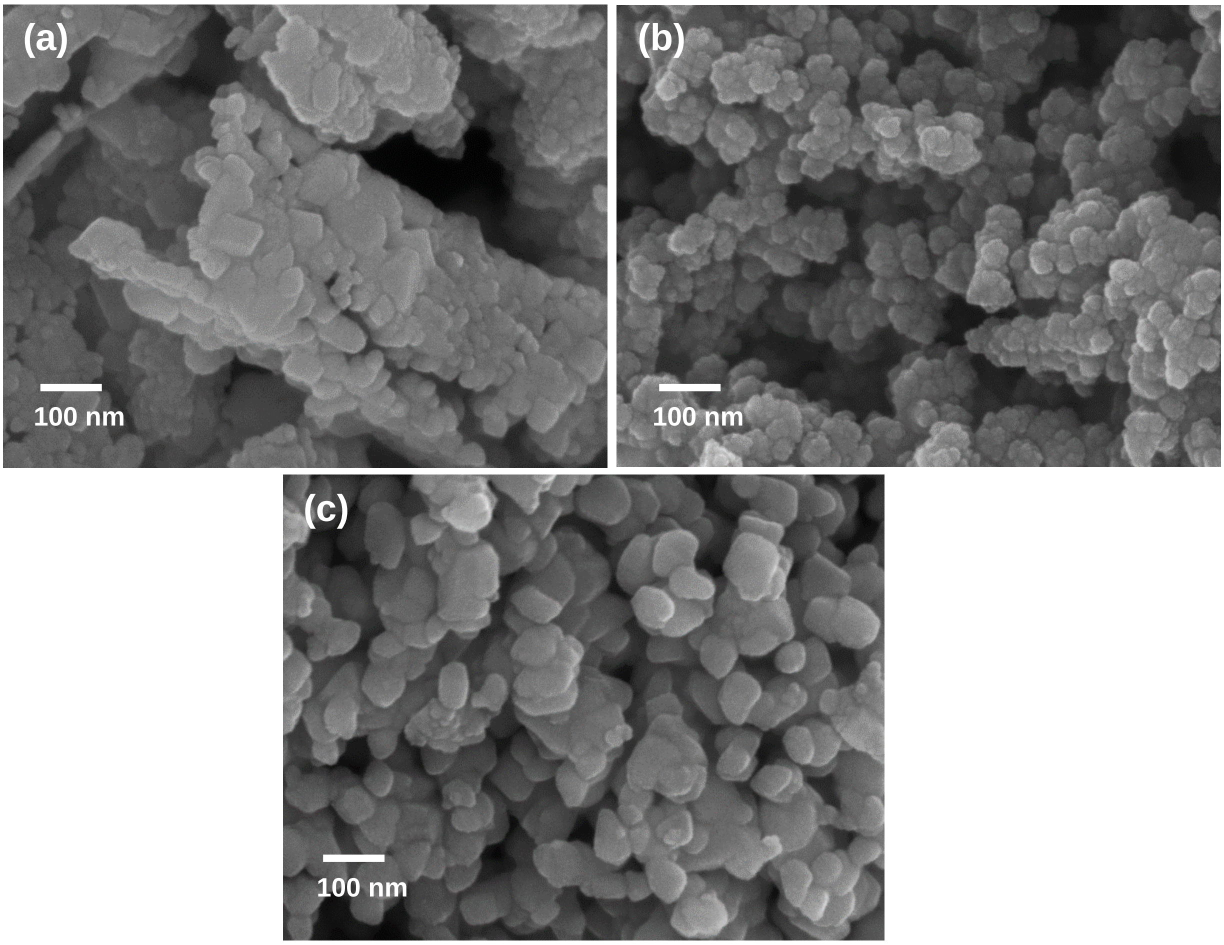

Fig. 5.2. SEM micrographs of (a) SnO_2/CuO-(1.0:0.5M), (b) SnO_2/CuO- (1.0:1.0M) and (c) SnO_2/CuO- (0.5:1.0M).

High resolution-TEM micrographs of the SnO_2/CuO heterostructures of various molar concentration are shown in Fig. 5.3 (a), (c) and (e). As shown in Fig. 5. all the nanostructures are made of nanoparticles, and this confirm the SEM findings. The selected area electron diffraction (SAED) patterns in Fig. 5.3 (b), (d) and (f) shows that the materials are polycrystalline. The SAED in Fig. 5.3 (b) and (d) shows diffused Debye ring, indicating that the materials are amorphous as confirmed from the XRD analyses. The SAED in Fig. 5.3 (f) shows that the materials are more crystalline than its counterparts. Additonally, several planes associated with CuO and SnO_2 were observed.

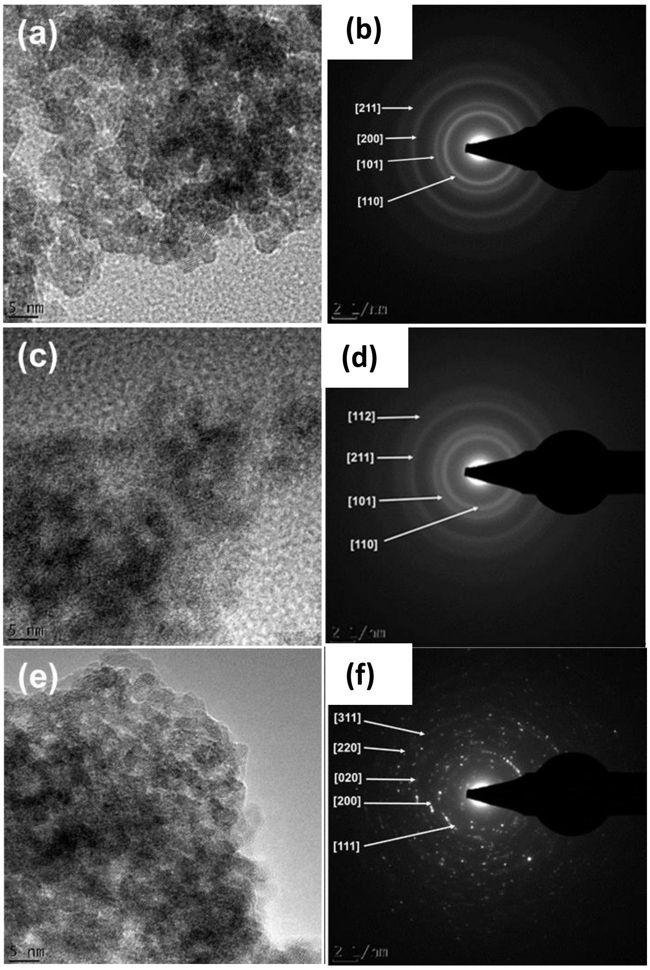

Fig. 5.3: HR-TEM images (a) SnO_2-CuO (1: 0.5), (c) SnO_2-CuO (0.5: 1), (e) SnO_2-CuO (1:1), corresponding to SAED patterns (b), (d) and (f)

To confirm an appropriate distribution of CuO on SnO_2 matrix, STEM- EDS SI maps of CuO/SnO_2 -(1.0:1.0M) were carried out. From the maps in Fig. 5.4, it is evident that both Cu, Sn and O are distribubeted homogeneuosly.

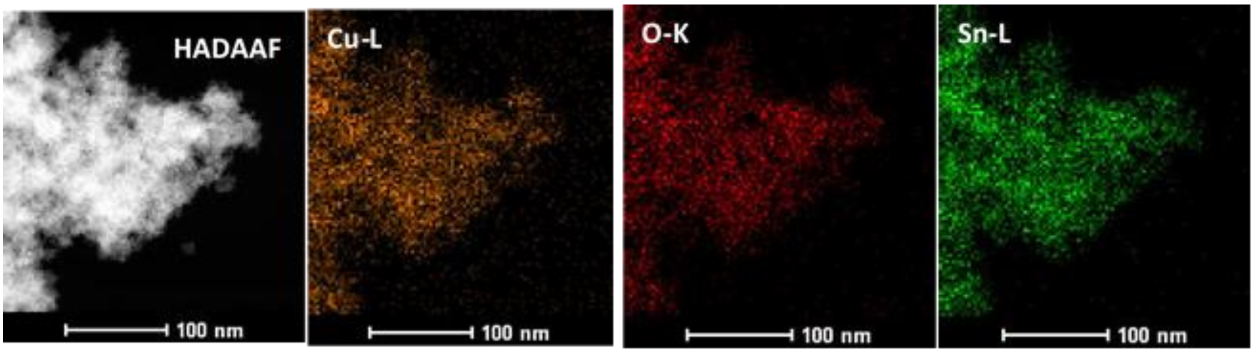

Fig. 5.4: STEM-EDS maps of CuO/SnO_2 -(1.0:1.0M).

Fig. 5.5 shows UV-vis absorption spectra of pure and the plots $(F(R)\ hv)^2$ against (hv) for SnO_2, CuO, SnO_2/CuO-(1.0:1.0M), SnO_2/CuO-(1.0:0.5M), SnO_2/CuO-(0.5:1.0M). The measurements were taken from 800 to 300 nm. The energy band gap were extracted by Kubelka-Munk equation (KM) were absorption $(F(R)\ hv)^2$ equal to zero, using dash line as indicated in the fig. 5.5 (f), the band gap energy were found to be 3.26eV for SnO_2, which is close to the reported band gap [5.11], 1.58eV for CuO, which is near the reported band gap of 1.4 eV [10], 2.97eV SnO_2/CuO-(1.0:1.0M), 3.30eV for SnO_2/CuO-(1.0:0.5M) and 2.32eV for SnO_2/CuO-(0.5:1.0M) respectively. The band gap energy increases due to the reduction of the crystal size.

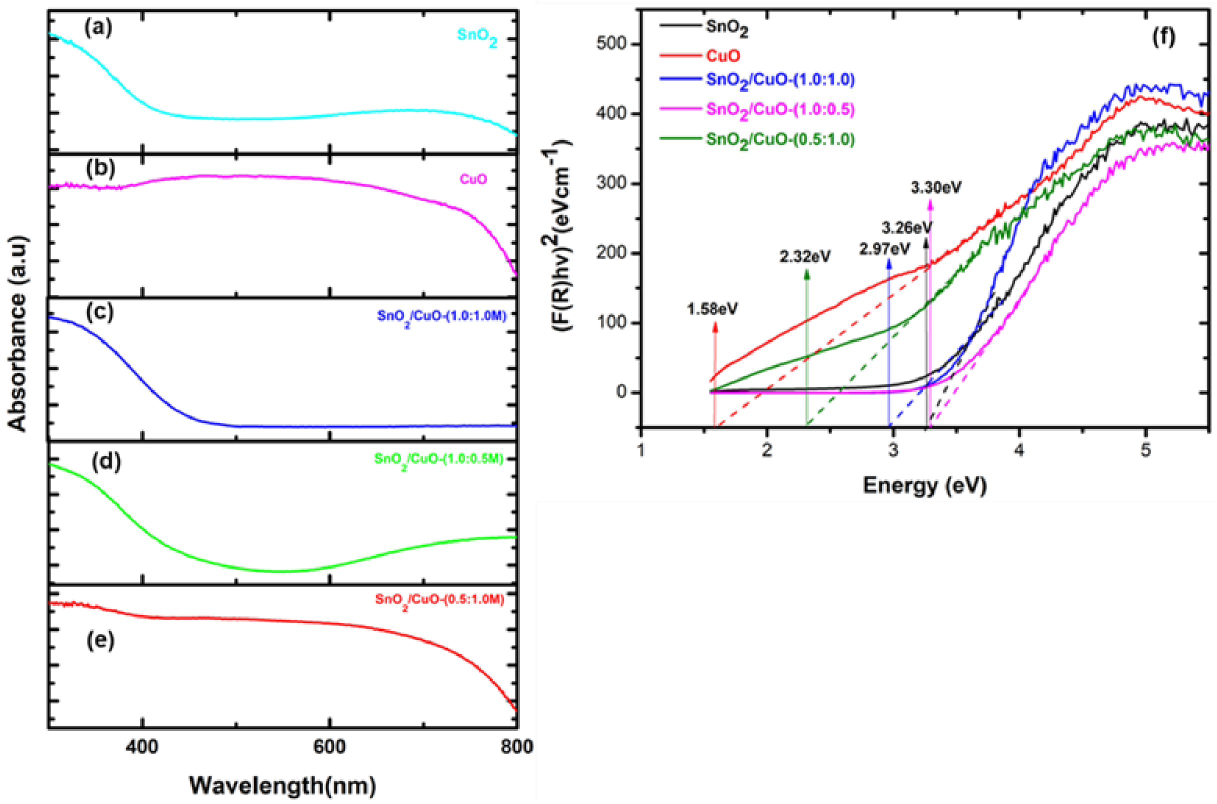

Fig. 5.5: UV-vis absorption spectra of pure (a) SnO_2, (b) CuO, (c) SnO_2/CuO-1.0:1.0 M,(d) SnO_2/CuO-1.0:0.5 M and (e) SnO_2/CuO-0.5:1.0 M. (f) The Kubelka-Munk (K-M) plots $(F(R)\ hv)^2$ against (hv) for pure SnO_2 and CuO, and their heterostructure with different molar concentration ratio.

Fig. 5.6 (a) presents the resistance-time plots for SnO_2/CuO-(1.0:1.0 M), SnO_2/CuO-(1.0:0.5 M SnO_2/CuO-(0.5:1.0 M) heterostructures tested toward NO_2 at room temperature and 100 °C. The change in electrical signals is observed when the sensors are exposed to NO_2 gas at that operating temperature. The sudden increase is resistances of the sensors is observed when exposed to oxidising gas of NO_2, this shows that the composites exhibit n-type conductivity behaviours. The sensors exhibited the response when the gas was injected in the test chamber and recovered incompletely when the gas was flushed out with air, which may be due to the NO_2 gas remained in the test chamber. The different molar concentrations have effect on the sensing behaviour of the nanocomposites. This indicates that the sensors could only respond at room temperature, which is considered as an optimal temperature.

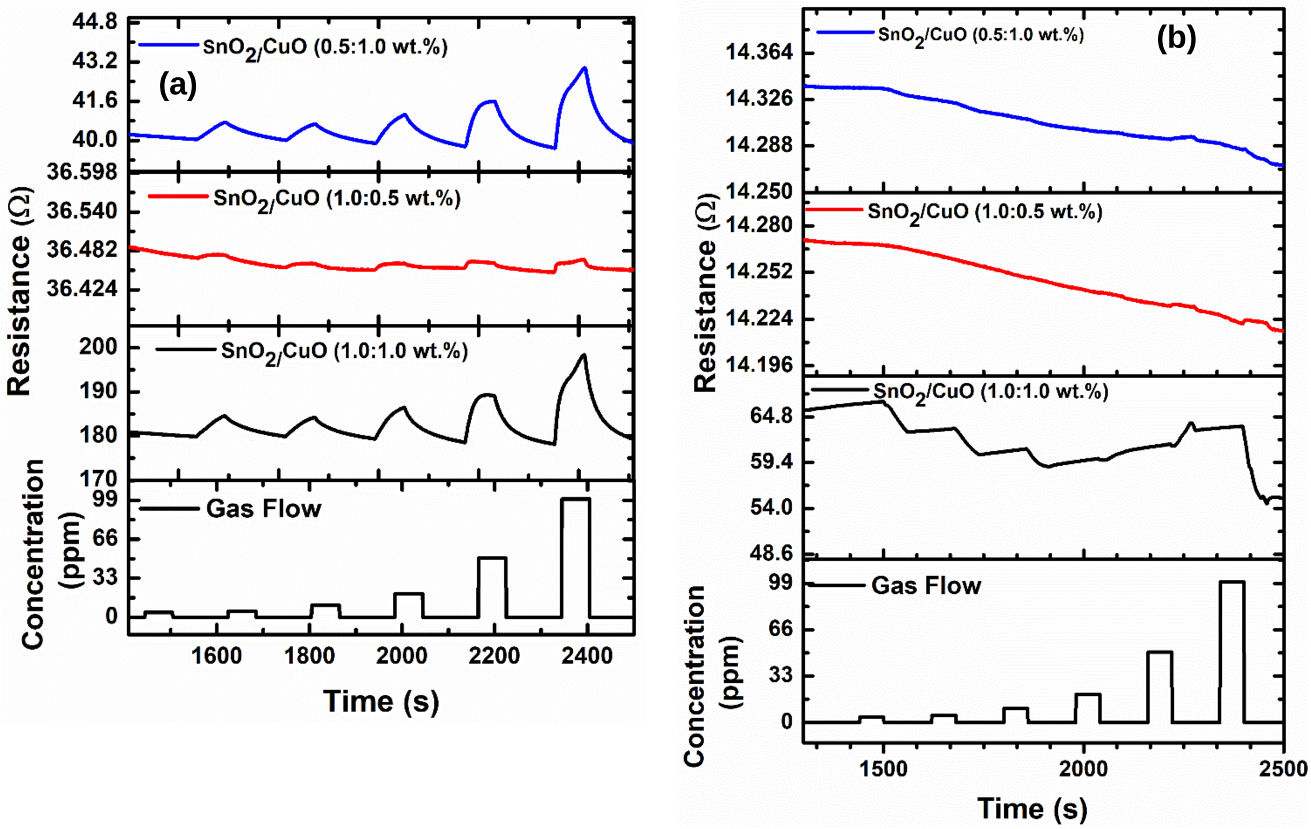

Fig. 5.6: The plots of (a) Resistance against time, and (b) Response against concentration for SnO_2/CuO-(1.0:1.0 M) and SnO_2/CuO-(0.5:1.0 M) at 25 °C, for NO_2 gas.

Fig. 5.7(a) shows the response of the sensors when exposed to different NO_2 concentrations at room temperature. At 10 ppm, the SnO_2/CuO-(1.0:1.0 M) and SnO_2/CuO-(0.5:1.0 M) had a response of 1.05 and 1.04, respectively. While higher concentration (100 ppm), the SnO_2/CuO-(1.0:1.0 M), disclosed the highest response of 1.13. The higher response could be justified by smaller nanoparticles observed from the SEM analyses, leading to reduced crystallite sizes.

Fig. 5.7(b) shows the radar selectivity plot of various sensors towards different gases. The SnO_2/CuO-(1.0:1.0 M) shows better selectivity, followed by SnO_2/CuO-(0.5:1.0 M)-based sensor towards NO_2 gas in comparison to other gases. This shows that the sensors could some-how be useful for detection of NO_2.

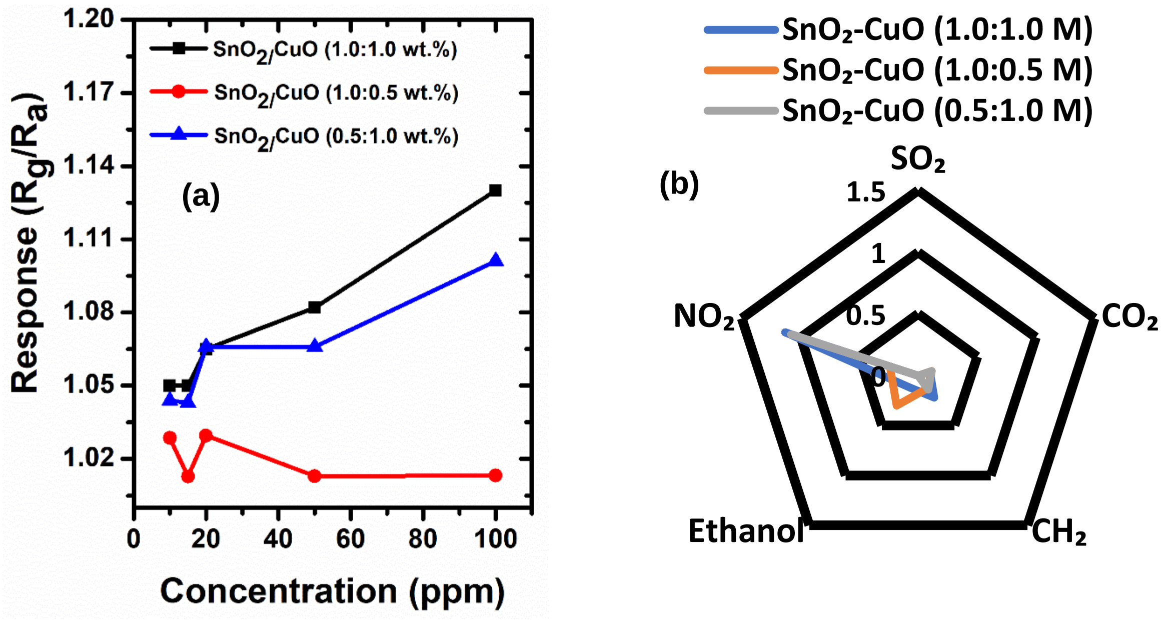

Fig. 5.7: Response versus NO_2 concentration, and (b) radar selectivity plot.

Table 5.2 shows the comparison behavior of the various sensors from the literature with the current work. Compared to sensors prepared in refs. [5.14] and [5.15], our sensor shows better response/recovery times. Moreover, with respect to ref. [5.15], our sensor further shows improved response. Though we should point out that further improvement in synthesis approach is required, by either doping with noble metals to improve the sensitivity of our sensors. Such work will be considered in the future.

Table 5.2: Summary of the NO_2 gas sensing performances of different gas sensor materials.

Materials	Technique	NO_2 (ppm)	Temperature (°C)	Response	T_{res}/T_{rec} (s)	Refs
SnO_2/CuO-(1.0:1.0 M)	Hydrothermal	10	25	1.13	50/77	**This work**
CuO	Hydrothermal	5	25	1221.3	6.8/55.1	[5.12]
CuO	Hydrothermal	40	75	39.0	-/-	[5.13]
SnO_2	Hydrothermal	10	25	94	10/413	[5.14]
V_2O_5	Sputter deposition	100	150	32.5%	102.29 /778.23	[5.15]
rGO-Co_3O_4	Hydrothermal	60	25	80	120/…	[5.16]

References

5.1. E.M. Pate. Practical Considerations in the Implementation of Emissions Reduction Solutions at Eskom's Coal Fired Power Plan. 2012. 11-20.

5.2. R. Gorham. Air Pollution from Ground Transportation.2002. 2-4.

5.3. C.H. Drake. Understanding the low temperature electrical properties of nanocrystalline SnO2 for gas sensor applications. 2003. 2-4.

5.4. D.J. Jarvis, G. Adamkiewicz, M.-E. Heroux, Regula Rapp, and Frank J. Kelly. WHO Guidelines for Indoor Air Quality: Selected Pollutants. Nitrogen oxide. 2010.

5.5. B. Ostro. Outdoor pollution.2004. 1.

5.6. Adverse Health Effects of Elevated Nitrogen Dioxide (NO2) Levels in Homes – Case study. www.E-Inst.com.

5.7. Ananya Dey. Semiconductor metal oxide gas sensors. Materials Science & Engineering B. (2018). 229. p206–217.

5.8. Sanjit Manohar Majhi. Ali Mirzaei. Hyoun Woo Kim. Sang Sub Kim. Tae Whan Kim. Recent advances in energy-saving chemiresistive gas sensors: A review. Nano Energy. (2021). 79. p1-25.

5.9. R Jayaseelan. M Gopalakrishnan. Synthesis and Characterization of Virgin and Ag doped CuO: SnO_2 Mixed Composites. DJ Journal of Engineering Chemistry and Fuel. (2017). 2(1). p 10-20.

5.10. R.N. Mariammal. K. Ramachandran. B. Renganathan. D. Sastikumar. On the enhancement of ethanol sensing by CuO modified SnO_2 nanoparticles using fiber-optic sensor. Sensors and Actuators B. (2012). 169. p199– 207.

5.11. Kyaw Kyaw. Hnin Yu Khaing. Fabrication and Structural Properties of CuO Doped SnO_2 Nanostructured Thin Films. University of Mandalay. Research Journal. (2020). 11. p169-177.

5.12. Haineng Bai. Hui Guo. Jin Wang. Yan Dong. Bin Liu. Zili Xie. Fuqiang Guo. Dunjun Chen. Rong Zhang. Youdou Zheng. A room-temperature NO2 gas sensor based on CuO nanoflakes modified with rGO nanosheets. Sensors and Actuators: B. Chemical. (2021). 337. p1-13.

5.13. Dina N. Oosthuizen. David E. Motaung. Hendrik C. Swart. Temperature-dependent NO2 gas sensing study of hydrothermally prepared CuO nanoplatelets. 17th International Meeting on Chemical Sensors. (2018). P897-898. DOI 10.5162/IMCS2018/P2NG.28.

5.14. Ji Li. Ming Yang.Xiaoli Cheng. Xianfa Zhang. Chuanyu Guo.Yingming Xu.Shan Gao.Zoltán. Major.Hui Zhao. Lihua Huo. Fast detection of NO_2 by porous SnO_2 nanotoast sensor at low temperature. Journal of Hazardous Materials. (2021). 419. p1-10.

5.15. Vijendra Singh Bhati. D Sheela. Basanta Roul. Ramesh Raliya. Pratim Biswas. Manish Kumar. M S Roy. K K Nanda. S B Krupanidhi. Mahesh Kumar. NO_2 gas sensing performance enhancement based on reduced graphene oxide decorated V_2O_5 thin films. Nanotechnology. (2019). 30. p1-12.

5.16. Chen N. Li X. Wang X. Yu J. Wang J. Tang Z. Akbar S. Enhanced room temperature sensing of Co3O4-intercalated reduced graphene oxide based gas sensors. Sens. Actuators B Chem. (2013). 188. p902–908.

CHAPTER 6.

SUMMARY

Various SnO_2 and V_2O_5 nanostructures were efficiently synthesized using a hydrothermal method in different base solutions. Surface analyses illustrated that the SnO_2-NaOH possessed hollowspheres like structures with a chirped/etched surface, while the SnO_2-NH_4OH and SnO_2-Urea showed nanoflakes and hierarchical spheres with smooth edges, respectively. The V_2O_5-NaOH showed nanorod like structures, which are attached to one another, while the V_2O_5-Urea displayed hexagonally shaped thick rods like structures. XRD analyses displayed that both the SnO_2 and V_2O_5 were highly crystalline and the SnO_2 followed the following behaviour in terms of crystallinity: SnO_2-NH_4OH>SnO_2-Urea>SnO_2-NaOH. The nanostructures were further analysed using In-situ EPR and in-situ PL studies. Both the in-situ PL and EPR showed that the SnO_2-NaOH contained a higher number of V_O. Sensing performances of the designed gas sensors were evaluated toward CO in the presence of other interference gases, H_2S, CH_4, NO_2 and VOCs, such as methanol and ethanol. The SnO_2-NaOH based sensor demonstrated improved response and selectivity towards CO gas at 75 °C from the tested six sensors. Additionally, the SnO_2-NaOH based sensor illustrated the lowest theoretical detection limit of 70 ppb. These findings point out that the SnO_2-NaOH based sensor is a favourable, reliable, and economical solution for detection of CO gas for the air quality monitoring at ppb-level. This versatile tunability on SnO_2 hollowspheres derived from the use of NaOH base introduced a new avenue for fabricating distinct and tailored sensors for detection of CO at a low operating temperature. Thus, the future work will focus on improving the stability, while maintaining the sensitivity.

Moreover, with respect to low temperature detection of NO_2, the SnO_2/CuO-(1.0:1.0 M), SnO_2/CuO-(0.5:1.0 M) and SnO_2/CuO-(1.0:0.5 M) heterostructures-based sensors were fabricated. Various instrumentations validated the formation of heterostructures. Among the tested sensors, the SnO_2/CuO-(1.0:1.0 M)-based sensor demonstrated higher response towards NO_2, in the presence of other four gases at room temperature. At higher temperature of 100 °C, the sensors showed poor response, justifying that their optimal temperature is 25 °C. These findings point out that these sensors could be considered as low-power consumption sensors for detection of NO_2.

Future Work:

- Focuses on further improving the approach of synthesis method.
- Investigate the long-term stability in dry air and in the presence of relative humidity (i.e., 0-60 %)
- Improve the sensitivity by introducing noble metals (i.e., Au, Pt, Ag) on the surface of SnO_2/CuO.
- Investigate the effect of bias voltage on the sensing performance.
- Investigate the low concentration of NO_2 (<5 ppm).
- Attempt to fabricate self-powered sensors for the purpose of low-power consumption.

APPENDIX A

Low Temperature Tunability on CO Selectivity, Low Detection Limit Based on SnO_2-Hollowspheres Induced by Various Bases

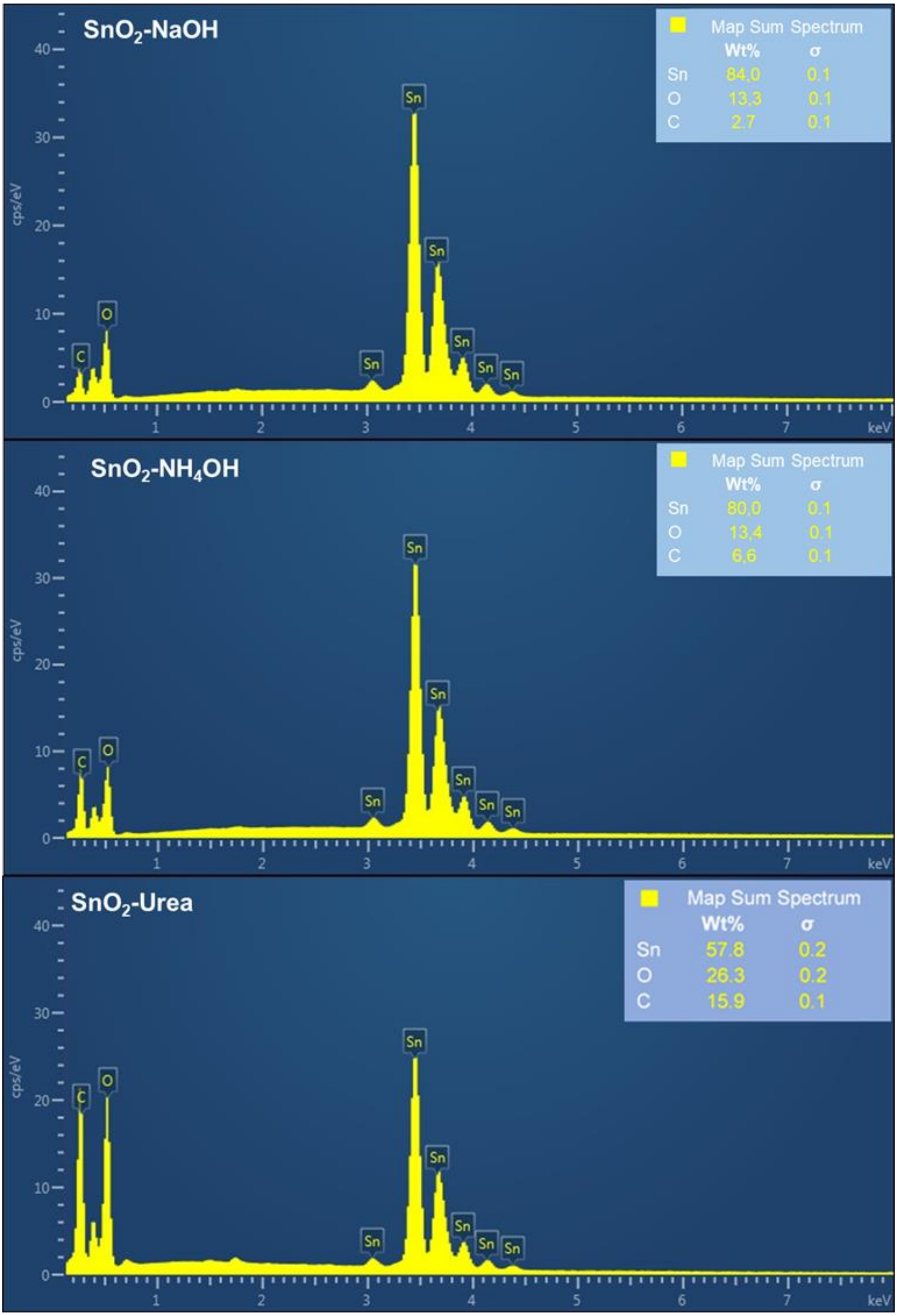

SnO$_2$-NaOH

Map Sum Spectrum	Wt%	σ
Sn	84,0	0.1
O	13,3	0.1
C	2.7	0.1

SnO$_2$-NH$_4$OH

Map Sum Spectrum	Wt%	σ
Sn	80,0	0.1
O	13,4	0.1
C	6,6	0.1

SnO$_2$-Urea

Map Sum Spectrum	Wt%	σ
Sn	57.8	0.2
O	26.3	0.2
C	15.9	0.1

Fig. A1: EDS spectra of SnO$_2$-NaOH, SnO$_2$-NH$_4$OH and SnO$_2$-Urea

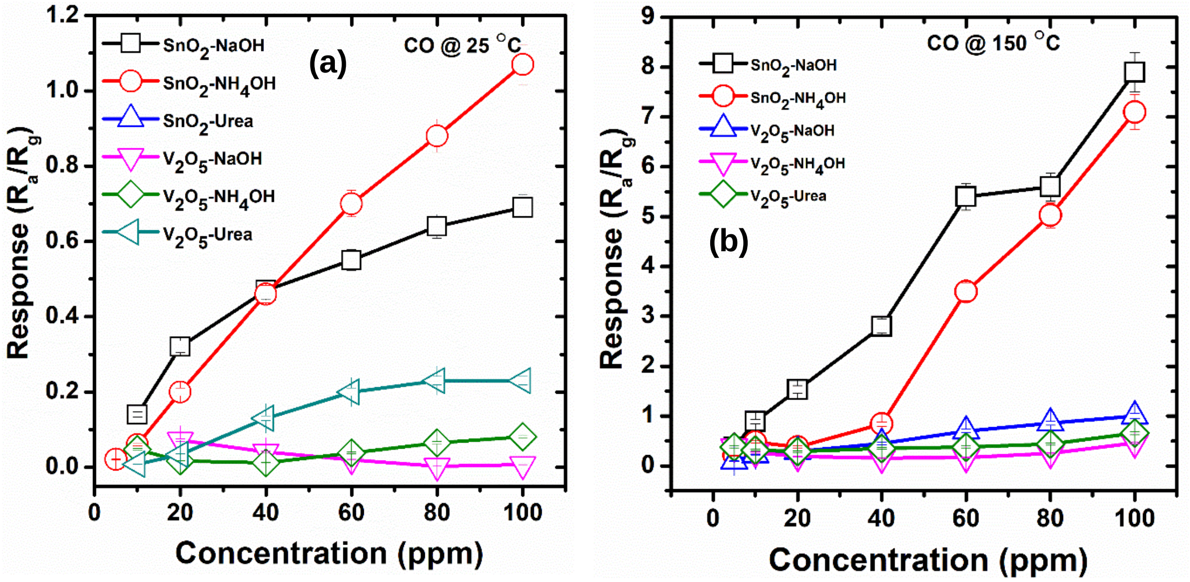

Fig. A2: Response versus CO concentration at (a) 25 and (b) 150 °C.

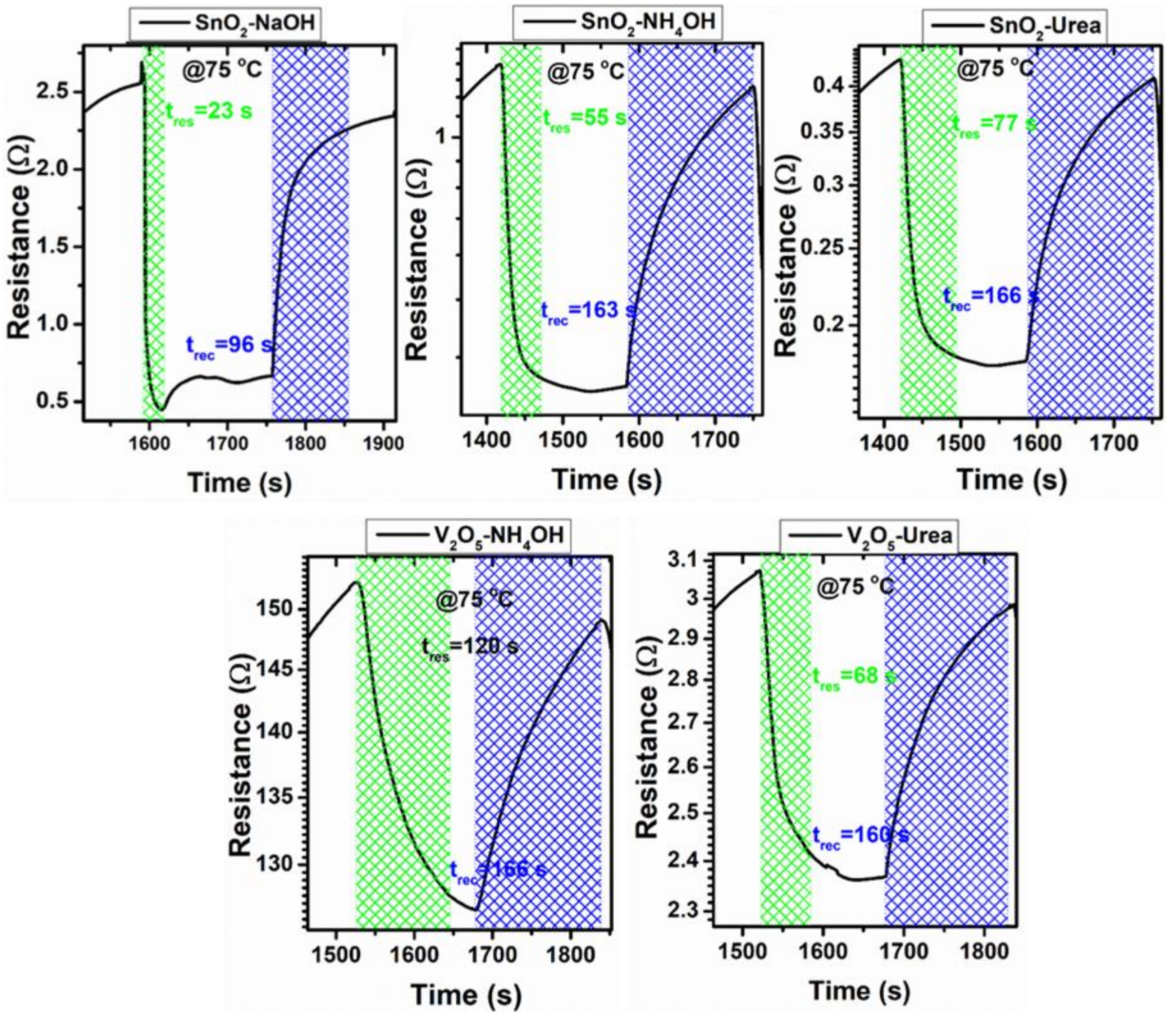

Fig. A3: Response and recovery times of various nanostructures towards CO at 75 °C.

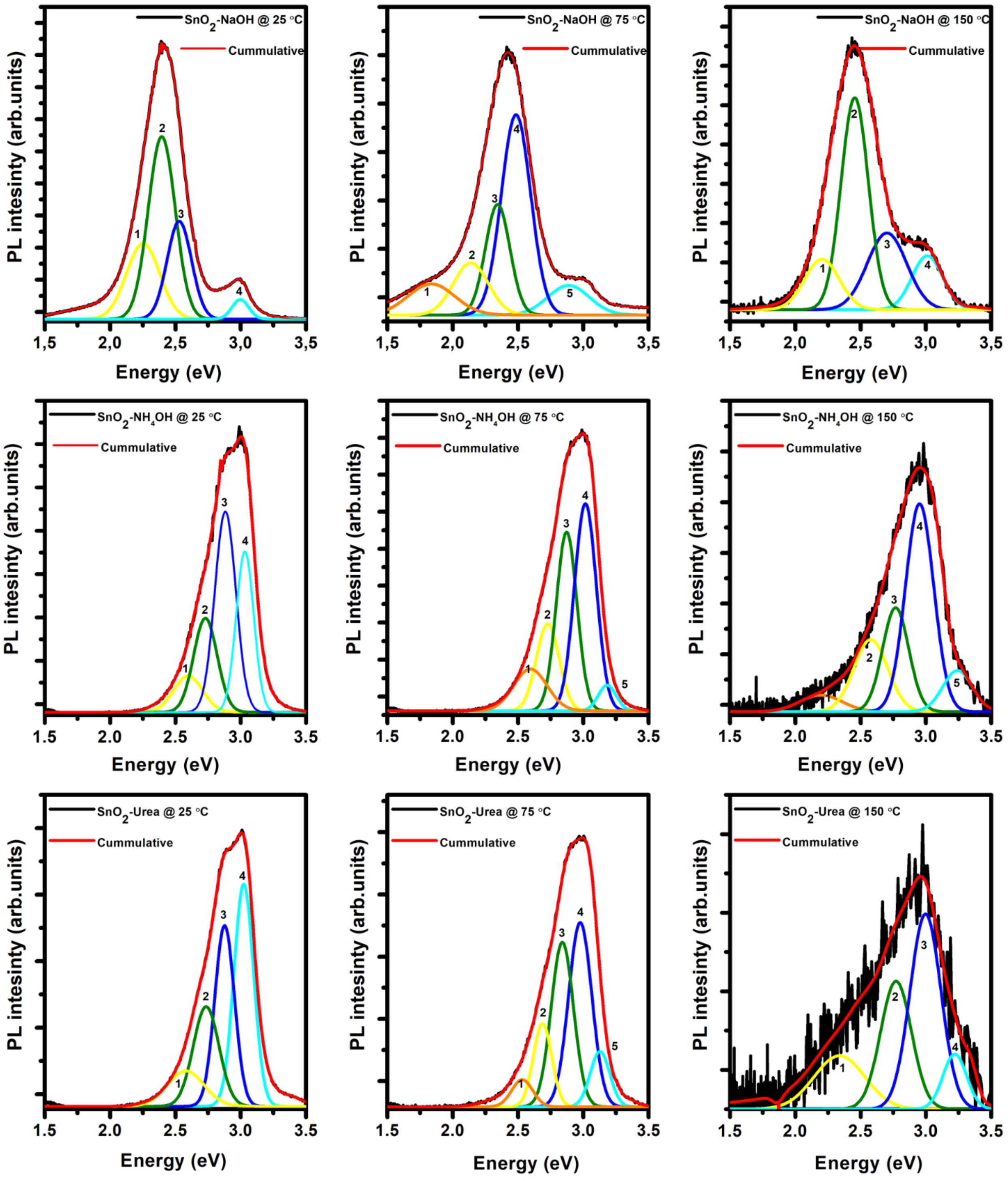

Fig. A4: PL fitted plots of SnO$_2$-NaOH, SnO$_2$ and SnO$_2$-Urea measured at different Temperatures.